

MARKUS NEUSCHITZER, BSc

Grazing incidence in-plane X-ray diffraction on ultra-thin organic films using standard laboratory equipment

MASTER THESIS

For obtaining the academic degree
Diplom-Ingenieur

Master Programme of
Technical Physics



Graz University of Technology

Supervisor:

Ao.Univ.-Prof. Dipl.-Ing. Dr.techn. Roland Resel
Institut of Solid State Physics
Graz University of Technologies

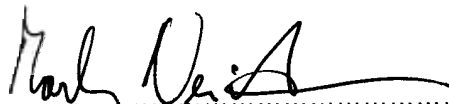
Graz, March, 2012

Deutsche Fassung:
Beschluss der Curricula-Kommission für Bachelor-, Master- und Diplomstudien vom 10. .2008
Genehmigung des Senates am 1.12.2008

EIDESSTATTLICHE ERKLÄRUNG

Ich erkläre an Eides statt, dass ich die vorliegende Arbeit selbstständig verfasst, andere als die angegebenen Quellen/Hilfsmittel nicht benutzt, und die den benutzten Quellen wörtlich und inhaltlich entnommene Stellen als solche kenntlich gemacht habe.

Graz, am 27.03.2012


(Unterschrift)

Englische Fassung:

STATUTORY DECLARATION

I declare that I have authored this thesis independently, that I have not used other than the declared sources / resources, and that I have explicitly marked all material which has been quoted either literally or by content from the used sources.

27.03.2012
date


(signature)

Acknowledgment

First of all I would like to thank my supervisor Roland Resel for the possibility to work on this interesting project and for making it possible to spend a beamtime at the HASYLAB DORIS W1 beamline and to participate at the 2011 European Materials Research Society Spring Meeting in Nice, France, which both were great experiences. He always gave me encouragement and the right direction to this work and he also gave me the time needed to find and try my own approaches.

Furthermore, I would like to thank Jiri Novak who started the whole project during his postdoc stay at our institute. He gave me a great introduction into the field of grazing incidence X-ray diffraction and X-ray reflectivity and always took his time to discuss theoretical and experimental issues in detail.

Another big thank you goes to Alfred Neuhold who took me to the HASYLAB beamtime and introduced me into the art of X-ray reflectivity fitting. Further, many thanks to Armin Moser who was always there to solve my python code errors and for all the fruitful discussions about X-ray diffraction. I would like to thank Ingo Salzmann for his support at HASYLAB, for further synchrotron measurements he did for me and for his comments on the results.

I would like to thank Johanna Kraxner and Barbara Stadlober from the Joanneum Research Forschungsgesellschaft mbH, Institute of Surface Technologies and Photonics for preparing pentacene samples and AFM measurements. Thanks to Birgit Kunert and Harald Kerschbaumer for all the technical support. A big thanks to Ulrich Kaltenbrunner for drawing these fancy CAD schematics for me.

Of course, I would like to thank all the people of my office the 'k-Raum' Tatjana Djuric, Alfred Neuhold, Armin Moser, Michael Dohr, and Reinhold Hetzel for the great time there. It was always a great atmosphere and I had many inspiring conversations.

Last but not least I would like to thank my mum and dad for all their support in every moment of my life and of course my brother Andreas with whom I spend lots of great time together in the mountains or at the sea to gain new energies for my work at the university.

Abstract

Grazing incidence in-plane X-ray diffraction (GIXD) is a powerful technique to solve problems in material science. First established by Marra et al. (1979) to study crystal surfaces and interfaces, it is now widely used to determine in-plane order and crystal-line properties of thin films. In GIXD X-rays impinge on the sample surface under a grazing angle below the angle of total external reflection, resulting in an evanescent wave propagating parallel to the surface. Perpendicular to the surface, its amplitude is exponentially damped, i.e. its penetration depth is limited to several nanometers depending on the incidence angle, the used wavelength of the radiation, as well as the electron density of the material. Therefore, in a GIXD experiment the evanescent wave is scattered only by the first few surface layers resulting in an exceedingly increased surface sensitivity. Moreover, the wave field amplitude of the evanescent wave is enhanced up to a factor of two because incident, reflected, and transmitted wave fields couple coherently at the surface. As a result, GIXD allows performing scattering experiments on thin films of very low scattering volume. Because of its scattering geometry GIXD probes lattice planes that are almost perpendicular to the surface. Thus, the in-plane structure of the sample can be determined and GIXD allowed for the first time even to characterize the structure of ordered organic monolayers.

Nowadays, GIXD measurements are mostly performed using synchrotron radiation sources of high brilliance. However, an increasing interest to GIXD setups in laboratories arose with the emergence of more sophisticated X-ray optics. This work shows in detail the realization of a novel grazing incidence in-plane X-ray diffraction (GIXD) setup in the laboratory. The setup is based on a commercial 4-circle diffractometer with a sealed-ceramic copper X-ray tube, upgraded with parabolic graded multilayer X-ray optics and a one-dimensional position sensitive detector. The high potential of this setup is demonstrated by a phase analysis study of pentacene thin-films and the determination of in-plane lattice constants of pentacene mono- and multilayers. There, a detailed comparison between GIXD laboratory results and synchrotron measurements is given. Furthermore, the in-plane crystal structure of self-assembled monolayers based on functionalized quinquethiophene molecules is investigated. In addition to GIXD, X-ray reflectivity measurements are employed to probe the out-of-plane order of these ultra-thin organic films.

The introduced GIXD setup is also applicable on inorganic thin-film characterization. A qualitative phase analysis of inorganic oxide solar cell multilayer stacks is presented as a combination of normal specular X-ray diffraction and GIXD. Depending on the layer growth conditions different copper oxide phases could be determined in the multilayer by GIXD measurements. Due the fact that only the cupric oxide phase (CuO) is favorable for an efficient device performance this phase analysis was from high importance to optimize the growth process of the copper oxide layers.

Kurzfassung

Um Fragestellungen der Materialwissenschaften zu lösen ist Röntgenbeugung bei streifendem Einfall (grazing incidence in-plane X-ray diffraction - GIXD) eine herausragende experimentelle Technik. Erstmals experimentierte Marra et al. (1979) damit um kristalline Oberflächen und Grenzschichten zu untersuchen. Heute wird diese Technik vor allem zur Bestimmung der kristallinen Eigenschaften und „in-plane“ Ordnung dünner Filme verwendet.

Bei GIXD treffen Röntgenstrahlen mit einem Einfallswinkel unterhalb des Winkels der Totalreflektion auf der Probenoberfläche auf. Dadurch bildet sich eine evaneszente Welle aus, die sich parallel zur Oberfläche fortbewegt. Normal zur Oberfläche ist die Amplitude dieser Welle exponentiell gedämpft, d.h. ihre Eindringtiefe beschränkt sich auf einige Nanometer abhängig vom Einfallswinkel, der verwendeten Wellenlänge und der Elektronendichte des zu untersuchenden Materials. Auf Grund der geringen Eindringtiefe wird die evaneszente Welle nur von den ersten oberflächennahen Schichten gestreut und GIXD Experimente sind daher besonders oberflächensensitiv. Weiters wird die Amplitude der evaneszenten Welle bis zu einem Faktor zwei verstärkt, da sich die einfallenden, reflektierten und transmittierten Wellen kohärent verstärken. Somit sind auch Beugungsexperimente an sehr dünnen Schichten möglich, die nur ein sehr geringes Streuvolumen aufweisen. Zusätzlich werden durch die in GIXD verwendete Streugeometrie Netzebenen, die nahezu normal zur Oberfläche stehen, untersucht. Es wird daher nur die kristalline Ordnung parallel zur Oberfläche („in-plane“) analysiert. So war es mit Hilfe von GIXD zum ersten Mal möglich die Kristallstruktur von geordneten Monolagen zu bestimmen. Heutzutage werden GIXD Experimente hauptsächlich an Synchrotron-Strahlungsquellen durchgeführt. Mit dem Aufkommen von besseren Röntgenoptiken stieg jedoch das Interesse an GIXD Aufbauten in Laboratorien.

Diese Arbeit zeigt detailliert die Realisierung eines neuartigen GIXD-Setups im Labor. Das Setup basiert auf einem kommerziellen 4-Kreis Diffraktometer mit Kupfer-Röntgenröhre, das mit einem parabolischen Multilagen-Röntgenspiegel und einem ein-dimensionalen Detektor aufgerüstet wurde. Das hohe Potential dieses Setups wird anhand einer Phasenanalyse von Pentacen-Dünnschichten und der Bestimmung der „in-plane“ Gitterkonstanten von Pentacen-Monolagen aufgezeigt. Dabei werden die Ergebnisse detailliert mit Synchrotron Messungen verglichen. Desweiteren werden Untersuchungen der „in-plane“ Struktur von selbstassemblierten Monolagen aus funktionalen Quinquethiophenen präsentiert. Zusätzlich zu den GIXD Experimenten wurden auch Röntgenreflektometriemessungen durchgeführt um die „out-of-plane“ Struktur dieser dünnen Filme zu untersuchen.

Das vorgestellte Setup eignet sich auch hervorragend um anorganische Dünnschichten zu charakterisieren. Es wird eine qualitative Phasenanalyse einer anorganischen Multilagen-Oxid-Solarzelle anhand von konventionellen spekularen Röntgenbeugungsexperimenten und GIXD Messungen präsentiert. Abhängig von den Wachstumsparametern konnten unterschiedliche Kupferoxidphasen mittels GIXD bestimmt werden. Auf Grund der Tatsache, dass nur Kupfermonoxid (CuO) zu einer zufriedenstellenden Effizienz

der Solarzelle führt, war diese Phasenanalyse von hoher Wichtigkeit um den Wachstumsprozess der Kupferoxid Schichten optimieren zu können.

Contents

1. X-ray interaction with matter	13
1.1. Basic principles	13
1.2. Snell's law in the X-ray region	15
1.3. Fresnel equations in the X-ray region	17
1.4. Evanescent wave	18
1.5. Reflectance and Transmittance	20
1.6. X-ray reflectivity from surfaces	22
1.6.1. X-ray reflectivity of a homogeneous slab	22
1.6.2. X-ray reflectivity from multilayers - Parratt's recursive formalism	24
1.6.3. The influence of roughness on the reflectivity	25
1.7. X-Ray diffraction	27
1.7.1. Kinematical X-Ray diffraction	27
1.7.2. Evanescent X-ray scattering	32
2. Experimental setups	37
2.1. Bruker Grazing incidence in-plane X-ray diffraction setup	37
2.1.1. Experimental data processing	39
2.1.2. Flat field correction for 1d data of Vantec-1 detector	40
2.2. HASYLAB beamline W1	43
2.3. Panalytical Empyrean X-ray reflectivity setup	44
3. Experimental setup performance - results and details	47
3.1. Pentacene	47
3.1.1. Pentacene polymorphs	48
3.1.2. Pentacene 50 nm thin-films	50
3.1.3. Pentacene mono- and multilayers	56
3.1.4. Bragg rod analysis	65
3.1.5. Degradation under the X-ray beam	65
3.2. Microstructure characterization of a quinquethiophene based self-assembled monolayer	69
3.2.1. Fabrication and layer formation	69
3.2.2. XRR investigations	71
3.2.3. GIXD investigations	73
3.2.4. Degradation under the X-ray beam	77
3.3. Qualitative phase analysis of inorganic oxide solar cell multilayer stack	79
3.3.1. Specular XRD and GIXD investigations	79

CONTENTS

4. Conclusion	85
A. GIXD setup: how to align and measure	89
A.1. Alignment of the GIXD setup	89
A.2. GIXD Measurements	90
B. Coplanar diffraction configuration	97
B.1. Alignment of coplanar configuration	97
C. Paper published at the Journal of Applied Crystallography, Volume 45, Part 2, pages 367-370	101

1. X-ray interaction with matter

1.1. Basic principles

From an electrodynamic viewpoint one describes electromagnetic waves inside a medium using the Maxwell's equations (Born & Wolf, 1998)

$$\nabla \cdot \mathbf{B} = 0 \quad (1.1)$$

$$\nabla \times \mathbf{E} + \frac{\partial \mathbf{B}}{\partial t} = 0 \quad (1.2)$$

$$\nabla \cdot \mathbf{D} = \rho_f \quad (1.3)$$

$$\nabla \times \mathbf{H} - \frac{\partial \mathbf{D}}{\partial t} = \mathbf{j}_f \quad (1.4)$$

with \mathbf{E} the electric field vector, \mathbf{B} the magnetic induction field vector, \mathbf{D} the electric displacement field vector, \mathbf{H} the magnetic field vector, ρ_f the charge density the free electrons, and \mathbf{j}_f the current density of the free electrons. For isotropic materials the fields are related with simple equations

$$\mathbf{D} = \epsilon \mathbf{E} \quad (1.5)$$

$$\mathbf{B} = \mu \mathbf{H} \quad (1.6)$$

where ϵ is known as dielectric constant (or permittivity) and μ as magnetic permeability. Further, for the case of dielectrics (i.e., $\rho_f = 0$ and $\mathbf{j}_f = 0$) one can decouple Maxwell's equations

$$\nabla^2 \mathbf{E} - \epsilon \mu \frac{\partial^2 \mathbf{E}}{\partial t^2} = 0 \quad (1.7)$$

$$\nabla^2 \mathbf{H} - \epsilon \mu \frac{\partial^2 \mathbf{H}}{\partial t^2} = 0 \quad (1.8)$$

and for the case of plane waves $\mathbf{E} = \mathbf{E}_0 \exp(i(\mathbf{k} \cdot \mathbf{r} - \omega t))$ one gets out of Eq. (1.7) the Helmholtz equation

$$\nabla^2 \mathbf{E}(\mathbf{r}) + k_0^2 n^2(\mathbf{r}) \mathbf{E}(\mathbf{r}) = 0 \quad (1.9)$$

where $k_0 = \omega/c_0$ is the modulus of the wavevector in vacuum and $n(\mathbf{r}) = c_0/c_m$ is the index of refraction. The Helmholtz equation is perfectly suited to describe the propagation of electromagnetic plane waves in a transparent medium described by a index of refraction $n(\mathbf{r})$. The index of refraction is defined as the ratio of the speed of light in vacuum (c_0) to the phase speed of light in the medium ($c_m = 1/\sqrt{\epsilon\mu}$). Assuming a harmonic oscillator of N atoms per unit volume with resonance frequencies ω_j the index of refraction can be expressed as (Hecht, 2002)

$$n^2(\mathbf{r}) = 1 + N \frac{e^2}{\epsilon_0 m} \sum_{j=1}^N \frac{f_j}{\omega_j^2 - \omega^2 + i\gamma_j \omega} \quad (1.10)$$

where ω is the frequency of the incoming plane wave, e the charge of the electron, m the mass of the electron, γ_j the damping factors, and f_j the oscillator strengths of the electrons of each atom which is a energy dependent complex number $f_j = f_j^0 + f_j'(E) + i f_j''$. For the case of X-rays $\omega > \omega_j$ and $n(\mathbf{r})$ can be written as (Tolan, 1999)

$$n(\mathbf{r}) = 1 - \delta(\mathbf{r}) + i\beta(\mathbf{r}) \quad (1.11)$$

where $\delta(\mathbf{r})$ takes dispersion into account

$$\delta(\mathbf{r}) = \frac{\lambda^2}{2\pi} r_e \rho(\mathbf{r}) \sum_{j=1}^N \frac{f_j^0 + f_j'(E)}{Z} \quad (1.12)$$

and $\beta(\mathbf{r})$ is the absorption term

$$\beta(\mathbf{r}) = \frac{\lambda^2}{2\pi} r_e \rho(\mathbf{r}) \sum_{j=1}^N \frac{f_j''(E)}{Z} = \frac{\lambda}{4\pi} \mu(\mathbf{r}) \quad (1.13)$$

Here $r_e = e^2/(4\pi\epsilon_0 m c^2) = 2.81410^{-5} \text{\AA}$ is the classical electron radius or Thompson scattering length of the electron, $Z = \sum_{j=1}^N Z_j$ is the total number of electrons inside the material (Z_j is the number of electrons of each atom of the material), $\rho(\mathbf{r})$ is the electron density of the material, and $\mu(\mathbf{r})$ is the linear absorption coefficient. Far away from absorption edges and for a homogeneous medium $f_j^0 \approx Z_j$, thus $\delta(\mathbf{r})$ can be simplified to

$$\delta(\mathbf{r}) = \lambda^2 r_e \rho / (2\pi) \quad (1.14)$$

For X-rays δ is always a positive number and in the order of magnitude of $\sim 10^{-6}$ (Tolan, 1999), therefore the index of refraction for all materials is slightly less than unity in the X-ray regime. One might ask oneself if that means that the speed of light is higher in the material than in vacuum, however, as mentioned above $c_m = c_0/n$ is the phase velocity and not the group velocity ($d\omega/dk$) which is indeed less than c_0 (Als-Nielsen & McMorrow, 2001). Furthermore, a refraction index lower than unity leads to the phenomenon of total external reflection from a flat and sharp interface. That means that for a incidence angle lower than a certain critical angle the ray no longer penetrates the material but is totally reflected from it as we will see in the next section.

1.2. Snell's law in the X-ray region

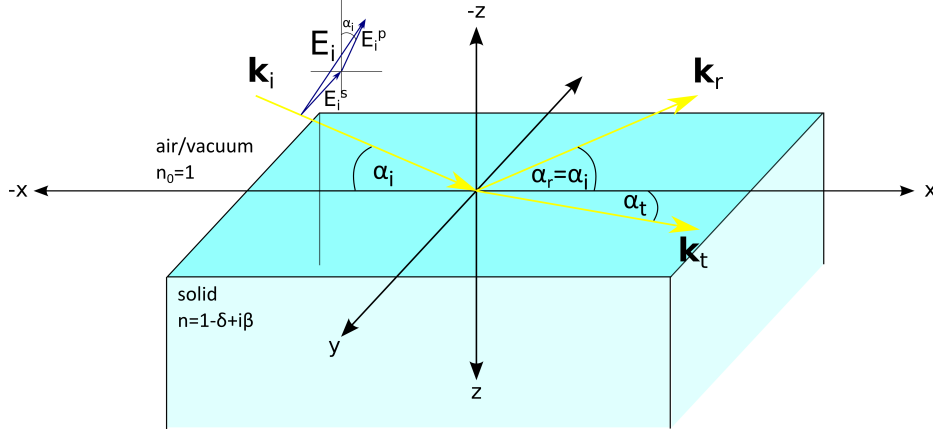


Figure 1.1.: Schematic of a plane wave \mathbf{E}_i with wavevector \mathbf{k}_i impinging on an interface ($z=0$) at an angle of incident α_i . The wave field \mathbf{E}_i is split into a part perpendicular (E_i^s) and parallel (E_i^p) to the plane of incidence (x,z -plane). Further the wavevectors of the reflected (\mathbf{k}_r) and transmitted wave (\mathbf{k}_t) are indicated.

An electromagnetic wave propagating in air (vacuum) changes directions when it enters a transparent material with a different index of refraction $n(\mathbf{r})$. This phenomena known as refraction is qualitatively described by Snell's law.

From Maxwell's equations one can derive boundary conditions for the case that the physical properties ϵ , μ , i.e., the index of refraction of a medium change abruptly across an interface. For the normal and tangential components of the fields on gets ($\hat{\mathbf{n}}$ denotes a vector normal to the interface)

$$\hat{\mathbf{n}} \times (\mathbf{H}_1 - \mathbf{H}_2) = \mathbf{i}_f \quad (1.15)$$

$$\hat{\mathbf{n}} \times (\mathbf{E}_1 - \mathbf{E}_2) = 0 \quad (1.16)$$

$$\hat{\mathbf{n}} \cdot (\mathbf{B}_1 - \mathbf{B}_2) = 0 \quad (1.17)$$

$$\hat{\mathbf{n}} \cdot (\mathbf{D}_1 - \mathbf{D}_2) = \gamma_f \quad (1.18)$$

Therefore, excluding surface currents ($\mathbf{i}_f = 0$) and surface charges ($\gamma_f = 0$) the boundary conditions at an interface are that the tangential components of the electric field vector \mathbf{E} and magnetic field vector \mathbf{H} , as well as the normal components of the electric displacement field vector \mathbf{D} and the magnetic induction field vector \mathbf{B} are continuous. To study the effects of refraction and reflection of X-rays at an interface we will use these boundary conditions.

We considering a plane X-ray wave in vacuum $\mathbf{E}_i(\mathbf{r}, t) = \mathbf{E}_i \exp(i(\mathbf{k}_i \cdot \mathbf{r} - \omega_i t))$ impinging on a flat surface of a material characterized by a refraction index n under

an incidence angle α_i as shown in Figure 1.1. This plane wave is linearly polarized with

$$\mathbf{E}_i = \begin{pmatrix} E_i^p \sin(\alpha_i) \\ E_i^s \\ -E_i^p \cos(\alpha_i) \end{pmatrix} \quad (1.19)$$

where E_i^p and E_i^s denote the components of the electric field vector parallel (the p-polarized part) and perpendicular (the s-polarized part) to the plane of incidence, respectively. One part of the impinging wave is reflected and one is transmitted at the interface. The fields of the reflected wave $\mathbf{E}_r(\mathbf{r}, t) = \mathbf{E}_r \exp(i(\mathbf{k}_r \cdot \mathbf{r} - \omega_r t))$ and the transmitted wave $\mathbf{E}_t(\mathbf{r}, t) = \mathbf{E}_t \exp(i(\mathbf{k}_t \cdot \mathbf{r} - \omega_t t))$ are split in the same way into s and p components. For the wavevectors, i.e. the directions these three distinct waves travel one gets (see Figure 1.1)

$$\mathbf{k}_i = k_i \begin{pmatrix} \cos(\alpha_i) \\ 0 \\ \sin(\alpha_i) \end{pmatrix}; \quad \mathbf{k}_r = k_r \begin{pmatrix} \cos(\alpha_r) \\ 0 \\ -\sin(\alpha_r) \end{pmatrix}; \quad \mathbf{k}_t = k_t \begin{pmatrix} \cos(\alpha_t) \\ 0 \\ \sin(\alpha_t) \end{pmatrix}; \quad (1.20)$$

Boundary condition can be applied for the three wave fields at the interface. As mentioned before (1.16) the tangential components of the electric field vector \mathbf{E} must be continuous at the interface ($z=0$) which can be expressed as

$$\hat{\mathbf{n}} \times (\mathbf{E}_i e^{i(k_i \cos(\alpha_i)x - \omega_i t)} + \mathbf{E}_r e^{i(k_r \cos(\alpha_r)x - \omega_r t)} - \mathbf{E}_t e^{i(k_t \cos(\alpha_t)x - \omega_t t)}) = 0 \quad (1.21)$$

This equation must hold for all possible values of t and x and therefore first we have to set all exponential factors equal to each other. For $x = 0$ follows

$$\omega_i = \omega_r = \omega_t \equiv \omega \quad (1.22)$$

and for $t = 0$ the equation requires

$$k_i \cos(\alpha_i) = k_r \cos(\alpha_r) = k_t \cos(\alpha_t) \quad (1.23)$$

Using $k_i = k_r = k = \omega/c_0$ and $k_t = \omega/c_m = n\omega/c_0 = nk$ one gets the law of reflection

$$\alpha_i = \alpha_r \quad (1.24)$$

and finally **Snell's law**

$$\cos(\alpha_i) = n \cos(\alpha_t) \quad (1.25)$$

Because of the fact that the index of refraction n in the X-ray region is always smaller than unity, there exists a **critical angle of total external reflection** α_c . Setting $\alpha_t = 0$ it follows from Snell's law that

$$\cos(\alpha_c) = n \quad (1.26)$$

or with $\cos^2(\alpha) = 1 - \sin^2(\alpha)$

$$\sin^2(\alpha_c) = 1 - n^2 \quad (1.27)$$

and with the real part of Eq.(1.11) $n^2 = 1 - 2\delta + \delta^2$ (neglecting δ^2 because its very small), Eq.(1.14), and for the case of small angles ($\sin(\alpha) \approx \alpha$) one gets

$$\alpha_c = \sqrt{2\delta} = \lambda \sqrt{\frac{r_e \rho}{\pi}} \quad (1.28)$$

Since δ is very small the critical angle is also very small, e.g. $\alpha_c = 0.223^\circ$ for Silicon ($\lambda = 1.54\text{\AA}$; CuK_α radiation) or even smaller for organic materials with lower electron densities (Tolan, 1999).

1.3. Fresnel equations in the X-ray region

In this section relations between the incidence, the reflected, and the transmitted wave fields are derived to investigate how the reflected and transmitted wave fields behave in dependence of the incidence angle. This relations are known as Fresnel equations or coefficients (Peatross & Ware, 2011).

Since we know from the last section that in equation (1.21) all exponents are identical it reduces to

$$\hat{\mathbf{n}} \times (\mathbf{E}_i + \mathbf{E}_r - \mathbf{E}_t) = 0 \quad (1.29)$$

\mathbf{E}_i and \mathbf{E}_r can be written as \mathbf{E}_i (1.19) split into s-polarized and p-polarized parts

$$\mathbf{E}_r = \begin{pmatrix} -E_r^p \sin(\alpha_i) \\ E_r^s \\ -E_r^p \cos(\alpha_i) \end{pmatrix}; \quad \mathbf{E}_t = \begin{pmatrix} E_t^p \sin(\alpha_t) \\ E_t^s \\ -E_t^p \cos(\alpha_t) \end{pmatrix} \quad (1.30)$$

Since, Eq. (1.29) means that the tangential components of the wave fields at the interface (x-y-plane) are continuous one gets two equations

$$(E_i^p - E_r^p) \sin(\alpha_i) - E_t^p \sin(\alpha_t) = 0 \quad (1.31)$$

and

$$E_i^s + E_r^s - E_t^s = 0 \quad (1.32)$$

We can derive two more equations from the boundary conditions of the magnetic field vector \mathbf{H} . To get \mathbf{H} Maxwell's equation (1.2) can be used for plane waves which leads to

$$\mathbf{B} = \frac{\mathbf{k} \times \mathbf{E}}{\omega} \quad (1.33)$$

Inserting (1.19), (1.20) and (1.30) into (1.33) we get

$$\mathbf{B}_i = \frac{k}{\omega} \begin{pmatrix} -E_i^s \sin(\alpha_i) \\ E_i^p \\ E_i^s \cos(\alpha_i) \end{pmatrix}; \quad \mathbf{B}_r = \frac{k}{\omega} \begin{pmatrix} E_r^s \sin(\alpha_i) \\ E_r^p \\ E_r^s \cos(\alpha_i) \end{pmatrix}; \quad \mathbf{B}_t = \frac{nk}{\omega} \begin{pmatrix} -E_t^s \sin(\alpha_t) \\ E_t^p \\ E_t^s \cos(\alpha_t) \end{pmatrix} \quad (1.34)$$

Considering that the permeability μ is the same on both sides of the interface, and excluding surface currents the boundary condition (1.15) becomes

$$\hat{\mathbf{n}} \times (\mathbf{B}_i + \mathbf{B}_r - \mathbf{B}_t) = 0 \quad (1.35)$$

Thus, the tangential components of \mathbf{B} are continuous at the interface. With (1.34) we have

$$(-E_i^s + E_r^s) \sin(\alpha_i) + nE_t^s \sin(\alpha_t) = 0 \quad (1.36)$$

and

$$E_i^p + E_r^p - nE_t^p = 0 \quad (1.37)$$

From the four equations (1.31), (1.32), (1.36), and (1.37) the ratio of the reflected and transmitted field components to the incident field components can be calculated. They are called Fresnel coefficients

$$r_s = \frac{E_r^s}{E_i^s} = \frac{\sin(\alpha_i) - n \sin(\alpha_t)}{\sin(\alpha_i) + n \sin(\alpha_t)} \quad (1.38)$$

$$t_s = \frac{E_t^s}{E_i^s} = \frac{2 \sin(\alpha_i)}{\sin(\alpha_i) + n \sin(\alpha_t)} \quad (1.39)$$

$$r_p = \frac{E_r^p}{E_i^p} = \frac{n \sin(\alpha_i) - \sin(\alpha_t)}{n \sin(\alpha_i) + \sin(\alpha_t)} \quad (1.40)$$

$$t_p = \frac{E_t^p}{E_i^p} = \frac{2 \sin(\alpha_i)}{n \sin(\alpha_i) + \sin(\alpha_t)} \quad (1.41)$$

Since, in the X-ray region n is almost unity there is no difference between the two polarizations and they are therefore indistinguishable for any practical case and no more subscripts -s and -p are used in the following. Sometimes its more convenient to use the Fresnel coefficients in dependence of the z-components of the wavevectors, i.e. $k_{i,z} = k \sin(\alpha_i)$ and $k_{t,z} = nk \sin(\alpha_t)$. Multiplying Eq. (1.38) and (1.39) with k/k gives

$$r = \frac{k_{i,z} - k_{t,z}}{k_{i,z} + k_{t,z}} \quad (1.42)$$

$$t = \frac{2k_{i,z}}{k_{i,z} + k_{t,z}} \quad (1.43)$$

1.4. Evanescent wave

Now we take a closer look to the transmitted wave, especially in the region of total external reflection. Assuming an s-polarized incident wave \mathbf{E}_i (i.e. field vector has just a y-component; as mentioned before there is no difference to p-polarization) then the transmitted wave is

$$\mathbf{E}_t(\mathbf{r}, t) = t\mathbf{E}_i e^{i(\mathbf{k}_t \cdot \mathbf{r} - \omega t)} \quad (1.44)$$

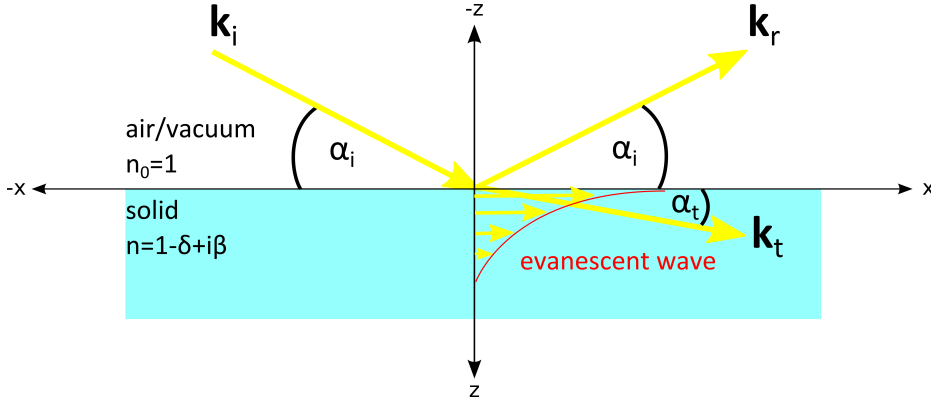


Figure 1.2.: A plane wave with wavevector \mathbf{k}_i hits a surface and is split into a reflected (\mathbf{k}_r) and transmitted wave (\mathbf{k}_t). Below the critical angle of total external reflection, the transmitted wave travels parallel to the surface (x-direction) and is exponentially damped in z-direction (evanescent wave).

For the wavevector \mathbf{k}_t one gets using Snell's law (1.25)

$$\mathbf{k}_t = k \begin{pmatrix} n \cos(\alpha_t) \\ 0 \\ n \sin(\alpha_t) \end{pmatrix} = k \begin{pmatrix} \cos(\alpha_i) \\ 0 \\ \sqrt{n^2 - 1 + \sin^2(\alpha_i)} \end{pmatrix} \quad (1.45)$$

The x-component of the transmitted wavevector is the same as the x-component of the incident wavevector. For the z-component we can write using Eq.(1.11) (neglecting δ^2 -, $\delta\beta$ - and β^2 -terms)

$$k_{t,z} = k \sqrt{n^2 - 1 + \sin^2(\alpha_i)} \approx k \sqrt{\sin^2(\alpha_i) - 2\delta + 2i\beta} \quad (1.46)$$

Therefore, the transmitted wave becomes

$$\mathbf{E}_t(\mathbf{r}) \propto t e^{i(k \cos(\alpha_i)x + \text{Re}\{k_{t,z}\}z)} e^{-\text{Im}\{k_{t,z}\}z} \quad (1.47)$$

Neglecting absorption ($\beta = 0$) and for small angles we have ($\alpha_c^2 = 2\delta$)

$$k_{t,z} \approx k \sqrt{\alpha_i^2 - \alpha_c^2} \quad (1.48)$$

Thus, for an incident angle smaller than the critical angle ($\alpha_i < \alpha_c$) $k_{t,z}$ is purely imaginary. In this case Eq.(1.47) describes a wave traveling parallel to the surface in x-direction. In z-direction this wave is exponentially damped with a penetration depth l_i

$$l_i = \frac{1}{\text{Im}\{k_{t,z}\}} \quad (1.49)$$

This resulting transmitted wave is called **evanescent wave**.

Furthermore, the transmission function t shows a very interesting feature at the critical angle as can be seen in Figure 1.3(a). It has a pronounced maximum right at

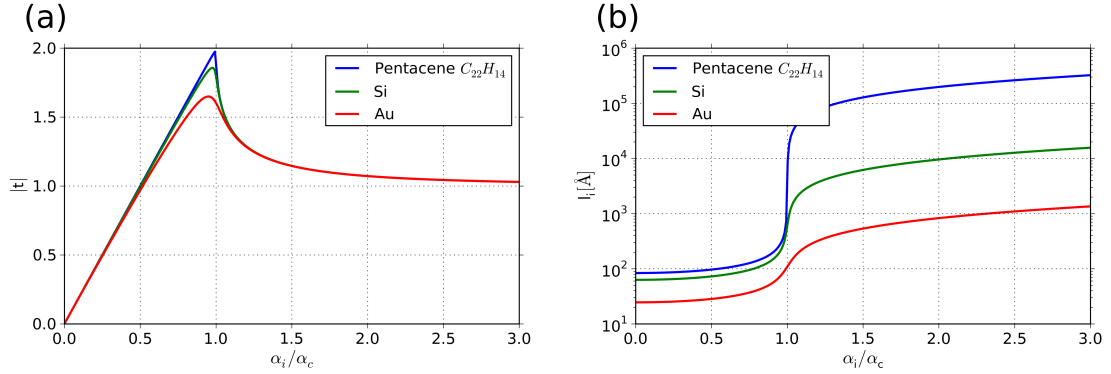


Figure 1.3.: (a) Absolute value of the transmission function and (b) penetration depth l_i for different materials as a function of the normalized angle of incidence α_i/α_c . (parameters for calculations (Tolan, 1999): $\lambda_{CuK\alpha} = 1.54\text{\AA}$; $\delta_{C_{22}H_{14}} = 4.3 \times 10^{-6}$, $\beta_{C_{22}H_{14}} = 0.63 \times 10^{-8}$; $\delta_{Si} = 7.6 \times 10^{-6}$, $\beta_{Si} = 17.3 \times 10^{-8}$; $\delta_{Au} = 49.6 \times 10^{-6}$, $\beta_{Au} = 511 \times 10^{-8}$)

the critical angle that originates from the coherent coupling of incident, reflected and transmitted wave fields (Dosch, 1992). As a result the amplitude of the transmitted wave is enhanced up to a factor of two. The penetration depth l_i of the wave is plotted in Figure 1.3(b). It is very low below the critical angle and increases tremendously after it. The asymptotic value is found with $l_{i0} = 1/(k\alpha_c) = \lambda/(2\pi\alpha_c)$ for $\alpha_i \rightarrow 0$. For Si this leads to an penetration depth of $l_{i0} \approx 60\text{\AA}$.

Summarized, the evanescent wave is enhanced up to an factor of two at the critical angel and travels parallel to the interface. Further, its penetration depth can be tuned by the incident angle. Below the critical angle it propagates only in the near-surface region. These facts are used in the so-called grazing incidence X-ray diffraction (GIXD) where the Bragg scattering of the evanescent wave is investigated. GIXD is a powerful tool to get informations about crystal surfaces and interfaces, and to study crystalline thin films and monolayers.

1.5. Reflectance and Transmittance

One might wonder how the transmission coefficient of the evanescent wave can reach a value up to two without violating the conservation of energy. However, regarding energy flow one has to calculate the Poynting vector \mathbf{S} (Hecht, 2002)

$$\mathbf{S} = c^2 \epsilon \mathbf{E} \times \mathbf{B} \quad (1.50)$$

Its magnitude is the power per unit area crossing a surface whose normal is parallel to \mathbf{S} . Furthermore, the irradiance or radiant flux density (W/m^2), i.e. the intensity we can measure with a detector, is given by the time-averaged value of the magnitude of the Poynting vector. For large integration time it is (Hecht, 2002)

$$I \equiv \langle S \rangle_T = \frac{c_m^2 \epsilon_m}{2} |E|^2 \quad (1.51)$$

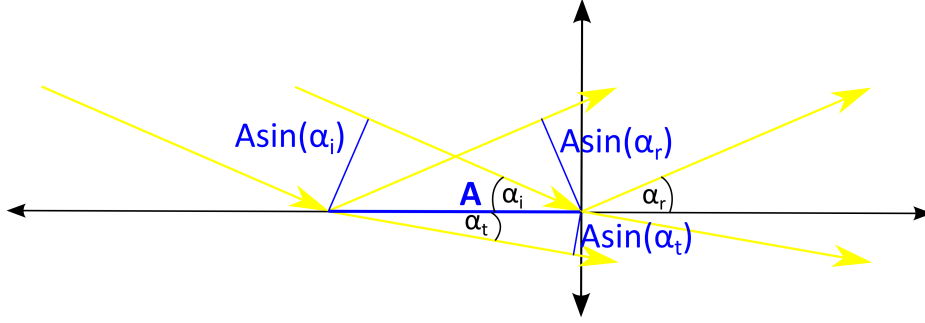


Figure 1.4.: Reflection and transmission of an incident beam. The beam cross-section arriving at an area A on the surface are indicated.

The irradiance is the average energy per unit time per unit area normal to \mathbf{S} . In our case we have I_i , I_r and I_t the incident, reflected and transmitted radiant flux density, respectively. Considering now the energy per time arriving at a surface area A we have to multiply the irradiance with the corresponding beam cross-section (see Figure 1.4). E.g. $I_i A \sin(\alpha_i)$ is the energy per unit time (power) flowing in the incident beam and arriving on the surface over A . We define the reflectance (reflectivity) R as the ratio of the reflected power to the incident power

$$R = \frac{I_r A \sin(\alpha_r)}{I_i A \sin(\alpha_i)} \quad (1.52)$$

and the transmittance T as the ratio of the transmitted power to the incident power

$$T = \frac{I_t A \sin(\alpha_t)}{I_i A \sin(\alpha_i)} \quad (1.53)$$

Since $\alpha_i = \alpha_r$ and $c_i \epsilon_i = c_r \epsilon_r$ R (1.52) is

$$R = \frac{|E_r|^2}{|E_i|^2} = |r|^2 \quad (1.54)$$

For T we get if we assume $\mu_i = \mu_t = \mu_0$ and thus $\mu_0 \epsilon_t = 1/c_m^2$ and $\mu_0 \epsilon_t c_t = n/c_0$

$$T = \frac{n \sin(\alpha_t)}{\sin(\alpha_i)} \frac{|E_t|^2}{|E_i|^2} = \frac{n \sin(\alpha_t)}{\sin(\alpha_i)} |t|^2 \quad (1.55)$$

Regarding the conservation of energy, the total energy flowing into the area A per time must be equal to the reflected plus transmitted

$$I_i A \sin(\alpha_i) = I_r A \sin(\alpha_r) + I_t A \sin(\alpha_t) \quad (1.56)$$

thus

$$|E_i|^2 \sin(\alpha_i) = |E_r|^2 \sin(\alpha_r) + n |E_t|^2 \sin(\alpha_t) \quad (1.57)$$

$$1 = \frac{|E_r|^2}{|E_i|^2} + \frac{n \sin(\alpha_t)}{\sin(\alpha_i)} \frac{|E_t|^2}{|E_i|^2} \quad (1.58)$$

This is

$$1 = R + T \quad (1.59)$$

which shows the conservation of energy (in the whole calculation absorption was neglected). Here we found out that $T \neq |t|^2$. Summarized, this is because first the speeds with which the energy is transported is not the same and second the cross sections of incident and transmitted beam are different due to refraction. R is much simpler to handle since $R = |r|^2$. R is sometimes also referred to as Fresnel reflectivity.

For the case of the evanescent wave no energy is carried across the interface. If we would calculate the Poynting vector we would see that the energy actually circulates back and forth across the interface, resulting in a zero net flow (Hecht, 2002).

1.6. X-ray reflectivity from surfaces

In this section we take a closer look to the reflectivity of X-rays from surfaces. By measuring the specular reflectivity (specular means that the angle of incident is equal to the exit angle) one gets information about layer thickness and the index of refraction, i.e. the vertical electron density distribution of a material. Therefore, X-ray reflectivity (XRR) is a powerful tool to investigate thin films and interfaces. Here we will first derive the reflectivity of a homogeneous slab and then the reflectivity of a multilayer stack where we introduce Parratt's recursive formalism (Parratt, 1954) which is widely used in XRR evaluation softwares. Furthermore, the influence of roughness on the reflectivity is shortly discussed.

1.6.1. X-ray reflectivity of a homogeneous slab

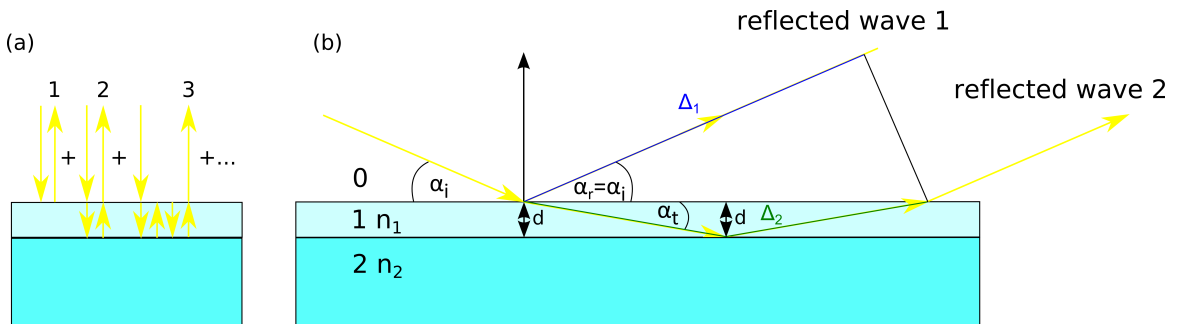


Figure 1.5.: (a) Reflection from a slab of finite thickness. To obtain the total reflectance all possible waves have to be summed up. The first three waves are indicated. (b) First and second reflected wave are indicated. Their path difference is $\Delta = \Delta_2 - \Delta_1$. From the path difference the phase factor can be calculated.

We consider a finite homogeneous slab of thickness d characterized by a index of refraction n_1 on top of a infinite slab with index of refraction n_2 . Contrary to the case of a infinite slab, which we have treated when deriving the Fresnel coefficient r (1.42), we have now a infinite series of reflections possible. Thus, we have to sum up all these wave amplitudes to get the total amplitude reflectivity as it is indicated in Figure 1.5(a) (Als-Nielsen & McMorrow, 2001). For the reflected waves amplitudes we get :

wave 1: We have a reflection at the interface 0 to 1 with amplitude r_{01} .

wave 2: First we have a transmission at the interface 0 to 1 with t_{01} , then a reflection at the interface 1 to 2 with r_{12} and finally a transmission at the interface 1 to 0 with t_{10} . If we want to add this wave to the first wave we have to include the proper phase factor. It can be calculated from the optical path difference. As indicated in Figure 1.5 the path difference is $\Delta = \Delta_2 - \Delta_1 = \frac{2nd}{\sin(\alpha_t)} - \frac{2nd \cos^2(\alpha_t)}{\sin(\alpha_t)} = 2nd \sin(\alpha_t)$. This leads to a phase $\varphi = 2\pi/\lambda\Delta$ and therefore a phase factor $p^2 = e^{i\varphi} = e^{i4\pi/\lambda n \sin(\alpha_t)d} = e^{i2k_{1,z}d}$, with $k_{1,z}$ the z-component of the wavevector inside the slab.

wave 3: We have transmission at the interface 0 to 1, t_{01} , reflection at the interface 1 to 2, r_{12} , reflection at the interface 1 to 0, r_{10} , followed by another reflection at the interface 1 to 2, r_{12} , and finally transmission at the interface 1 to 0 with t_{10} . As phase factor we have p^4 .

Accordingly, the total amplitude reflectivity is the sum of all possible reflected waves (Als-Nielsen & McMorrow, 2001)

$$r_{total} = r_{01} + t_{01}t_{10}r_{12}p^2 + t_{01}t_{10}r_{10}r_{12}^2p^4 + t_{01}t_{10}r_{10}^2r_{12}^3p^6 + \dots \quad (1.60)$$

$$= r_{01} + t_{01}t_{10}r_{12}p^2(1 + r_{10}r_{12}p^2 + r_{10}^2r_{12}^2p^4 + \dots) \quad (1.61)$$

$$= r_{01} + t_{01}t_{10}r_{12}p^2 \sum_{n=0}^{\infty} (r_{10}r_{12}p^2)^n \quad (1.62)$$

The sum can be identified as a geometric series ($\sum_{i=0}^{\infty} x^i = 1/(1-x)$; for $-1 < x < 1$ (Bartsch, 2004)), so we get

$$r_{total} = r_{01} + t_{01}t_{10}r_{12}p^2 \frac{1}{1 - r_{10}r_{12}p^2} \quad (1.63)$$

For r_{01} we have (1.42)

$$r_{01} = \frac{k_{0,z} - k_{1,z}}{k_{0,z} + k_{1,z}} \quad (1.64)$$

and therefore

$$r_{01} = -r_{10} \quad (1.65)$$

and with

$$r_{01}^2 + t_{01}t_{10} = \frac{(k_{0,z} - k_{1,z})^2}{(k_{0,z} + k_{1,z})^2} + \frac{4k_{0,z}k_{1,z}}{(k_{0,z} + k_{1,z})^2} = \frac{(k_{0,z} + k_{1,z})^2}{(k_{0,z} + k_{1,z})^2} = 1 \quad (1.66)$$

inserted into (1.63) we get

$$r_{total} = \frac{r_{01} + r_{12}p^2}{1 + r_{01}r_{12}p^2} \quad (1.67)$$

From the phase factor we see that the total amplitude reflectivity is oscillating due to interferences of the waves reflected at the top and the bottom of the slab. This oscillations are called Kiessig-fringes (Kiessig, 1931). From its period the layer thickness can be determined $d = 2\pi/(2\Delta k) \approx \lambda/(2\Delta\alpha_i)$.

1.6.2. X-ray reflectivity from multilayers - Parratt's recursive formalism

Parratt (1954) introduced a recursive formalism to calculate the reflectivity of a multilayer composed of N layers sitting on a infinitely thick substrate. Each of this layers is characterized by a index of refraction $n_j = 1 - \delta_j + i\beta_j$ and a thickness d_j . We know from Section 1.4 that the x-component of the transmitted wavevector is conserved, i.e. it is the same in all N layers ($k_{j,x} = k_x$ for all j). The absolute value of the wavevector in the j layer is $k_j = n_j k$, where k is the absolute value of the wavevector in vacuum. So we get for the z-component of the wavevector in layer j (Als-Nielsen & McMorro, 2001)

$$k_{j,z}^2 = (n_j k)^2 - k_x^2 = (1 - \delta_j + i\beta_j)k^2 - k_x^2 \approx k_z^2 - 2\delta_j k^2 + i2\beta_j k^2 \quad (1.68)$$

where k_z is the z-component of the wavevector \mathbf{k} in vacuum, i.e. the wavevector of the wave impinging on the first layer of the multilayer stack. Excluding multiple reflections, we get from the Fresnel coefficient (1.42) the reflectivity of each layer as

$$r'_{j,j+1} = \frac{k_{j,z} - k_{j+1,z}}{k_{j,z} + k_{j+1,z}} \quad (1.69)$$

The prime denotes that it is the Fresnel coefficient where no multiple reflections are taken into account.

To obtain the total reflectivity of the multilayer stack we start with the reflectivity of the bottom of the N'th layer and the substrate and continue to include more and more layers so we get a recursion for the total reflectivity. Since the substrate is infinite thick there are no multiply reflections and we get

$$r'_{N,S} = \frac{k_{N,z} - k_{S,z}}{k_{N,z} + k_{S,z}} \quad (1.70)$$

where the subscript S denotes substrate. The z-components of the wavevector can be calculated using Eq. (1.68). For the reflectivity from the top of the N'th layer we get

with Eq. (1.67)

$$r_{N-1,N} = \frac{r'_{N-1,N} + r'_{N,S} p_N^2}{1 + r'_{N-1,N} r'_{N,S} p_N^2} \quad (1.71)$$

with the phase factor $p_N^2 = e^{i2k_N z d_N}$.

For the reflectivity of the next interface, the top of the N-1 layer we have

$$r_{N-2,N-1} = \frac{r'_{N-2,N-1} + r_{N-1,N} p_{N-1}^2}{1 + r_{N-2,N-1} r_{N-1,N} p_{N-1}^2} \quad (1.72)$$

with $p_{N-1}^2 = e^{i2k_{N-1} z d_{N-1}}$. This process can be continued recursively until we obtain the total reflectivity amplitude, $r_{0,1}$, at the interface between vacuum and the first layer (Als-Nielsen & McMorrow, 2001). The total specular reflected intensity R is proportional to $|r_{0,1}|^2$.

Parratt's recursive formalism is very powerful to refine measured specular reflectivity intensities of multilayers with a appropriate model. However, since the refinement is model based a good knowledge of the investigated system must be available a priori.

1.6.3. The influence of roughness on the reflectivity

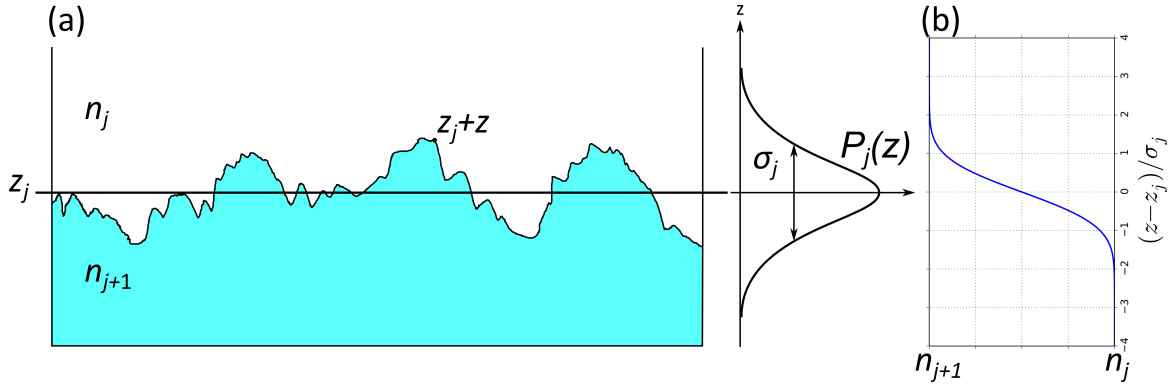


Figure 1.6.: (a) Rough interface, where z_j denotes the mean height. The real height shows fluctuations z around z_j . z is weighted by a probability distribution $P_j(z)$ as indicated. (b) If $P_j(z)$ is a Gaussian probability distribution the index of refraction changes continuously between two layers j and $j + 1$. This change can be described using the error function as shown in the graph.

Up to now we calculated reflectivity from perfectly flat interfaces. However, real interfaces are never perfectly flat. They will always have a certain amount of roughness. This roughness dampens the reflected intensity and further leads to off-specular reflections (diffuse scattering) which will not be treated in this work.

A perfectly sharp interface means that the index of refraction n_j of layer j jumps to a value n_{j+1} at the interface of layer j and $j + 1$. For a rough interface we have to replace this sharp step by a continuous variation of the refractive index.

The roughness of an interface can be described by replacing the z -coordinate of the interface z_j by $z_j + z$ where z is weighted by a probability density $P_j(z)$ see Figure 1.6(a) (Tolan, 1999). The mean value (μ_j) of it is

$$\mu_j = \int z P_j(z) dz \quad (1.73)$$

and we can define the root-mean-square (rms) roughness σ as

$$\sigma_j^2 = \int (z - \mu_j)^2 P_j(z) dz \quad (1.74)$$

We assume that z is normally (Gaussian) distributed random variable. We have

$$P_j(z) = \frac{1}{\sqrt{2\pi}\sigma_j} e^{-\frac{z^2}{2\sigma_j^2}} \quad (1.75)$$

Then the variation of the index of refraction can be described using the error function $erf(z) = \frac{2}{\sqrt{\pi}} \int_0^z e^{-t^2} dt$ (Tolan, 1999)

$$n_j(z) = \frac{n_j + n_{j+1}}{2} - \frac{n_j - n_{j+1}}{2} erf\left(\frac{z - z_j}{\sqrt{2}\sigma_j}\right) \quad (1.76)$$

The resulting continuous refractive index profile is plotted in Figure 1.6(b).

Now one can solve the Helmholtz equation (1.9) using the continuous refractive index profile $n(z)$ as it was done by Névot & Croce (1980). As result they found out that roughness damps the specular reflectivity by a factor $e^{-2k_{j,z}k_{j+1,z}\sigma_j^2}$ so that we get for the Fresnel coefficients

$$\tilde{r}_{j,j+1} = r_{j,j+1} e^{-2k_{j,z}k_{j+1,z}\sigma_j^2} \quad (1.77)$$

where $r_{j,j+1}$ is the Fresnel coefficient excluding roughness. This roughness factors can be easily included into Parratt's recursive formalism. More details about the influence of roughness on the reflectivity can be found in Tolan (1999). Sinha et al. (1988) took a different approach to investigated X-ray scattering from rough surfaces. They employed distorted-wave Born approximation and got the same damping factor as result for the specular reflectivity. There, also the off-specular reflectivity is treated in detail which is not the focus of this work.

1.7. X-Ray diffraction

In the previous sections we have treated the interaction of X-rays with matter in an exact way and showed the phenomena of refraction. In the following section X-ray scattering is considered in the weak scattering limit the so called kinematical or Born approximation where multiple scattering effects are neglected. This allows to derive a simple formalism to explain X-ray diffraction from crystals. In the end of this section we will extend this formalism to the distorted wave Born approximation (DWBA) to include refraction and give a proper formalism for evanescent X-ray scattering that has to be used to understand grazing incident X-ray diffraction experiments.

1.7.1. Kinematical X-Ray diffraction

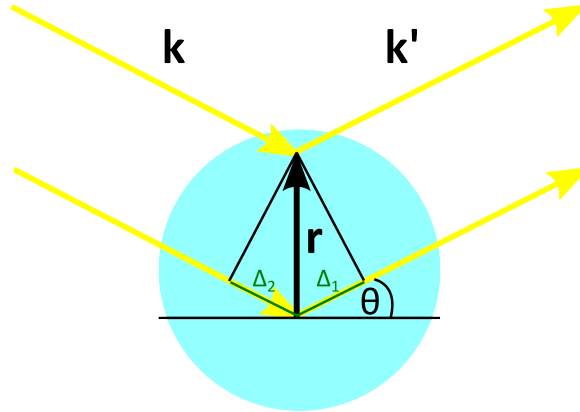


Figure 1.7.: Scattering from an atom. The incident wavevector \mathbf{k} and the scattered wavevector \mathbf{k}' are indicated. The path difference $\Delta = \Delta_1 + \Delta_2$ between the wave that is scattered in the origin and the wave scattered in \mathbf{r} is also indicated.

In the kinematical or Born approximation it is assumed that the wave that is scattered is the same inside the scattering sample as outside. That means that the transmitted wave and wavevector \mathbf{k} are the same inside the sample as in vacuum. Refraction is neglected. Furthermore, it is assumed that each element of the sample scatters the incoming wave and all these resulting scattered fields are summed up to get the total scattering. Multiple scattering is not considered.

To derive the formalism we start with scattering of X-rays by an electron. An incoming X-ray plane wave is scattered by an electron with a scattering amplitude of $-r_e$ (the minus sign means that incident field and the radiated field are 180° out of phase) (Als-Nielsen & McMorrow, 2001). r_e is the Thomson scattering length or classical electron radius, which was already introduced in Eq. (1.12). We consider now the scattering from an atom, which (in a very classical description) has an electron density distribution $\rho(\mathbf{r})$. So a volume element $d\mathbf{r}$ at \mathbf{r} contributes $-r_e\rho(\mathbf{r})d\mathbf{r}$ to the scattered field. To get the total scattering amplitude we have to integrate over the whole volume including the proper phase factor. In Figure 1.7 the scattering

from a atom is indicated. For the phase difference between the wave scattered in the origin and the wave scattered at \mathbf{r} we get $\Delta\varphi = 2\pi/\lambda(\Delta_1 + \Delta_2)$ which is the same as $\Delta\varphi = (\mathbf{k}' - \mathbf{k}) \cdot \mathbf{r} = \mathbf{q} \cdot \mathbf{r}$ (the scalar product of the two vectors \mathbf{q} and \mathbf{r}) where \mathbf{k} is the wavevector of the incident wave and \mathbf{k}' is the wavevector of the scattered wave. We have introduced the wavevector transfer or scattering vector

$$\mathbf{q} = \mathbf{k}' - \mathbf{k} \quad (1.78)$$

Thus, we get for the total scattering amplitude of an atom

$$-r_e f^0(\mathbf{q}) = -r_e \int \rho(\mathbf{r}) e^{i\mathbf{q} \cdot \mathbf{r}} d\mathbf{r} \quad (1.79)$$

$f^0(\mathbf{q})$ is the atomic form factor in units of the Thomson scattering length $-r_e$.

In the same way we can calculate the scattering amplitude of a molecule. The atoms organized into a molecule are labeled by j , thus we get

$$F^{mol}(\mathbf{q}) = \sum_{r_j} f_j(\mathbf{q}) e^{i\mathbf{q} \cdot \mathbf{r}_j} \quad (1.80)$$

where $f_j(\mathbf{q})$ is the atomic form factor of the j 'th atom.

Finally, we consider the scattering of a crystal lattice. A crystal lattice can be constructed by regularly repeating a basic structural units called unit cell. The points where the unit cells are located form a lattice. In real space a 3D lattice is specified by a set of vectors \mathbf{R}_n with (Als-Nielsen & McMorrow, 2001):

$$\mathbf{R}_n = n_1 \mathbf{a}_1 + n_2 \mathbf{a}_2 + n_3 \mathbf{a}_3 \quad (1.81)$$

where \mathbf{a}_1 , \mathbf{a}_2 and \mathbf{a}_3 are the lattice vectors and n_1 , n_2 and n_3 are integers.

For the scattering amplitude of a crystal lattice we have

$$F^{crystal}(\mathbf{q}) = \sum_{r_j} F_j^{mol}(\mathbf{q}) e^{i\mathbf{q} \cdot \mathbf{r}_j} \sum_{\mathbf{R}_n} e^{i\mathbf{q} \cdot \mathbf{R}_n} \quad (1.82)$$

where $F_j^{mol}(\mathbf{Q})$ is the molecular (or atomic) form factor and \mathbf{r}_j the position of the j 'th molecule (or atom) in the unit cell. In Eq. (1.82) the first term is the unit cell structure factor which represents the scattering amplitude from the basis of molecules in the unit cell and the second term is known as lattice sum. The scattered intensity is proportional to the square of the scattering amplitude

$$I \propto |F^{crystal}|^2 \quad (1.83)$$

The square of the lattice sum, also called Laue function can be written as:

$$\left| \sum_{n_1, n_2, n_3} e^{i\mathbf{q} \cdot (n_1 \mathbf{a}_1 + n_2 \mathbf{a}_2 + n_3 \mathbf{a}_3)} \right|^2 = \frac{\sin^2(\frac{n_1 \mathbf{q} \cdot \mathbf{a}_1}{2})}{\sin^2(\frac{\mathbf{q} \cdot \mathbf{a}_1}{2})} \frac{\sin^2(\frac{n_2 \mathbf{q} \cdot \mathbf{a}_2}{2})}{\sin^2(\frac{\mathbf{q} \cdot \mathbf{a}_2}{2})} \frac{\sin^2(\frac{n_3 \mathbf{q} \cdot \mathbf{a}_3}{2})}{\sin^2(\frac{\mathbf{q} \cdot \mathbf{a}_3}{2})} \quad (1.84)$$

For a perfect crystal where n_1, n_2 and n_3 are infinite this function is zero except if

$$\mathbf{q} \cdot \mathbf{a}_1 = 2\pi h, \quad \mathbf{q} \cdot \mathbf{a}_2 = 2\pi k, \quad \mathbf{q} \cdot \mathbf{a}_3 = 2\pi l \quad (1.85)$$

where h, k , and l are integers. This diffraction conditions suppose to construct a lattice in the wave vector space spanned by basis vectors \mathbf{a}_1^* , \mathbf{a}_2^* and \mathbf{a}_3^* which fulfill $\mathbf{a}_i \cdot \mathbf{a}_j^* = 2\pi\delta_{ij}$ with the Kronecker delta δ_{ij} , defined so that $\delta_{ij} = 1$ if $i = j$ and zero otherwise. It may be shown that

$$\mathbf{a}_1^* = 2\pi \frac{\mathbf{a}_2 \times \mathbf{a}_3}{\mathbf{a}_1 \cdot \mathbf{a}_2 \times \mathbf{a}_3}, \quad \mathbf{a}_2^* = 2\pi \frac{\mathbf{a}_3 \times \mathbf{a}_1}{\mathbf{a}_1 \cdot \mathbf{a}_2 \times \mathbf{a}_3}, \quad \mathbf{a}_3^* = 2\pi \frac{\mathbf{a}_1 \times \mathbf{a}_2}{\mathbf{a}_1 \cdot \mathbf{a}_2 \times \mathbf{a}_3} \quad (1.86)$$

satisfy the conditions and the points of this so called **reciprocal lattice** are specified by vectors of the type

$$\mathbf{G} = h\mathbf{a}_1^* + k\mathbf{a}_2^* + l\mathbf{a}_3^* \quad (1.87)$$

It is apparent that the reciprocal lattice vector \mathbf{G} satisfy Eq. (1.85) and therefore

$$\mathbf{q} = \mathbf{G} \quad (1.88)$$

This is the **Laue condition** for observation of X-ray diffraction. It may be shown that $|\mathbf{G}| = 2\pi/d_{hkl}$ where d_{hkl} is the lattice spacing of the planes with Miller indices h, k, l (Als-Nielsen & McMorrow, 2001). With the latter, Eq. (1.84) and the fact that for elastic scattering ($|\mathbf{k}'| = |\mathbf{k}|$; $k = 2\pi/\lambda$) $\mathbf{q} = 2k \sin(\theta)$ (see Figure 1.7), with the scattering angle 2θ (angle between \mathbf{k} and \mathbf{k}'), the well known **Bragg condition** can be derived.

$$2d_{hkl} \sin(\theta) = \lambda \quad (1.89)$$

Bragg's law Eq. (1.89) describes x-ray diffraction in real space, which is expressed as the Laue condition Eq. (1.88) in reciprocal space. That is, Bragg reflection takes place when the sample is placed in such a position that the scattering vector \mathbf{q} ends in any reciprocal lattice point. Therefore, it is very convenient to understand diffraction phenomena in reciprocal space instead of real space.

Reciprocal lattice of a single crystal

The reciprocal lattice of a single crystal are points in the reciprocal space as indicated in Figure 1.8 for two different families of lattice plane. To measure diffracted intensities of a family of lattice plane the scattering vector \mathbf{q} has to intersect one of the corresponding reciprocal lattice points to fulfill the Laue condition (1.88). Thus, the orientation and length of the scattering vector \mathbf{q} has to be changed by orienting the sample and choosing the right scattering angle 2θ .

Reciprocal lattice of a powder

A powder consist of crystallites that are randomly oriented. Therefore, the reciprocal lattice consists of spheres of different radius as shown in Figure 1.8(b). Each sphere

represents one lattice plane distance. To observe diffraction only the length of the scattering vector has to be changed. The orientation of \mathbf{q} is not important because the scattering vector will intersect the spheres of the reciprocal lattice as soon as it has the appropriate length. Since $|\mathbf{q}| = 4\pi/\lambda \sin(\frac{2\theta}{2})$ just the scattering angle 2θ has to be changed continuously to measure all possible Bragg reflections.

Reciprocal lattice of a 2d powder

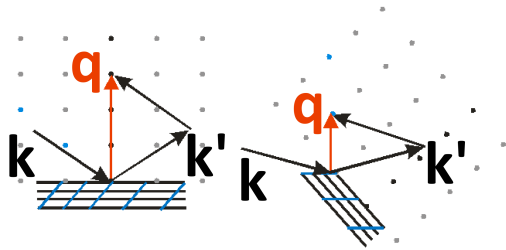
Two dimensional powders are typically found in organic thin films grown on isotropic substrates. In a 2 d powder all crystallites are oriented with the same lattice plane family parallel to the surface. Their azimuthal orientations are random. This is illustrated in Figure 1.8(c₁). The reciprocal lattice of a 2 d powder is a set of rings as shown in Figure 1.8(c₂). The radii of the rings is determined by the in-plane component $q_p = \sqrt{q_x^2 + q_y^2}$ of the scattering vector \mathbf{q} . The height of the rings is given by the z-component q_z .

To measure all Bragg diffractions of a 2 d powder in-plane diffraction is necessary, where the in-plane component of the scattering vector \mathbf{q} is changed. From conventional specular X-ray diffraction (XRD) experiments only one lattice plane distance can be determined, because in specular XRD (i.e. angle of incidence equal to exit angle) the scattering vector is always perpendicular to the sample surface and only its length changes but not its directions. So, for the case of 2 d powders in specular XRD only diffraction features from one lattice plane family could be observed.

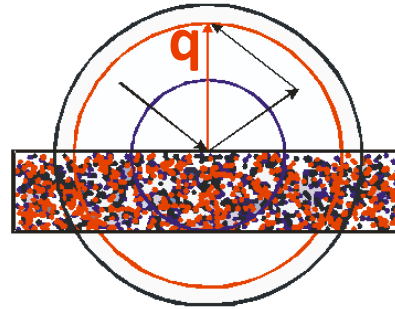
Reciprocal lattice of a 2d crystal

A two dimensional crystal (e.g. crystalline monolayer) in real space is just a set of points lying in one plane (see Figure 1.8(d)). If we assume that the lattice vector \mathbf{a}_3 is along the surface normal the monolayer has no repetition in this direction. We can set n_3 in Eq. 1.84 equal to unity and the diffraction is then independent of $\mathbf{q} \cdot \mathbf{a}_3$, which is the component of the scattering vector perpendicular to the surface. In reciprocal space we find a lattice of rods (Robinson & Tweet, 1992) which are often referred to as Bragg rods. Perpendicular to the surface these rods are continuous and in both directions parallel to the surface the rods are sharp. We can measure diffraction features if the scattering vector \mathbf{q} intersects this rods. This is only possible when performing in-plane diffraction experiments. In normal specular XRD no diffraction features are observed because in a monolayer there is no repetition perpendicular to the surface. A powerful technique to investigate the in-plane structure of crystalline monolayers is grazing incident in-plane X-ray diffraction (GIXD) as we will see in the next section.

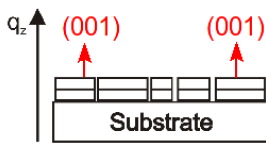
(a) single crystal



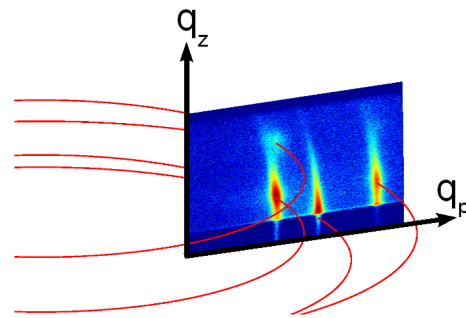
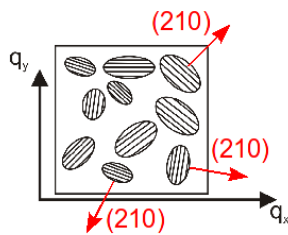
(b) powder



(c₁)



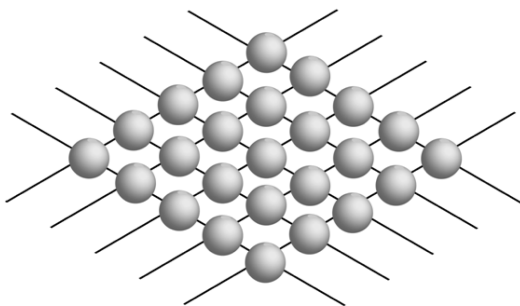
2 d powder (c₂)



(d)

2 d crystal

real space



reciprocal space

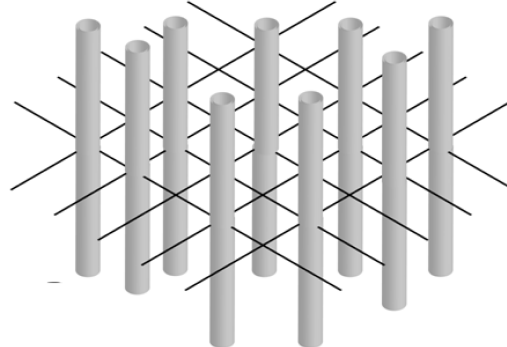


Figure 1.8.: Reciprocal lattice of (a) a single crystal, (b) a powder, (c) a 2 d powder and (d) real and reciprocal lattice of a 2 d crystal like a crystalline monolayer (pictures taken from Moser (2008) and Fleisch (2010)).

1.7.2. Evanescent X-ray scattering

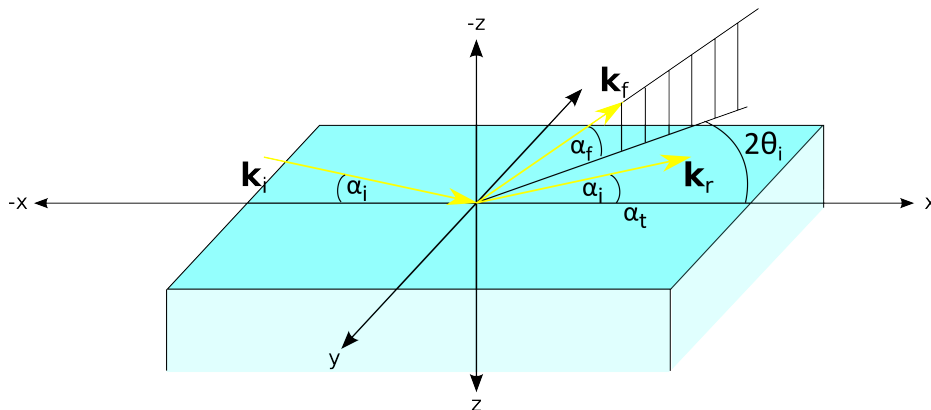


Figure 1.9.: Schematic of grazing incident in-plane scattering geometry. \mathbf{k}_i , \mathbf{k}_r , and \mathbf{k}_f are the wavevectors of the incident, reflected and scattered waves, respectively. $2\theta_i$ is the in-plane scattering angle.

We have already introduced the evanescent wave in Section 1.4. There we have seen that for an incident angle smaller than the critical angle the resulting transmitted wave in a medium travels parallel to the surface and penetrates just a few tens of Angstrom depending on the angle of incident into the material. Furthermore, this evanescent wave is enhanced up to a factor of two. Therefore, it is perfectly suited to use it for surface sensitive diffraction experiments, e.g. to investigate the crystalline structure of monolayers. However, evanescent X-ray diffraction can not be treated in the kinematical approximation because in the kinematical approximation refraction phenomena are neglected. To keep the easy formalism of kinematical approximation it has to be extended. Vineyard (1982) treated grazing incidence diffraction in the distorted wave Born approximation (DWBA). In DWBA the scatterer is first replaced by a simpler distribution (characterized by n). Then the field that is produced when an incident wave field falls on this distribution is calculated exactly. The resulting field is called the distorted wave. It is now considered that the distorted wave illuminates the real scatterer and produces scattered waves that are summed up over all elements of the scatterer as before in the kinematical (Born) approximation.

Mathematically, this can be described by splitting up the index of refraction (Dosch, 1987)

$$n(\mathbf{r}) = n + \Delta n(\mathbf{r}) \quad (1.90)$$

where n is the average value of the index of refraction and $\Delta n(\mathbf{r})$ is the spacial deviation of it that causes scattering. In Figure 1.9 a schematic of the grazing incident scattering geometry is shown. The incident beam $\mathbf{E}_i(\mathbf{r})$ impinge on the surface under an angle of incidence smaller than the critical angle. The beam gets totally reflected and the evanescent wave $\mathbf{E}_t(\mathbf{r})$ travels parallel to the surface (in x-direction) in a very small near surface layer. The evanescent wave is the distorted wave in the DWBA and it gets scattered from every near surface scattering cross section. This scattered wave

$\mathbf{E}_f(\mathbf{r})$ can be observed under the in-plane scattering angle 2θ and a grazing exit angle α_f . To describe this scattering one gets with the split index of refraction (1.90) and the Helmholtz equation (1.9) an inhomogeneous Helmholtz equation (Dosch, 1987)

$$\nabla^2 \mathbf{E}_f(\mathbf{r}) + k^2 n^2 \mathbf{E}_f(\mathbf{r}) = -k^2 \Delta n^2(\mathbf{r}') \mathbf{E}_t(\mathbf{r}') \quad (1.91)$$

The solution of this Eq. (1.91) is derived in detail in Dietrich & Wagner (1984). Summarized, the amplitude of the resulting scattered wave becomes

$$E_f \propto t(\alpha_i) t(\alpha_f) F(\mathbf{q}') \quad (1.92)$$

and the Intensity

$$I \propto |t(\alpha_i)|^2 |t(\alpha_f)|^2 |F(\mathbf{q}')|^2 \quad (1.93)$$

where $t(\alpha_i)$ is the Fresnel transmission coefficient (1.43) for the angle of incident α_i and $t(\alpha_f)$ the Fresnel transmission coefficient for the exit angle α_f and $F(\mathbf{q}')$ the scattering amplitude we know already from the kinematical approximation

$$F(\mathbf{q}') = \int \Delta\rho(\mathbf{r}) e^{i\mathbf{q}' \cdot \mathbf{r}} d\mathbf{r} \quad (1.94)$$

where $\Delta\rho(\mathbf{r})$ is the spatial variation of the electron density that causes the scattering. \mathbf{q}' is the scattering vector inside the crystal

$$\mathbf{q}' = \mathbf{k}'_f - \mathbf{k}_t \quad (1.95)$$

and k'_f the refracted wave vector of the scattered wave

$$\mathbf{k}'_f = k \begin{pmatrix} \cos(\alpha_f) \cos(2\theta_i) \\ \sin(\alpha_f) \cos(2\theta_i) \\ -\sqrt{n^2 - 1 + \sin^2(\alpha_f)} \end{pmatrix} \quad (1.96)$$

similar to \mathbf{k}_t (1.45).

An interesting feature in the scattered amplitude (1.92) is the appearance of two transmission functions. One for the angle of incidence α_i and one for the exit angle α_f . That can be explained with reciprocity principle in optics. Because, if the source and the point of observation are interchanged, the same amplitude must result (Dosch, 1987). The transmission function of the exit angle α_f leads to the increased scattered intensity when $\alpha_f = \alpha_c$. This horizon of increased intensity is known as Yoneda reflection (Yoneda, 1963) and is typically seen in gracing incidence reciprocal space maps at very low q_z values (see Figure 1.10(a)).

Figure 1.10(b) shows the enhancement of the scattered intensity in dependence of the angle of incidence α_i . There, the scattered intensity measured at one specific q_p -position is shown as a function of α_i . Along the exit angle α_f the intensity was integrated. Therefore, $I \propto |t(\alpha_i)|^2$ and the absolute square of the transmission function (1.43) could be fitted to the data. It can clearly be seen that there is a strong

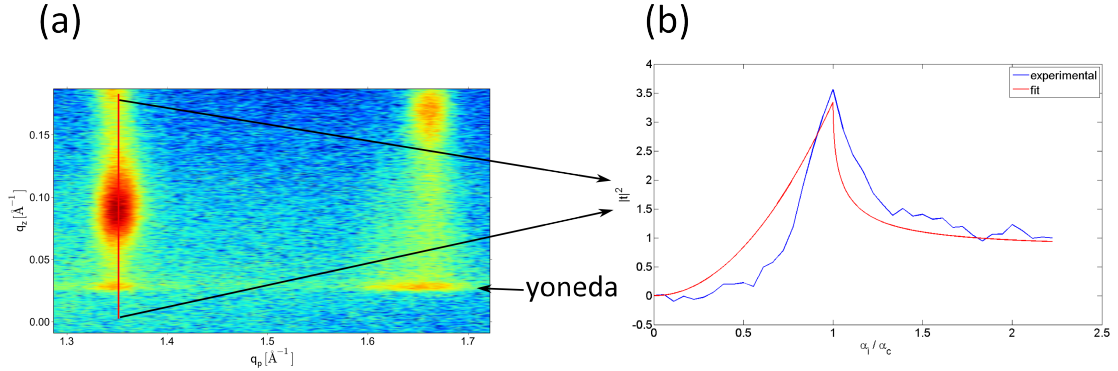


Figure 1.10.: (a) Grazing incidence reciprocal space map of pentacene. The Yoneda reflection is visible at $q_z \approx 0.025 \text{ \AA}^{-1}$. (b) The detector was moved to the indicated position in $q_p = 1.35 \text{ \AA}^{-1}$ and the angle of incidence was scanned to demonstrate the enhancement of the diffracted signal at the critical angle. For each α_i -value the detected diffracted intensity was integrated over the whole detector range. Then the transmission function was fitted to this profile.

enhancement at the critical angle. In this case, where we investigated pentacene, the scattered intensity is enhanced almost up to a factor of 3.5. This clearly demonstrates the power of this technique, because due to this enhancement also samples with low scattering volume (i.e. scattered intensities) like monolayers can be investigated.

A qualitative explanation for the appearance of the two transmission functions in the amplitude of the scattered wave can be given if we consider the scattering of first layer of atoms/molecules of a material. To get the total scattered amplitude we have to take into account different possible scattering events. In Figure 1.11 these events are illustrated. Fig. 1.11(a) shows the scattering directly at the first layer. We assume this happens with an amplitude f . In Fig.1.11(b) the incident wave is first reflected at the layers below the first layer with $r(\alpha_i)$ and then scattered by the atoms/molecules of the first layer. In Fig. 1.11(c) the incident wave is first scattered from the atoms/molecules towards the bulk material and then reflected from the bulk with $r(\alpha_f)$. In the last event we consider (Fig.1.11(d)) the incident wave gets first reflected by the bulk with $r(\alpha_i)$ then scattered by the first layer downwards and reflected again with $r(\alpha_f)$. For the whole scattering amplitude we have to sum up all these events and get

$$F = f(1 + r(\alpha_i) + r(\alpha_f) + r(\alpha_i)r(\alpha_f)) = f(1 + r(\alpha_i))(1 + r(\alpha_f)) \quad (1.97)$$

From Eq.(1.42) and Eq.(1.43) we know that $t = 1 + r$, thus we get

$$F = ft(\alpha_i)t(\alpha_f) \quad (1.98)$$

Summarized, DWBA keeps the simplicity of kinematical approximations where scattering can easily be understood in reciprocal space, however it adds the influence of refraction to it. In grazing incident in-plane X-ray diffraction (GIXD) DWBA has to

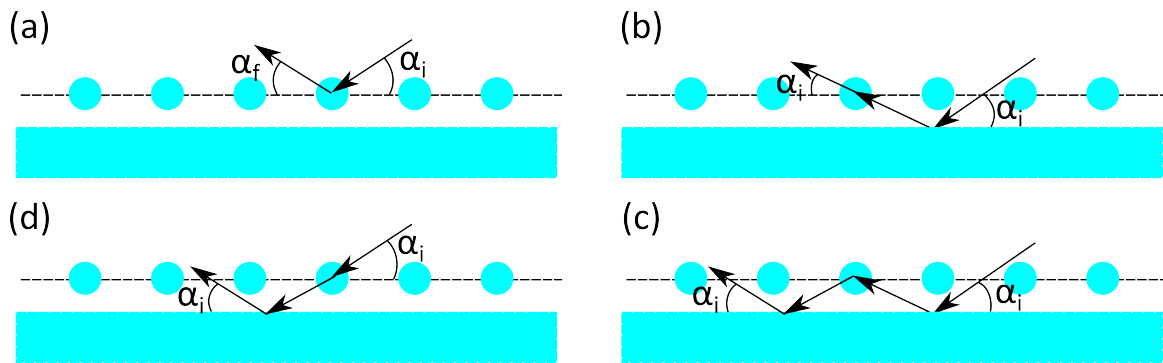


Figure 1.11.: Schematic of the possible different scattering events from the first layer of atoms/molecules of a material.

be used and we have seen that surface sensitive enhanced scattering can be observed. Therefore, GIXD is the perfect tool to investigate the in-plane structure of thin films and monolayers. Since, the critical angle of total external reflection are very small a high collimated X-ray beam is required for GIXD. Therefore, normally GIXD is only performed at synchrotron radiation facilities of high brilliance. In this work we will show that the use of sophisticated X-ray optics allows to perform X-ray experiments also with standard laboratory equipment.

2. Experimental setups

In this chapter a detailed description of all used experimental X-ray setups is given. Thereby, a special focus lies on the grazing incidence in-plane X-ray diffraction (GIXD) setup, which is fully based on standard laboratory equipment. Part of this whole work was the optimization and assembly of it. A manual how to align the setup and how to perform measurements are given in the Appendix A. Additionally, the diffractometer used in this introduced GIXD setup can be converted to normal specular geometry. The procedures of rebuilding and alignment are described accurately in Appendix B.

Furthermore, short descriptions of the used HASYLAB DORIS W1 beamline and specular X-ray reflectivity diffractometer setup Empyrean by Panalytical are given.

2.1. Bruker Grazing incidence in-plane X-ray diffraction setup

The GIXD setup is based on a commercial 4-circle Bruker D8 Discover diffractometer upgraded with the Bruker Ultra GID add-on, which allows rotating the X-ray tube to set the angle of incidence (α_i) of the X-ray beam towards the substrate surface. It is possible to tune the angle of incidence between -3.5° to 6.5° with a resolution better than 0.01° while keeping the sample horizontal; the schematic of the experimental setup is illustrated in Figure 2.1.

A conventional 2.2 kW, water-cooled X-ray tube with copper anode in line focus mode is used as X-ray source. The divergent X-ray beam emitted from the line-shaped source is collimated by a 60 mm long parabolic graded multilayer mirror (Schuster & Gobel, 1995), leading to an out-of-plane divergence better than 0.025° . In addition, the multilayer mirror acts as monochromator, which suppresses the intensity of Cu-K β radiation to less than 1% of the Cu-K α radiation. The in-plane incoming beam divergence is adjusted by Soller slits to 0.35° . The resulting beam has dimensions of 1.1 mm in height and 12 mm in width and can be limited in height by a vertical slit after the multilayer mirror. The reached flux density of the X-ray beam is 8.6×10^6 photons/(s mm²).

The sample is attached on an Eulerian cradle with a sample stage that allows translations in all 3 directions x, y, z and rotations around the vertical axis (φ). In addition, the sample holder can be tilted in two perpendicular directions (ξ, ζ) to align the sample surface normal to the rotation axis (φ).

To reduce measurement time, a one-dimensional position sensitive detector (PSD) Vantec-1 (Khazins et al., 2004) is used to collect scattering intensity profiles along

2. EXPERIMENTAL SETUPS

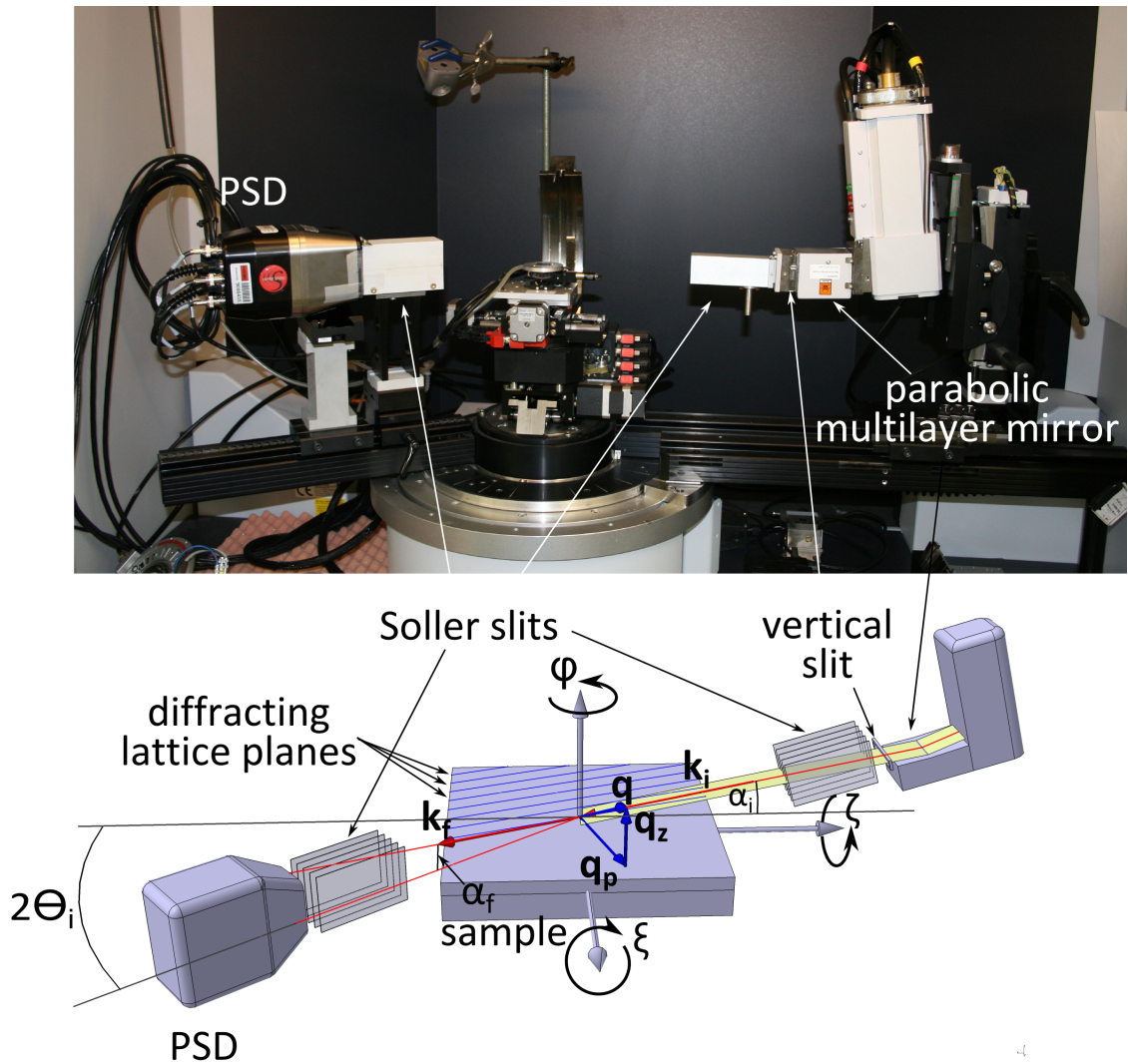


Figure 2.1.: Photograph and schematic of the experimental setup. The wave vectors of the incident wave and a scattered wave (\mathbf{k}_i and \mathbf{k}_f , respectively), the corresponding momentum transfer \mathbf{q} , and its in-plane and out-of-plane components (\mathbf{q}_p and \mathbf{q}_z , respectively), as well as the probed lattice planes are indicated. A detailed description is given in the text.

the out-of-plane direction with a resolution of $\Delta\alpha_f = 0.007^\circ$. The PSD's angular resolution is calibrated by scanning the X-ray's angle of incidence (α_i) from the lowest to the highest possible value, i.e., by scanning the (attenuated) primary X-ray beam over the whole detector range. So, a linear dependency between the detector read-out channels and the exit angle (α_f) can be calculated. In our present setup, the PSD covers an out-of-plane range (α_f) of 7.3° in one single shot. A set of Soller slits in front of the PSD defines the angular in-plane detector acceptance to 0.35° .

The presented scattering geometry probes lattice planes that are nearly perpendicular to the sample surface, as indicated in Figure 2.1. Thus, this setup is perfectly suited to characterize the in-plane order of epitaxially grown films as well as two dimensional powders (i.e., fiber-textured films).

2.1.1. Experimental data processing

The experimental results of the GIXD measurements are visualized and analyzed using the custom-made software PyGid (Moser, 2011) that allows transformation to q-space, indexation of Bragg peaks as well as intensity extraction into horizontal and vertical directions. Furthermore, the one dimensional PSD calibration scan can be analyzed directly inside the program by fitting a linear dependency between detector read out channels and exit angle as described above. The program PyGid is based on python programming language that allows an easy and fast upgrade and modification of the code. The support of Bruker *raw*-files was added by using the portable library xylib (Zhang & Wojdyr, 2008). So it is possible to directly import data collected with the one-dimensional PSD Vantec-1 and the original Bruker control software XRD commander.

In the following GIXD data are shown as reciprocal space maps (RSMs) as a function of the in-plane component q_p and out-of-plane component q_z of the momentum transfer vector \mathbf{q} (Figure 2.1).

Refraction correction

With the software PyGid it is possible to calculate reciprocal lattice point for any given lattice constants and indicated them in reciprocal space maps. So comparisons with measured diffraction features are possible. Further, if *Crystallographic Information Files* (Hall & McMahon, 2005) for the crystal are available the intensity of each expected diffraction spot can be indicated. Thus, we can compare measured diffraction intensities ($I \approx |F(\mathbf{q})|^2$) to references.

We have seen in Section 1.7.2 that for GIXD the scattering amplitude $F(\mathbf{q}')$ depends on the scattering vector \mathbf{q}' inside the crystal. For small angles of incident α_i and exit angles α_f refraction plays a non negligible role. We know from Eq.(1.95) that $\mathbf{q}' = \mathbf{k}'_f - \mathbf{k}_t$. The in-plane component q_p is not affected by refraction however the out-of-plane component. With Eq.(1.96) and Eq.(1.45) we have for the out-of-plane

component (neglecting absorption)

$$q'_z = k \left(\sqrt{\sin^2(\alpha_f)^2 - \alpha_c} + \sqrt{\sin^2(\alpha_i)^2 - \alpha_c} \right) \approx k \left(\sqrt{\alpha_f^2 - \alpha_c^2} + \sqrt{\alpha_i^2 - \alpha_c^2} \right) \quad (2.1)$$

Assuming that the angle of incident $\alpha_i = \alpha_c$ and $q_z \approx k\alpha_f$ (the z-component of the external scattering vector; the component we measure) we have

$$q'_z = \sqrt{q_z^2 - q_c^2} \quad (2.2)$$

where q_c is the corresponding value of α_c in q-space (q_z position of the Yoneda horizon). Diffraction data can be corrected using this equation (2.2) in PyGid by giving the Yoneda position as q_c . This correction helps to compare measured diffracted intensities to references pattern at low exit angle (α_f), where without correction the measured diffraction features are shifted to higher q_z -values due to refraction.

2.1.2. Flat field correction for 1d data of Vantec-1 detector

To measure grazing incidence in-plane reciprocal space maps 2θ scans were performed taking shots with the Vantec-1 detector at each 2θ step to collect intensity profiles along the out-of-plane direction. In these 2 dimensional maps lower background intensities in the middle of the detector were observed. Therefore, the detector's spatial sensitivity was investigated in more detail. For that purpose 2θ -scan through the attenuated direct beam were performed with the PSD in horizontal instead of a vertical position. This allowed to scan each detector read out channel through the same part of the direct beam. The scan was performed over a 2θ range from -8° to 8° with a step size of 0.05° taking a shot at each step for 60 s. This analysis is shown in Figure 2.2. Two different behaviors of the detector sensitivity were observed. If the direct beam was attenuated with 2 0.1 mm Cu absorber, leading to a count rate of ≈ 50 cps/pixel, no sensitivity decrease in the middle of the detector was observed, as can be seen in the integrated line scan in Figure 2.2(a). Only a stronger noise is observed in the middle. However, if the direct beam is attenuated with 3 0.1 mm Cu absorber, leading to a lower counting rate of 1-2 cps/pixel, a strong decrease of the detected intensity for the detector read out channels in the middle can be seen (Figure 2.2(b) line scan).

In conclusion, the detector spatial sensitivity strongly depends on the detected count rates. This behavior is very unfavorable behavior because we want to characterize thin organic films down to organic monolayers which show low scattering intensities.

To overcome this problem, recorded intensities were corrected using a flat-field correction to guarantee equal sensitivity over the whole detector range. That means the recorded intensities were divided by a sensitivity curve. This curve was obtained by measuring Fe-fluorescence, which leads to an isotropic irradiation of the detector. A small Fe-sample was mounted to the sample stage and the detector was moved in a 90° angle to the sample. Now the Fe sample was irradiated and the resulting fluorescence was measured. The measured intensities were normalized and interpolated to obtain

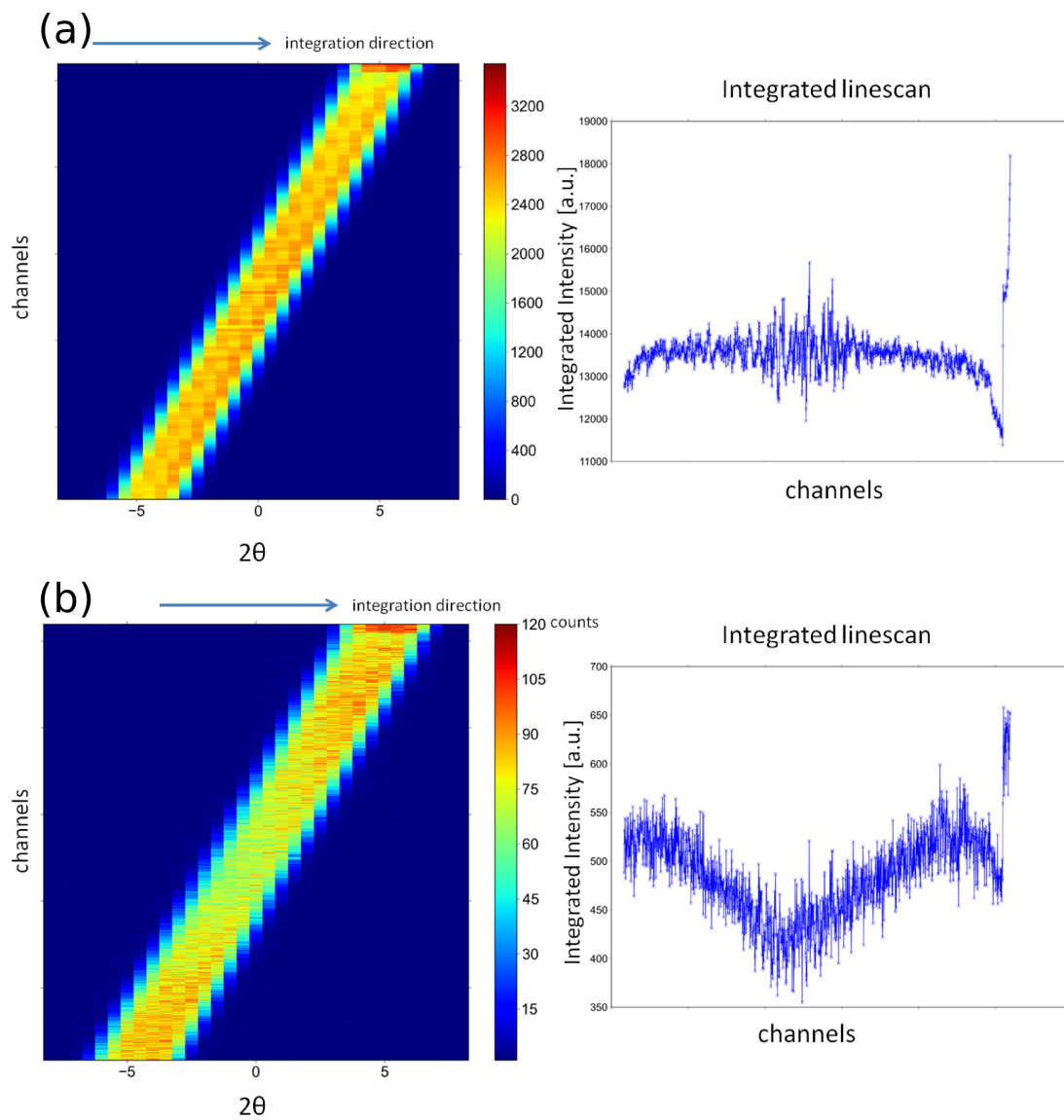


Figure 2.2.: 2θ -scan through direct beam with detector horizontal taking a shot at each step for 60s and integrated line scan. (a) direct beam attenuated with 2 0.1 mm Cu absorber (count rate ≈ 50 cps); (b) direct beam attenuated with 3 0.1 mm Cu absorber (maximal count rate = 1-2 cps)

a sensitivity value for each read out channel (see Figure 2.3). The whole flat-field correction was implemented into the software PyGid.

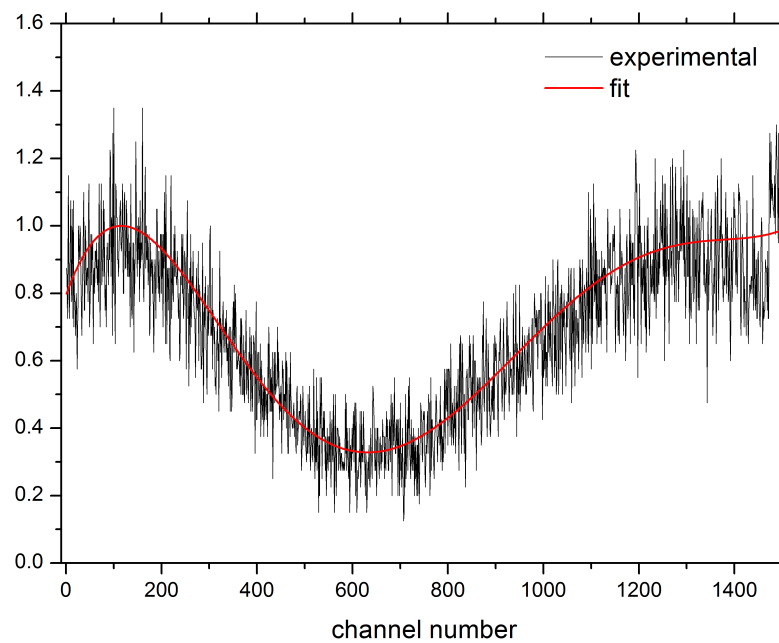


Figure 2.3.: Measurement of Fe-fluorescence detector and interpolation of the normalized experimental data (black line) to obtain the detector sensitivity curve (red line).

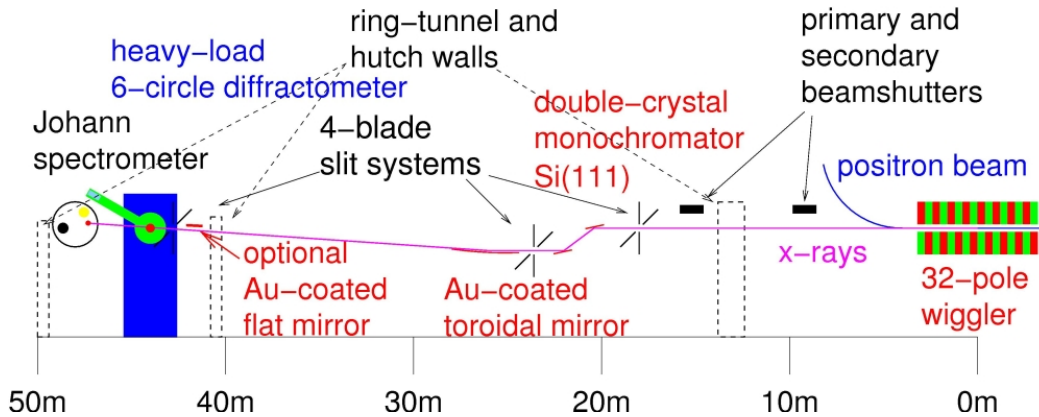


Figure 2.4.: Schematics of the HASYLAB Doris W1 beamline (picture taken from (HASYLAB-website, 2012)).

2.2. HASYLAB beamline W1

The HASYLAB synchrotron beamline W1 is situated at the DORIS III storage ring. The storage ring has a circumference of 289 meters and is designed to store positrons or electrons at an energy of 4.45 GeV in punched packages. Normally, 2 or 5 bunches of positrons are stored inside the ring with an initial beam current of up to 120 mA (HASYLAB-DORIS-website, 2012).

The HASYLAB beamline W1 uses a 32-pole wiggler as insertion device to generate a horizontally polarized white X-ray beam. For monochromatization a double crystal Si(111) monochromator is used, which allows to tune the X-ray energy between 4-11.5 keV. A toroidal mirror focuses the beam into a spot of approximately $1.6 \times 4 \text{ mm}^2$ at the position of the sample (HASYLAB-website, 2012), further a vertical and horizontal slit system can be used to limit the beam dimensions on the primary side. A sketch of the beamline is illustrated in Figure 2.4. During our experimental stay at the beamline the Johann spectrometer, also drawn in the sketch, was not used. Grazing incidence in-plane X-ray diffraction experiments were performed using a heavy load 6+2 circle diffractometer that was equipped with a Eulerian cradle and a sample stage. The sample stage can be covered with a X-ray transparent graphite dome to allow a constant flux of He inside the sample chamber (see Figure 2.5). The inert He-atmosphere reduces beam damages because it limits the formation of highly reactive ozone.

For detection a 1D-Mythen position sensitive detector (PSD) was employed that covers an out-of-plane range (α_f) of 4° in one shot. In front of the detector is an evacuated flight tube with a variable horizontal and vertical slit to set the in-plane resolution. The evacuated flight tube reduces unwanted air-scattering. In the used configuration the primary beam reaches a flux density of 3.1×10^{10} photons/(s mm²). The beamline provides a good trade-off between intensity and beam damage since beam damage plays a non negligible role in the characterization of organic materials using synchrotron radiation (Neuhold et al., 2011).

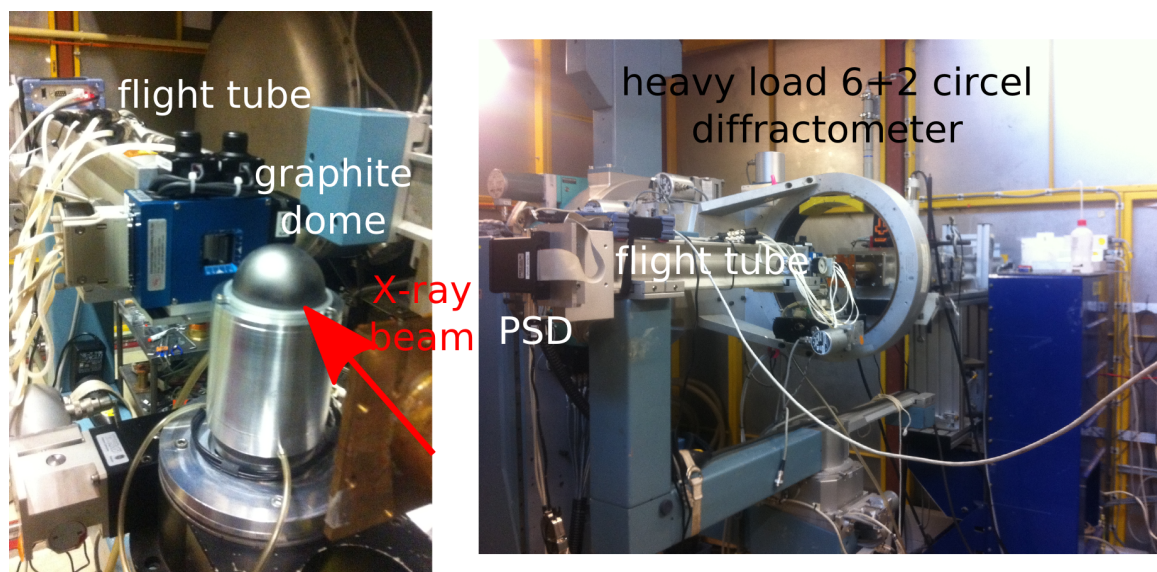


Figure 2.5.: Photographs of the HASYLAB beamline W1 experimental setup.

2.3. Panalytical Empyrean X-ray reflectivity setup

The Panalytical Empyrean is a 2 circle diffractometer, where the X-ray tube moves on the 2θ -circle and the detector on the θ -circle. In this geometry the sample always stays horizontal, which allows also to measure liquid samples. The whole setup is shown in Figure 2.6

The divergent X-ray beams emitted from the copper anode X-ray tube are collimated with a multilayer mirror. The sample is attached on a sample stage that can move in all 3 directions (x,y,z) and further rotate around a horizontal axis that lies within the scattering plane to align the sample. For detection a PIXcel^{3D} detector is employed that can be used in 0D mode as well as 1D and 2D mode. In front of the detector is a horizontal slit that determines the θ -resolution and vertical Soller slits as anti scatter slits to reduce detection of air scattering.

This setup is perfectly suited to perform X-ray reflectivity (XRR) experiments because due to its well collimated primary X-ray beam measurements at very low glancing angles are possible. In specular XRR $\theta/2\theta$ -scans are performed in a very low angular range (2θ from 0° - 10°) to probe the out-of-plane electron density as well as layer thickness and roughness of thin films.

Furthermore, specular X-ray diffraction (XRD) experiments are possible, which are in fact also $\theta/2\theta$ -scans but up to higher angles to probe lattice planes that are parallel to the sample surface. This is, because the scattering vector q always stays perpendicular to the surface and only its length changes but not its direction, as indicated in the sketch of Figure 2.6.

2.3. PANALYTICAL EMPYREAN X-RAY REFLECTIVITY SETUP

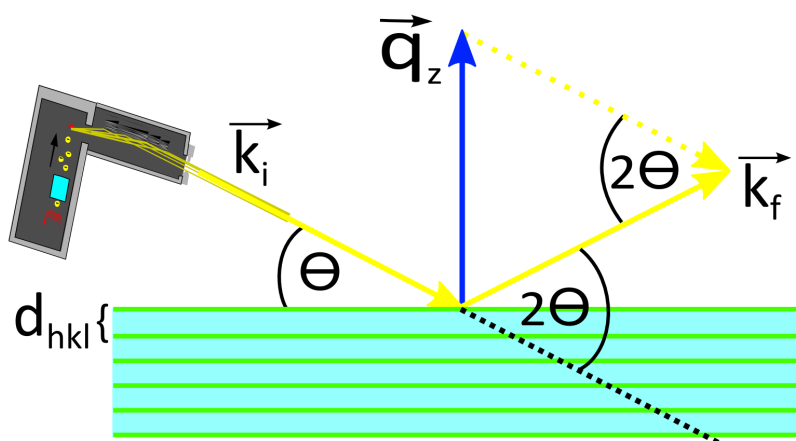
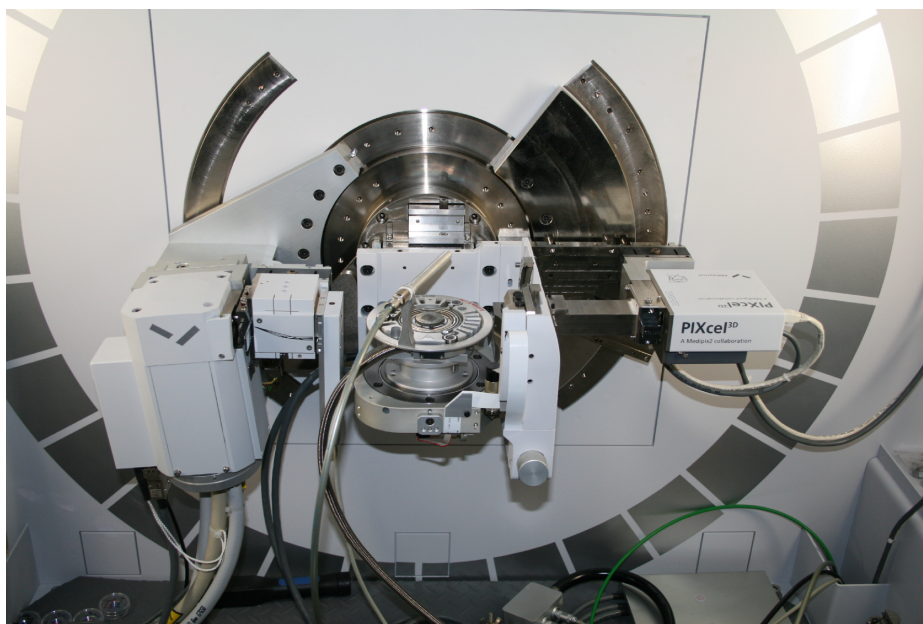


Figure 2.6.: Photograph and schematic of the Panalytical Empyrean XRR setup.

3. Experimental setup performance - results and details

3.1. Pentacene

Pentacene ($C_{22}H_{14}$) (see Figure 3.1), an organic semiconducting molecule consisting of five conjugated benzene rings is one of the most thoroughly studied materials in the field of organic electronics. Concerning organic field effect transistors it is one of the state-of-the-art materials reaching the highest mobility values necessary for high performance devices (Dimitrakopoulos et al., 1996; Gundlach et al., 1997; Braga & Horowitz, 2009). However, to get a better understanding of the electronic characteristics of an organic semiconductor it is important to know its structural properties, because charge transport is strongly influenced by the overlaps of molecular orbits of adjacent molecules (Mannsfield et al., 2009). In the case of pentacene, it exhibits several polymorphs slightly different from each other (Mattheus et al., 2001).

Pentacene deposited as thin film on SiO_2 grows as two dimensional powder making in-plane diffraction necessary to solve its crystal structure, as it was shown independently by Yoshida et al. (2007), Schiefer et al. (2007) and Nabok et al. (2007). In two dimensional powders all crystallites are oriented with the identical lattice plane parallel to the substrate surface while their azimuthal orientations (i.e., with respect to the sample surface) are statistically distributed. This specific growth mode is typically found for ordered organic monolayers or molecular crystals within thin-films grown on isotropic surfaces. In this case, complete crystallographic information can be revealed by in-plane diffraction at one specific azimuthal angle φ (Mannsfield et al., 2011; Salzmann et al., 2011; Moser et al., 2009).

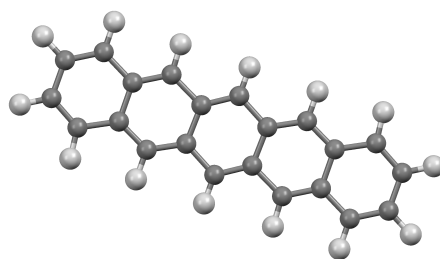


Figure 3.1.: Chemical structure of a pentacene ($C_{22}H_{14}$) molecule. Carbon atoms are represented as gray spheres, hydrogen as white ones.

3.1.1. Pentacene polymorphs

As already mentioned pentacene can be observed in several slightly different polymorphs depending on growth conditions and the used substrate (Mattheus et al., 2003). In this work we concentrate on two different polymorph. On the one hand the pentacene bulk phase, whose crystalline structure was solved by Campbell et al. (1962) and on the other hand the so called thin film phase that occurs in thin pentacene layers grown on isotropic SiO₂ substrates. Thin films are key elements in organic thin film transistors, thus, it is from high interest to know its crystalline structure for a better understanding of charge transport in such devices. However, since this thin film phase only occurs in thin layers grown on isotropic substrates (for that reason sometimes referred to as surface/substrate induced phase) it is not possible to grow large single crystals necessary for conventional full structure solutions. Furthermore, due to the thin film phase's growth as two dimensional powder, just one lattice plane distance can be determined using normal specular X-ray diffraction (XRD). This is because in specular XRD just lattice planes parallel to the surface are probed, which belong in the case of 2d powders all to the same lattice plane family. Therefore, other techniques have to be employed all having in-plane diffraction in common. Yoshida et al. (2007) suggested a full structural solution based on in-plane reciprocal space mapping and empirical force field calculations, Schiefer et al. (2007) applied GIXD and grazing incidence crystal truncation rod (GI-CTR) measurements and fitting, and Nabok et al. (2007) used a combination of GIXD and ab initio density functional theory (DFT) calculations. The triclinic lattice parameters reported in all the latter studies were obtained by GIXD measurements, pointing out once more the power of this experimental method and are listed in Table 3.1. There, also a comparison to the bulk phase is given. To determine the molecular arrangement within the unit cell different approaches were taken as mentioned above. It is reported that the triclinic unit cell, as for the bulk phase, contains two molecules that are packed in a herringbone structure (see Figure 3.2), which is characteristic for rod like molecules (Haber & Resel, 2008). The angle between two molecular planes (herringbone angle) is 50.0°, 54.3° or 54.1° and the molecular long axis tilts from the surface normal of the two independent molecules are 5.7° and 6.8°, 5.6° and 6.0° or 3.1° and 2.9° according to the studies of Yoshida et al. (2007), Schiefer et al. (2007) and Nabok et al. (2007), respectively. For the bulk phase the herringbone angle is 52.5° and the tilt angles 22.4° and 20.5°. So the molecules in the bulk phase are much more tilted, whereas in the thin film phase the molecules are almost upright standing. Therefore, in the thin film phase the intermolecular $\pi - \pi$ overlap is enhanced leading to a larger bandwidth of the topmost valence band and thus different electro-optical properties as it is pointed out by Nabok et al. (2007).

Table 3.1.: Comparison of the reported triclinic lattice parameters for the pentacene bulk phase (Campbell et al., 1962) and the pentacene thin film phase (Yoshida et al., 2007; Schiefer et al., 2007; Nabok et al., 2007).

Phase	$a / \text{\AA}$	$b / \text{\AA}$	$c / \text{\AA}$	α / deg	β / deg	γ / deg	$V / \text{\AA}^3$
Campbell et al. (1962)	6.079	7.893	14.78	83.20	79.92	94.40	692
Yoshida et al. (2007)	5.930	7.560	15.65	98.60	93.30	89.80	693
Schiefer et al. (2007)	5.958	7.596	15.61	81.25	86.56	89.80	697
Nabok et al. (2007)	5.920	7.540	15.63	81.50	87.20	89.90	689

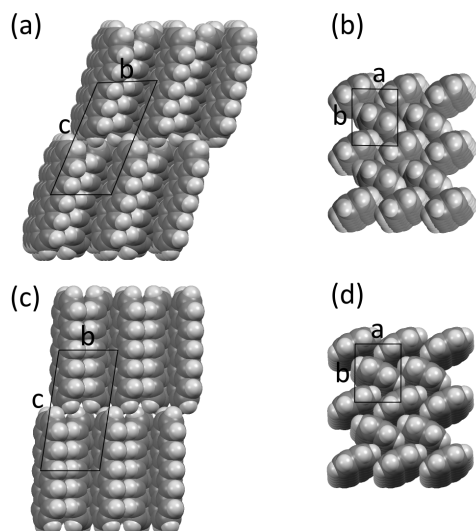


Figure 3.2.: Structure of two different pentacene polymorphs. (a) Side-view and (b) top-view of pentacene bulk phase (Campbell et al., 1962); (c) side-view and (d) top-view of pentacene thin film phase (Yoshida et al., 2007; Schiefer et al., 2007; Nabok et al., 2007).

3.1.2. Pentacene 50 nm thin-films

Since pentacene is a that well studied material, whose thin-film crystal structure was solved using in-plane diffraction, it is perfectly suited to use it as benchmark for our laboratory GIXD setup. In the following a structural study of 50 nm pentacene thin films is presented, fully performed using our laboratory setup. Further, a detailed comparison between synchrotron (HASYLAB Doris W1 beamline) and the laboratory measurements is given.

As sample a nominally 50 nm thick Pentacene film was prepared by vacuum deposition on a 20×20 mm² thermally oxidized silicon wafer. The reciprocal space map (RSM) of this layer measured with our laboratory GIXD setup can be seen in Figure 3.3(a). The measurement was carried out under ambient condition using an incidence angle of $\alpha_i = 0.17^\circ$, which corresponds to the critical angle of total external reflection of pentacene for Cu-K α radiation ($\lambda_{Cu-K\alpha} = 1.54178 \text{ \AA}$). The critical angle of total external reflection for a specific wavelength can be calculated by knowing the electron density ρ of the material using (Dosch, 1987)

$$\alpha_c = \lambda \cdot \sqrt{\frac{r_e \rho}{\pi}} \quad (3.1)$$

with $r_e = e^2/mc^2 = 2.82 \times 10^{-5} \text{ \AA}$ the classical electron radius and λ the wavelength of the radiation. For pentacene with 2×146 electrons per unit cell and a unit cell volume of 690 \AA^3 , one gets an electron density of $\rho = 0.423$ electrons/ \AA^3 and further $\alpha_c = 0.172^\circ$.

The vertical slit size that limits the primary X-ray beam height was chosen to 0.6mm leading in combination with this incidence angle to a 202 mm footprint of the direct beam on the sample surface plane. Therefore, with our 20×20 mm² sample only 10% of the incoming beam intensity is scattered from the sample and the usage of larger samples could be considered to further increase the scattered intensities.

The RSM was recorded over a $2\theta_i$ -range from 18° to 34° with a step-size of $\Delta 2\theta_i = 0.05^\circ$ and an integration time of 180s per step. Despite measuring under ambient conditions no degradation of the 50 nm pentacene thin-films due to beam damage was observed, however, the topics of degradation and beam damage are discussed in more detail in Section 3.1.5.

The transformation of the map from angular into q-space was done by the custom made software PyGid as it is described in Section 2.1.1 and the recorded intensities were corrected beforehand using a flat-field correction (Section 2.1.2).

In the RSM of the 50 nm pentacene thin film (Figure 3.3) the presence of a dominating thin film phase portion (black dots) and an additional less pronounced contribution of the bulk phase (white dots) can clearly be seen. All visible diffraction peaks can be explained and indexed with this two phases. The indexation was also done with the software PyGID using the unit cell parameters of Campbell et al. (1962) for the bulk phase and the parameters of Yoshida et al. (2007) for the thin film phase. The intensities of the diffraction features are in agreement with these solutions, as can be

seen by the radii of the rings around each dot which are proportional to the expected intensities.

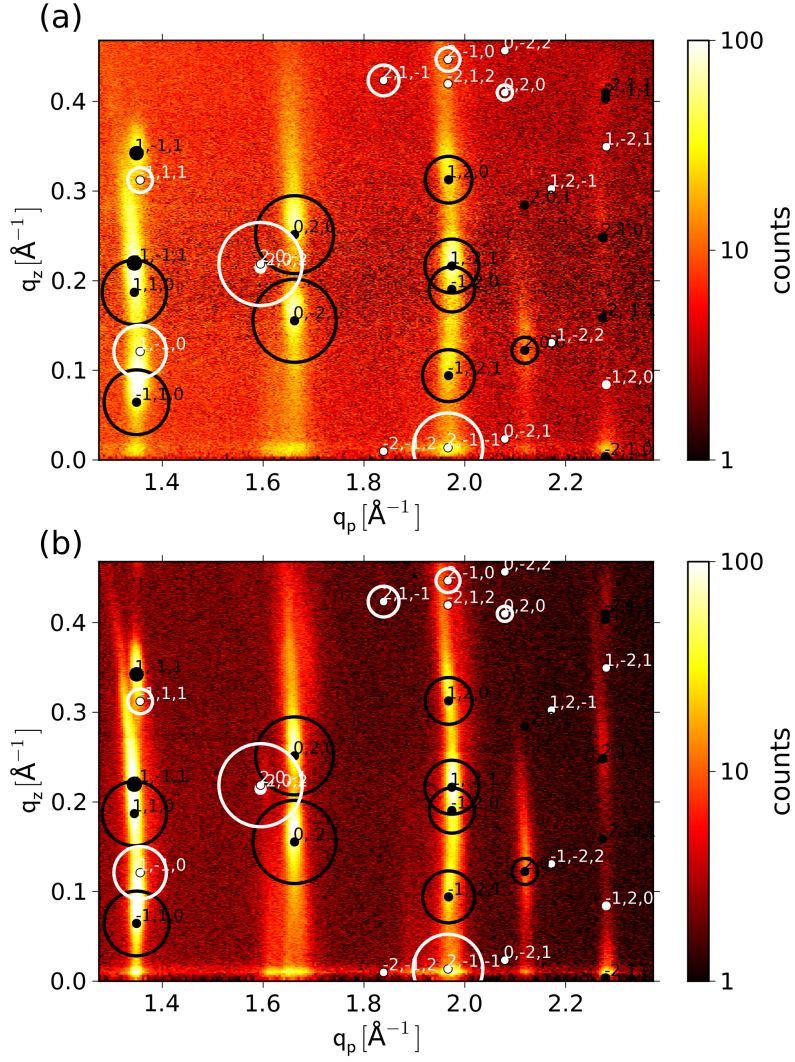


Figure 3.3.: Grazing incidence in-plane reciprocal space map of a 50 nm pentacene film grown on SiO_2 . (a) Measured with our laboratory setup and (b) measured at the HASYLAB Doris W1 beamline. Reflections corresponding to the pentacene thin film phase are indicated with black, bulk phase with white rings. The areas of the rings are proportional to the expected intensity.

Comparison between laboratory and synchrotron measurements

To compare the performance of our laboratory setup, the same pentacene thin film sample was mapped at the HASYLAB Doris W1 beamline, as it is shown in Figure 3.3(b). There, the used wavelength was $\lambda = 1.180\text{\AA}$, thus, the map was recorded over a $2\theta_i$ range from 13° to 26° with a step size of $\Delta 2\theta_i = 0.05^\circ$ to resolve the same range in reciprocal space as before. The integration time was 2 s per step and the whole measurement was carried out under He-atmosphere to avoid beam damage. As incidence angle $\alpha_i = 0.15^\circ$ was chosen, which is slightly above the critical angle of total external reflection for pentacene and the used wavelength ($\alpha_c = 0.13^\circ$).

Comparing the two RSM in Figure 3.3 they show exactly the same diffraction features and allow to draw the same conclusions about the presence of two phases. Both maps have the same logarithmic color scale, and show similar intensities at the diffraction peaks. Hence, a 50 times longer total measurement time in the laboratory (16.5 hours) than at the synchrotron (20 minutes) results in comparable quality, which is a reasonable measurement time for normal laboratories. The total measurement time of 20 minutes at the synchrotron is due to the fact that the detectors out-of-plane range is just 4° in comparison to 7.3° in the lab. Therefore, two vertically shifted in-plane scans (each 10 minutes) are necessary to map the same range as in the laboratory.

To get a more detailed comparison the RSMs were integrated along the q_z -direction from 0 \AA^{-1} to 0.46 \AA^{-1} . The resulting linescans, as depicted in Figure 3.4 for the case of the laboratory measurement, were fitted with a linear fit to determine the background and further each peak was fitted with a Lorentzian to get its full width at half maximum (FWHM), peak height, and peak area. This data analysis was performed with the fitting program *fityk* (Wojdyr, 2010) using a three parameter Lorentzian function to describe the peak shapes:

$$f(x) = \frac{\text{height}}{1 + \left(\frac{x-x_0}{FWHM/2}\right)^2} \quad (3.2)$$

In Figure 3.5 a comparison of the linescans fitted with Lorentzians after background subtraction is shown. The corresponding fit parameter are listed in Table 3.2.

The peak widths (FWHM) of the synchrotron data are smaller than the peaks of the laboratory measurement, e.g. 0.014 \AA^{-1} (HASYLAB) *versus* 0.024 \AA^{-1} (lab) for the first, 0.021 \AA^{-1} *versus* 0.03 \AA^{-1} for the second, and 0.018 \AA^{-1} *versus* 0.029 \AA^{-1} for the third peak. This is due to a worse in-plane resolution in the laboratory.

The in-plane resolution of the lab equipment is determined by Soller slits. Their angular acceptance has to be chosen as a trade-off between intensity (i.e., measurement time necessary to obtain requested measurement statistics) and resolution. The FWHM in reciprocal space of the first peak (0.024 \AA^{-1}) corresponds to 0.34° ($\Delta 2\theta = \lambda \Delta q / (2\pi \cos(2\theta/2))$) in angular space, i.e. exactly the angular acceptance of the Soller slits (0.35°). The FWHM of the second and third peak are slightly larger because of the presence of two polymorph structures of pentacene appearing

at similar q_p positions (compare Figure 3.3). Nevertheless, the in-plane resolution is highly sufficient to characterize organic thin films, although caution is advised when performing crystal size determinations by peak breadth analysis. The resolution limit for grain size analysis is reached if the experimentally determined peak broadening due to the crystal grain size (Δq_{exp} ; in terms of scattering vector) does not exceed the broadening due to the apparatus resolution (Δq_{res}) by at least 50% (Smilgies, 2009). Using

$$\Delta q_{hkl} = \sqrt{\Delta q_{exp}^2 - \Delta q_{res}^2} \quad (3.3)$$

with Δq_{hkl} the FWHM of a diffraction spot due to the average crystal grain size (D_{hkl}) and the well known Scherrer (1918) formula

$$D_{hkl} = \frac{2\pi K}{\Delta q_{hkl}} \quad (3.4)$$

with K the Scherrer constant (≈ 1) one can calculate an upper limit for the grain size that can be determined out of the peak broadening (Langford & Wilson, 1978). For the presented setup this leads to a maximum in-plane crystal size of 25 nm accessible to grain size determinations. Transverse shear force microscopy studies on pentacene monolayers vacuum deposited on SiO_2 report lateral crystalline domain sizes of 1-2 μm (Zhang et al., 2008; Wu et al., 2009), thus the observed peak broadening is purely caused by the in-plane resolution of the setup.

As a last point the integration time needed in the laboratory to obtain equivalent statistics to that of the synchrotron measurement was determined. The diffracted intensities of the RSM measured as counts were normalized to counts per second by dividing by the integration times. Again, integrated linescans were analyzed by fitting the (hkl)-rods. The obtained heights and areas of the fits are listed in Table 3.3, as well as the ratios between laboratory and synchrotron measurements of heights and areas for each peak. Taking a close look to these ratios one remarks a higher mean value of the height ratios than that of the area ratios. Although, normally it is better to compare peak areas than heights when comparing diffraction intensities, here one has to be careful because the peak areas are strongly related to the FWHM, which as mentioned above is determined by the in-plane resolution. Therefore, the ratios of the heights are more significant and in conclusion an around 100 times longer integration time is needed in the laboratory to obtain equivalent statistics to that of synchrotron measurements. This is still a reasonable timescale for normal laboratories and on the whole the comparison between laboratory and synchrotron measurements clearly showed the high potential of this setup for GIXD characterizations of thin films in the laboratory.

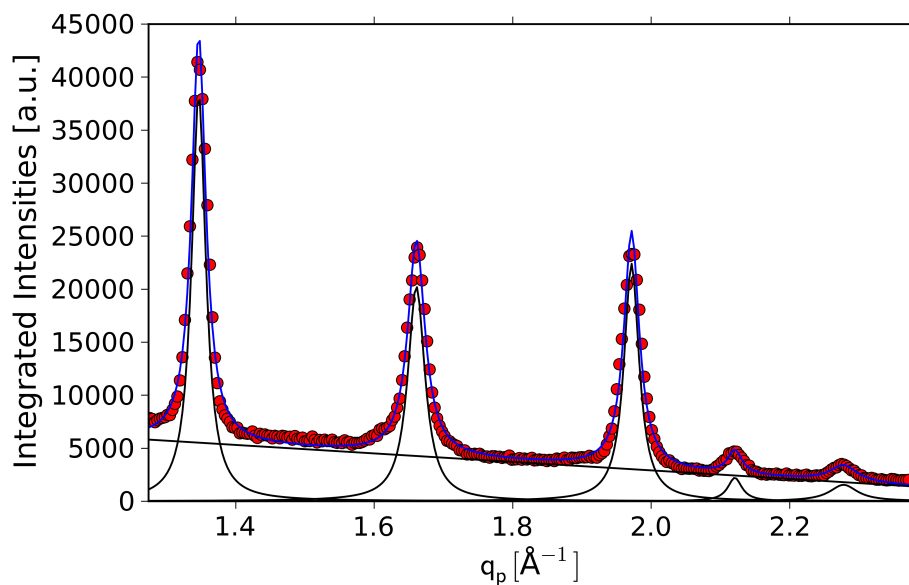


Figure 3.4.: Diffraction intensities of a 50 nm Pentacene film measured in the laboratory (see Figure 3.3) integrated over a q_z range from 0 \AA^{-1} to 0.46 \AA^{-1} (red dots). For the background a linear fit was used (black line) and the diffraction peaks were fitted with Lorentzian (black line; for fit parameters see Table 3.2). The sum of all fits is also shown as blue line.

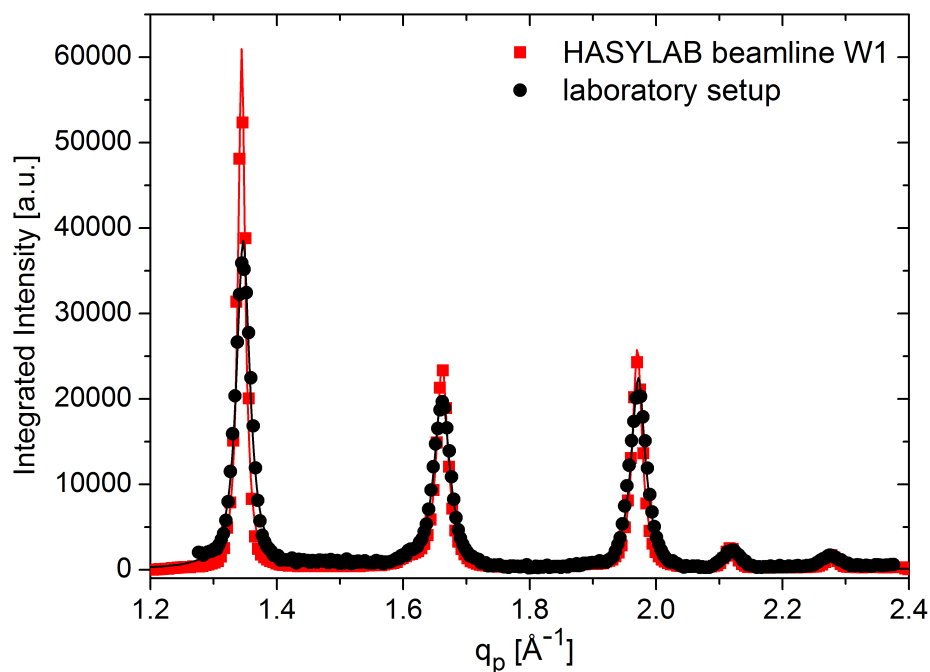


Figure 3.5.: Comparison between beamline W1 (HASYLAB) and laboratory measurements of 50 nm pentacene thin film (red squares and black dots, respectively). Intensities are integrated over a q_z range from 0 \AA^{-1} to 0.46 \AA^{-1} and afterwards corrected for the background. The peaks are fitted with Lorentzians (full lines).

Table 3.2.: Fit parameter of Lorentzian fits of the integrated Bragg rods for laboratory and synchrotron measurements (see Figure 3.5).

	$q_p / \text{\AA}^{-1}$	FWHM / \AA^{-1}	height	area
laboratory setup				
rod 11 l	1.347	0.024	38460	1502
rod 02 l	1.661	0.030	20259	955
rod 12 l	1.972	0.029	22396	933
rod 20 l	2.121	0.024	2212	85
rod 21 l	2.278	0.049	1542	118
HASYLAB W1				
rod 11 l	1.344	0.014	60917	1265
rod 02 l	1.662	0.021	23841	804
rod 12 l	1.971	0.018	25847	744
rod 20 l	2.118	0.019	2555	78
rod 21 l	2.278	0.031	1355	66

Table 3.3.: Analysis of the integration time needed for a equivalent statistic. The ratios of the fitted heights and areas are compared. In contrasts to Figure 3.5 and 3.4 the intensities were normalized to counts per second (cps) before integration over a q_z range from 0 \AA^{-1} to 0.46 \AA^{-1} .

	rod 11 l				
laboratory					
height / integrated cps	210	111	124	13	8
area	8.3	5.3	5.2	0.45	0.66
HASYLAB W1					
height / integrated cps	31882	12648	13391	1268	718
area	678	414	398	35.1	37.2
ratio height	152	114	108	98	90
ratio area	82	78	75	78	56

3.1.3. Pentacene mono- and multilayers

The phase analysis of 50 nm pentacene thin-films using our GIXD laboratory setup was very successful. Therefore, in a next step we wanted to test the setup's limits. In the following, a study of the 2 dimensional in-plane structure of pentacene mono- and multilayers films is presented. GIXD is the perfect tool to characterize the in-plane order of monolayers because it provides an enhanced surface sensitivity necessary to overcome the low scattering intensities of ultra-thin films and it probes lattice planes perpendicular to the sample surface (Als-Nielsen et al., 1994; Kaganer et al., 1999). Up to now GIXD studies on organic monolayers were only performed using synchrotron radiation facilities of high brilliance, thus, it was from high interest to test our laboratory setup with this well studied model system of pentacene mono- and multilayers.

Sample preparation

All samples were prepared at the Institute of Surface Technologies and Photonics, Weiz. There, nominal 1 monolayer (1ML), 2 ML, and 3 ML were vacuum deposited onto silicon wafers with 100 nm thermally grown silicon oxide (SiO_2). The SiO_2 -substrates were cleaned with acetone and opticlean beforehand. The vacuum during deposition was under 6.8×10^{-6} mbar and the substrate was heated to 65°C . The deposition rate for the first nominal ML ($\hat{=}1.3$ nm) was 0.1nm/90s, for the second ML 0.1nm/70s, and the third ML was deposited with a rate of 0.1nm/45s.

Pre-characterization

Before GIXD measurements the samples were characterized by atomic force microscopy (AFM) and specular X-ray reflectivity (XRR) experiments to get informations about the sample morphology. AFM micrographs of all three samples are shown in Figure 3.6(a),(c),(d). For the 1 ML sample the AFM investigation (3.6(a)) reveals a not fully covered first layer with small island grown on top. The line profile of the 1 ML sample Figure 3.6(b) shows a layer height of the first monolayer between 15-20 Å. The 2 and 3 ML sample (3.6(c),(d)) show a strong island growth typically for pentacene deposited on isotropic surfaces (Ruiz et al., 2004b). AFM data were analyzed using the free software WSXM (Horcas et al., 2007).

Specular XRR measurements were performed to probe the out-of-plane structure of the samples. These measurements, as shown in Figure 3.7, were performed on a Panalytical Empyrean diffractometer in $\theta/2\theta$ modus, using a step size of $\Delta 2\theta = 0.005^\circ$ and an integration time of 2 s per step. The evolution of an ordered three dimensional structure from 1 ML to 3 ML can clearly been followed by the occurrence of an increasing Bragg peak at $q_z \approx 0.38\text{\AA}^{-1}$ for the 2 ML and 3 ML sample. This also illustrates the sensitivity of specular X-ray diffraction to lattice planes parallel to the sample surface, which are not existent in 2 dimensional structures (e.g., monolayer)(Werzer et al., 2008). The high frequency oscillations (so called Kiessig fringes (Kiessig, 1931)) in the XRR curves are due to interferences of X-rays reflected from the 100nm thick

SiO₂ substrate. The lower frequency oscillations, which in the case of the 1 ML sample is just one large bump and for the 2 ML and 3 ML sample have increasing frequencies, originate from X-rays reflected from the pentacene layers. These oscillations have not to be mistaken for the Bragg peak visible for the 2 ML and 3 ML sample, which arises because of an intra-layer out-of-plane order of the pentacene molecules and therefore can only be observed for a film thickness starting from 2 ML.

The XRR data of 1 ML were fitted using GenX (Björck & Andersson, 2007), a XRR simulation software that employs a model based on Parratt's recursive algorithm (Parratt, 1954) combined with Névot and Croce's approach to include the influence of roughness (Névot & Croce, 1980). The fit and fit parameters are shown in Figure 3.8. The fitted film thickness of 20.6 Å is in agreement with the AFM cross section. However, compared to the *c* lattice parameter of the thin film phase of 15.6 Å the obtain monolayer height is slightly larger. This was also observed by Werzer et al. (2009) for pentacene submonolayers. There, a wetting layer is introduced to explain the height difference, which probably consists of flat lying molecules as it is observed for pentacene deposited on pure Si (Meyer zu Heringdorf, 2008). However, this is not the focus of this work.

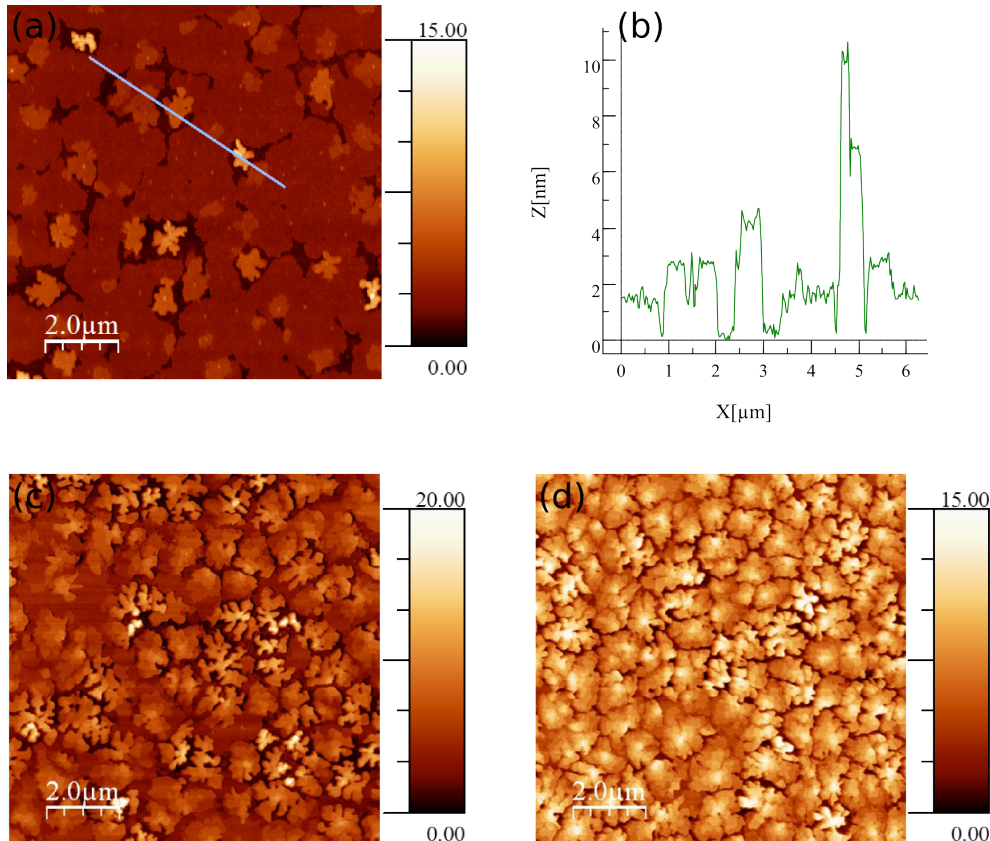


Figure 3.6.: (a) AFM micrograph of nominal 1 ML pentacene (height colorbar in nm). The position of the height profile (b) is indicated with a gray line. (c),(d) AFM micrograph of nominal 2 and 3 ML pentacene, respectively.

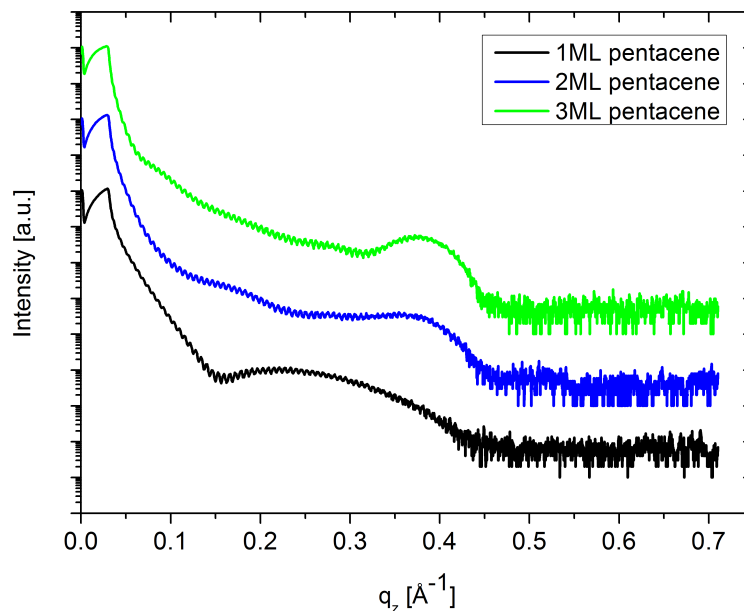


Figure 3.7.: X-ray reflectivity (XRR) of nominal 1 monolayer (1 ML), 2 ML and 3 ML pentacene on SiO_2 before GIXD measurements. The evolution of a three dimensional crystal structure can be observed by the appearance of a Bragg peak at $q_z \approx 0.38 \text{ \AA}^{-1}$ for the 2 and 3 ML sample. XRR curves are vertically shifted for the sake of clarity.

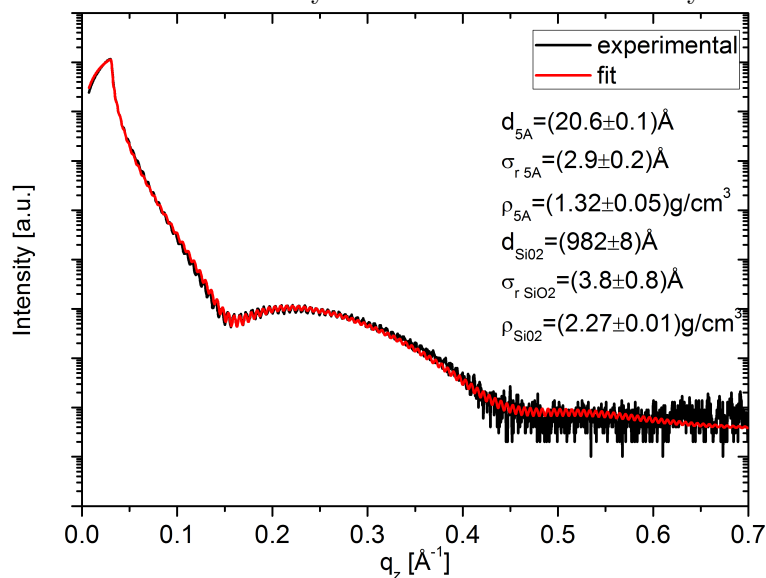


Figure 3.8.: X-ray reflectivity (XRR) of nominal 1 monolayer pentacene (5A) on SiO_2 before GIXD measurements. The solid red curve corresponds to the fit of the experimental data. The fit parameters are listed inside the graph (d = thickness; σ = root-mean-squared roughness; ρ = density).

GIXD experiments and characterization of the in-plane order

Grazing incidence reciprocal space maps (RSM) of 1 ML, 2 ML, and 3 ML samples were measured using our laboratory setup and at the HASYLAB W1 beamline. The RSM are depicted in Figure 3.10.

For the laboratory measurement a step size of $\Delta 2\theta_i = 0.05^\circ$ was chosen, using an integration time of 360 s per step. To reduce measurement time only small sections within the range of the expected Bragg rods were scanned ($18^\circ - 20^\circ$ in $2\theta_i$ for the first, $22.5^\circ - 24.5^\circ$ for the second, and $27^\circ - 29^\circ$ for the third rod). The incidence angle α_i was set, as for the 50 nm film, to the critical angle of total external reflection $\alpha_c = 0.17^\circ$. To illustrate the influence of the incidence angle on the surface sensitivity and enhancement of the scattered evanescent wave, the first Bragg rod was scanned at different incidence angles, as shown in Figure 3.9 for 1 and 2 ML. For the 1 ML sample the peak of the Bragg rod is only visible if α_i is equal to the critical angle $\alpha_c = 0.17^\circ$. However, it must be admitted that degradation due to beam damage also had an influence on this measurement, as is pointed out in Section 3.1.5 in more detail. But also for the 2 ML sample (Figure 3.9(b)) it is evident that at $\alpha_i = 0.17^\circ$ the peak-to-background ratio is the best. Higher incidence angles only increase the penetration depth of the evanescent wave, i.e., increase the unwanted scattering from the substrate. Due to this high dependence on the incidence angle a proper alignment of the sample is crucial before performing GIXD measurements.

At the HASYLAB W1 beamline the RSMs were scanned over a $2\theta_i$ range of $13^\circ - 22.5^\circ$, using a step size of $\Delta 2\theta_i = 0.033^\circ$, an integration time of 5 s per step, and an incidence angle of $\alpha_i = 0.15^\circ$.

The rod-like shape of the diffraction features in the RSMs (Figure 3.10) originates from the absence of a periodicity perpendicular to the substrate surface that is characteristic for monolayer films. As expected, for the 2 and 3 ML samples an evolution of a 3 dimensional structure is observed by the emergence of Bragg peaks at out-of-plane q_z values at the 02 and 12 Bragg rods. The Bragg rod profiles are analyzed in more detail in the next section.

In the RSM of the 1 ML sample measured with our laboratory setup hardly any rod is visible. Only at the Yoneda reflection (Yoneda, 1963), which is the horizontal line at approximately $q_z = 0.025 \text{ \AA}^{-1}$ that occurs due to diffuse scattering from the surface at the critical angle of total external reflection, increased intensity is visible. However, integrated linescans clearly show diffraction peaks, as can be seen in Figure 3.11. There, background subtracted integral intensity diffraction profiles (integrated over a q_z range from 0 \AA^{-1} to 0.25 \AA^{-1}) for 1 ML, 2 ML, and 3 ML samples are shown for the lab and in Figure 3.12 for the synchrotron measurement. Because the indexation of the first three Bragg rods (11, 02, and 12) is known from previous work (Fritz et al., 2004) the two dimensional unit cell parameters can be calculated from the q_p positions of the rods. They were obtained by fitting the integrated diffraction profiles with Lorentzians. Fit parameters are listed in Table 3.4. The calculation of the 2 dimensional lattice parameters was deduced from the square of the 2D scattering

3. EXPERIMENTAL SETUP PERFORMANCE - RESULTS AND DETAILS

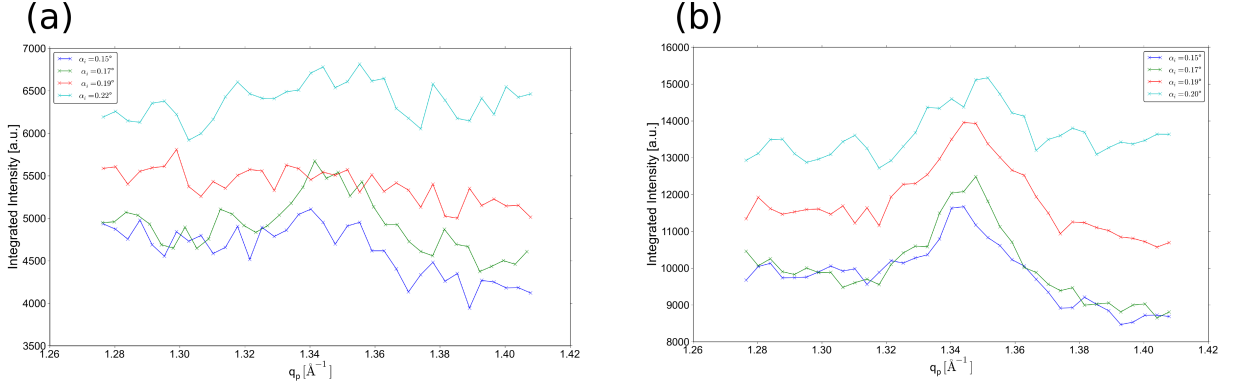


Figure 3.9.: Integrated diffraction intensities (from $q_z = 0 \text{ \AA}^{-1}$ to $q_z = 0.25 \text{ \AA}^{-1}$) of nominal 1 ML (a) and 2 ML (b) pentacene for different incidence angles α_i .

vector q_{hk}

$$q_{hk}^2 = (ha^*)^2 + (kb^*)^2 + hka^*b^* \cos(\gamma^*) \quad (3.5)$$

With the known indexation of three q_{hk} peaks, three equations for the 2 dimensional reciprocal lattice parameters a^* , b^* , and γ^* can be derived out of Eq. (3.5):

$$b^{*2} = \frac{q_{02}^2}{4} \quad (3.6)$$

$$a^{*2} = \frac{q_{02}^2}{2} - q_{12}^2 + 2q_{11}^2 \quad (3.7)$$

$$\cos(\gamma^*) = \frac{4q_{11}^2 - 4a^{*2} - q_{02}^2}{4q_{02}a^*} \quad (3.8)$$

or further transformed into direct space

$$\cos(\gamma) = -\cos(\gamma^*) \quad (3.9)$$

$$a = \frac{2\pi}{a^* \sin(\gamma)} \quad (3.10)$$

$$b = \frac{2\pi}{b^* \sin(\gamma)} \quad (3.11)$$

The resulting parameters are summarized in Table 3.5. Errors were calculated out of the errors of the q_{hk} fit parameters using error propagation. Laboratory and synchrotron analysis are within the errors in perfect agreement with each other. Also previous studies of pentacene mono- and multilayers carried out by Fritz et al. (2004) and Ruiz et al. (2004a), both using synchrotron radiation, report same parameters.

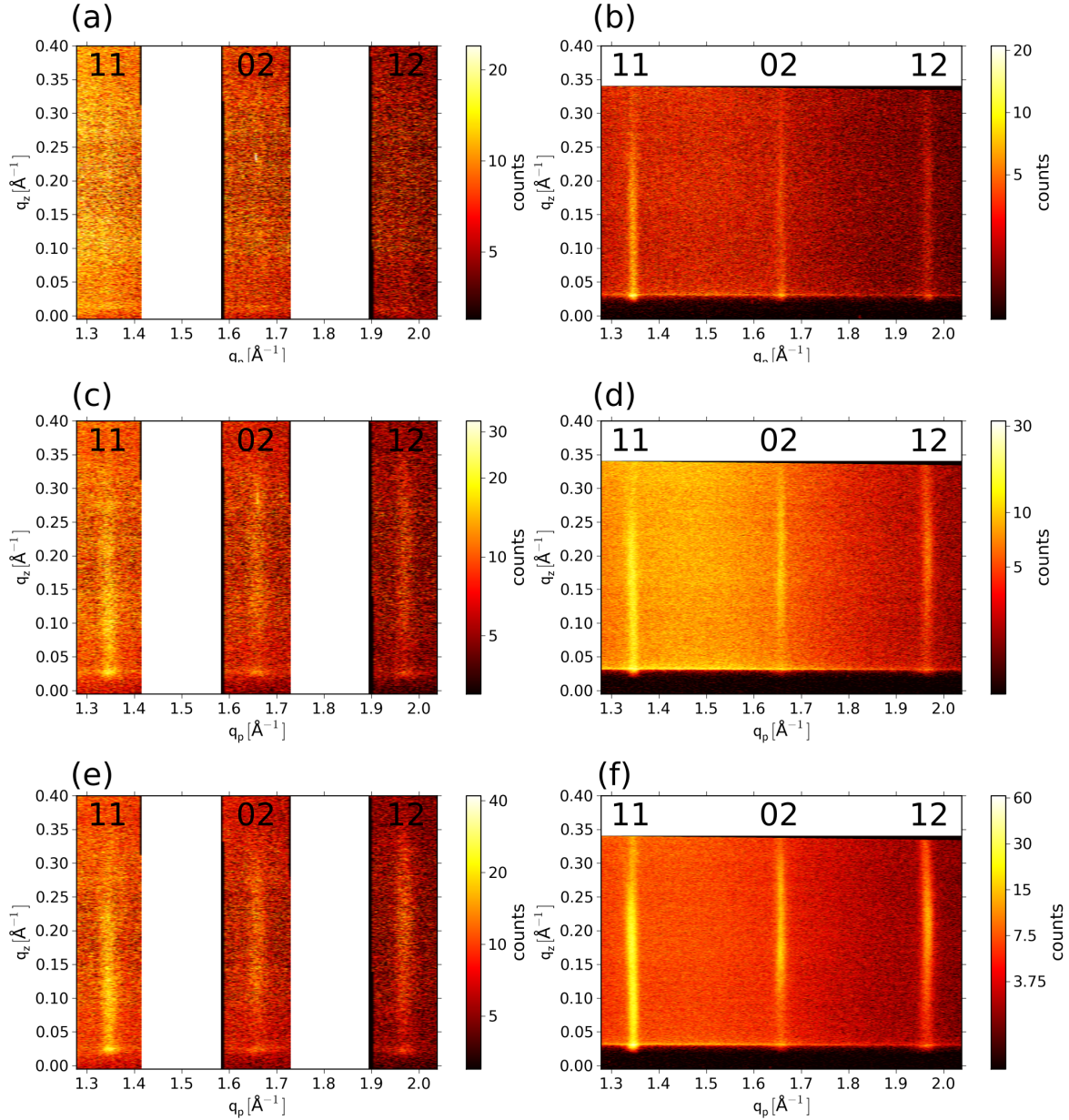


Figure 3.10.: Grazing incidence reciprocal space maps of nominal 1 ML ((a),(b)), 2 ML ((c),(d)), and 3 ML ((e),(f)) pentacene on SiO₂. (a), (c), and (d) were measured with the laboratory setup; (b), (e), and (f) at the HASYLAB W1 beamline. The Indexation of the Bragg rods is given.

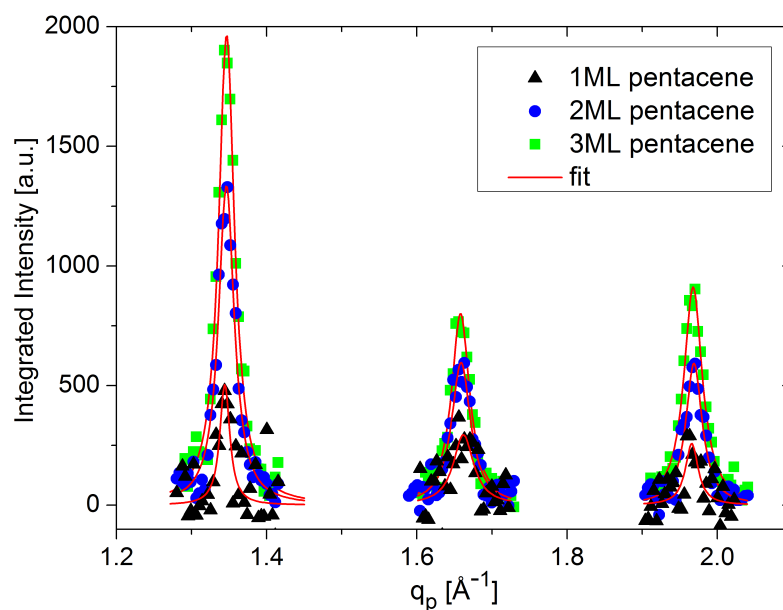


Figure 3.11.: Background subtracted diffraction intensities measured with the laboratory setup of 1 ML, 2 ML, and 3 ML pentacene integrated along the q_z direction (from 0 \AA^{-1} to 0.25 \AA^{-1}) and plotted as a function of the in-plane scattering vector q_p (triangles, circles, and squares). The first 3 Bragg rods are shown and fitted with Lorentzians (full lines).

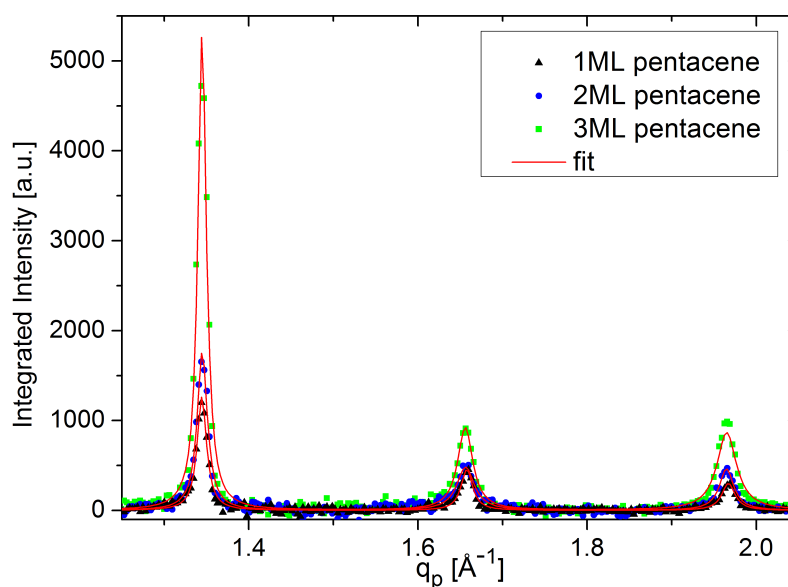


Figure 3.12.: Background subtracted diffraction intensities measured at the HASYLAB W1 beamline of 1 ML, 2 ML, and 3 ML pentacene integrated along the q_z direction (from 0 \AA^{-1} to 0.1 \AA^{-1}) and plotted as a function of the in-plane scattering vector q_p (triangles, circles, and squares). The first 3 Bragg rods are shown and fitted with Lorentzians (full lines).

Table 3.4.: Fit parameter of Lorentzian fits of the integrated Bragg rods for laboratory and synchrotron measurements (see Figure 3.11 and 3.12).

		$q_p / \text{\AA}^{-1}$	FWHM / \AA^{-1}	height	area
laboratory setup					
	rod 11	1.344 ± 0.002	0.016	506	12.8
1 ML	rod 02	1.662 ± 0.005	0.033	295	15.2
	rod 12	1.966 ± 0.005	0.022	257	8.4
	rod 11	1.3464 ± 0.0004	0.026	1337	53.6
2 ML	rod 02	1.6589 ± 0.0007	0.030	596	28.8
	rod 12	1.9689 ± 0.0007	0.027	593	24.8
	rod 11	1.3466 ± 0.0004	0.026	1967	79.4
3 ML	rod 02	1.6582 ± 0.0005	0.030	800	37.1
	rod 12	1.9678 ± 0.0005	0.030	911	43
HASYLAB W1					
	rod 11	1.3445 ± 0.0002	0.013	1265	26.7
1 ML	rod 02	1.6577 ± 0.0004	0.016	457	11.7
	rod 12	1.9670 ± 0.0005	0.19	303	9.0
	rod 11	1.3450 ± 0.0002	0.014	1771	40.3
2 ML	rod 02	1.6562 ± 0.0007	0.025	483	19.0
	rod 12	1.9648 ± 0.0004	0.021	466	15.0
	rod 11	1.3449 ± 0.0001	0.012	5333	101.0
3 ML	rod 02	1.6559 ± 0.0006	0.021	921	31.25
	rod 12	1.9650 ± 0.0005	0.028	867	38.1

Table 3.5.: Two dimensional unit cell parameters of one monolayer (1 ML), 2 ML, and 3 ML pentacene calculated from the fitted diffraction peak positions of Figure 3.11 and 3.12. The parameters obtained from our laboratory and synchrotron data are compared to parameters from previous studies of a pentacene monolayer (Fritz et al., 2004), sub monolayer (SML) and multilayer (MML) (Ruiz et al., 2004a) (both from synchrotron measurements).

	a / Å	b / Å	$\gamma/^\circ$
laboratory setup			
1 ML	5.91 ± 0.06	7.56 ± 0.03	89.6 ± 0.5
2 ML	5.92 ± 0.02	7.58 ± 0.01	90.0 ± 0.2
3 ML	5.91 ± 0.01	7.58 ± 0.01	89.9 ± 0.2
HASYLAB W1			
1 ML	5.936 ± 0.01	7.581 ± 0.005	90.0 ± 0.1
2 ML	5.913 ± 0.01	7.587 ± 0.005	89.8 ± 0.1
3 ML	5.918 ± 0.01	7.589 ± 0.005	89.9 ± 0.1
1 ML (Fritz et al., 2004)	5.916	7.588	89.95
SML (Ruiz et al., 2004a)	5.90	7.62	90.0 ± 0.2
MML (Ruiz et al., 2004a)	5.91	7.58	90.0 ± 0.2

3.1.4. Bragg rod analysis

The intensity distributions along Bragg rods (along q_z) of a monolayer give informations about the orientations of the molecules within the layer because the maximum in q_z direction is determined by the molecular form factor (Als-Nielsen et al., 1994; Kjaer, 1994). The molecular form factor (i.e., the Fourier transformed squared of the electron distribution) of a rod like molecule is a flat disc perpendicular to the molecular axis. Assuming upright standing molecules, i.e., molecules perpendicular to the surface, the molecular Form factor intercepts the Bragg rods at the horizon. Thus, the diffraction intensity along any Bragg rod will have its maximum at the sample horizon (Yoneda). If the molecules are tilted the maxima occur at different positions for each Bragg rod depending on the molecular tilt and tilt direction.

Bragg rod profiles of the 1 ML, 2 ML, 3 ML, and 50 nm pentacene samples are compared in Figure 3.13. Concerning the 1 ML sample it can clearly be seen that for all 3 Bragg rods the intensity maxima are at the Yoneda peak ($q_z = 0.025 \text{ \AA}^{-1}$). It must be admitted that the quality of the laboratory measurement is very poor. Nevertheless, regarding the arguments given above a qualitative conclusion can be drawn that the molecules in the 1 ML sample are upright standing. Here, more detailed synchrotron measurements are necessary to obtain more sophisticated data for quantitative analysis. Mannsfeld et al. (2009) performed a precise structural study of pentacene monolayers on SiO_2 using synchrotron radiation. There, a refinement of the Bragg rod profiles shows fully upright standing molecules in a herringbone packing with a herringbone angle of 52.7° . Furthermore, the result of standing molecules is in agreement with the obtained layer thickness of AFM and XRR measurements.

For the 2 ML and 3 ML samples the evolutions of a 3 dimensional structure can be observed, compatible to XRR measurements (Figure 3.7). The increased intensities at higher q_z -values in this case are not only due to tilted molecules but because of the formation of a 3 dimensional structure. This can be seen when comparing the Bragg rod profiles of the 2 ML and 3 ML films to the 50 nm pentacene film. Especially for the 12 rod of the 3 ML sample a pronounced peak can be seen at a q_z position corresponding to the 1-21, -120 double peak of the pentacene thin-film phase.

3.1.5. Degradation under the X-ray beam

Beam damage plays a non negligible role in the characterization of organic materials using X-ray diffraction. Especially the highly intense X-ray beams of modern synchrotrons can cause damage to soft matter materials during beam exposure. The reason for degradation due to beam damage is on the one hand the formations of photoelectrons induced by the incoming X-ray beam (Prince & of Crystallography., 2004). This photoelectrons favor the formation of free radicals that can damage the molecular structure. Another problem is the formation of highly reactive ozone and NO_x near the sample leading to oxidative degradation. For that reason normally synchrotron measurements are performed under inert conditions using a constant He flux or vacuum inside an X-ray transparent sample chamber. In this work all synchrotron

measurements were carried out under He atmosphere, but all laboratory measurements were performed under ambient conditions. For pentacene thin films under He-atmosphere recent study show that they are very stable to radiation damage after long synchrotron beam exposures (Neuhold et al., 2011).

To determine a possible degradation after GIXD experiments in the laboratory under ambient conditions, the same XRR measurements as for the pre-characterization were performed for the 1 ML, 2 ML and 3 ML sample and compared to the initial ones (Figure 3.14). There, a decrease in the Bragg peak intensity can be seen for the 2 ML and 3 ML sample indicating a degradation of the crystallinity. The XRR of the 1 ML sample shows a tremendous change after the long X-ray irradiation of the GIXD measurements. These data were fitted by GenX as before. Comparing Figure 3.8 and Figure 3.15 and their fit parameters an increased pentacene thickness and roughness, and a decreased density is observed after X-ray irradiation. An increase in thickness was also observed for films of the polymer polystyrene after X-ray irradiation (Richter et al., 2006; Bhatta et al., 2009). There, this increase is related to a radiation induced cross-linking of the polymer, however it is more likely that bonds brake up and thus the van der Waals volume of these new formed fragments is bigger than of the original polymer. For our present case of the small molecule pentacene highly reactive ozone is formed near the sample surface that breaks up bonds. The resulting oxidized fragments are separated more spatially because they are no longer covalent bond to each other resulting in an increased film thickness and decreased density. Furthermore, the crystalline structure of the 1 ML sample was totally destroyed. It was not possible to measure any diffraction features at the HASYLAB W1 beamline for the 1 ML sample that was measured beforehand in the laboratory and therefore irradiated for a long time under ambient conditions. The reference RSM of 1 ML pentacene Figure 3.10(b) was measured on an unused identical 1 ML sample.

For the 50 nm pentacene thin-film integrated linescans of same rods were compared after long irradiation times and no degradation was observed (not shown here; integration similar to Figure 3.4). This confirms the theory of degradation due to ozone formed near the sample surface, thus, just degrading the first layer, which is not so crucial for the crystallinity of a thick layer. Further, it is in agreement with Neuhold et al. (2011) who reports no degradation of pentacene considering photoelectrons (oxidation was excluded due to measurements under He atmosphere).

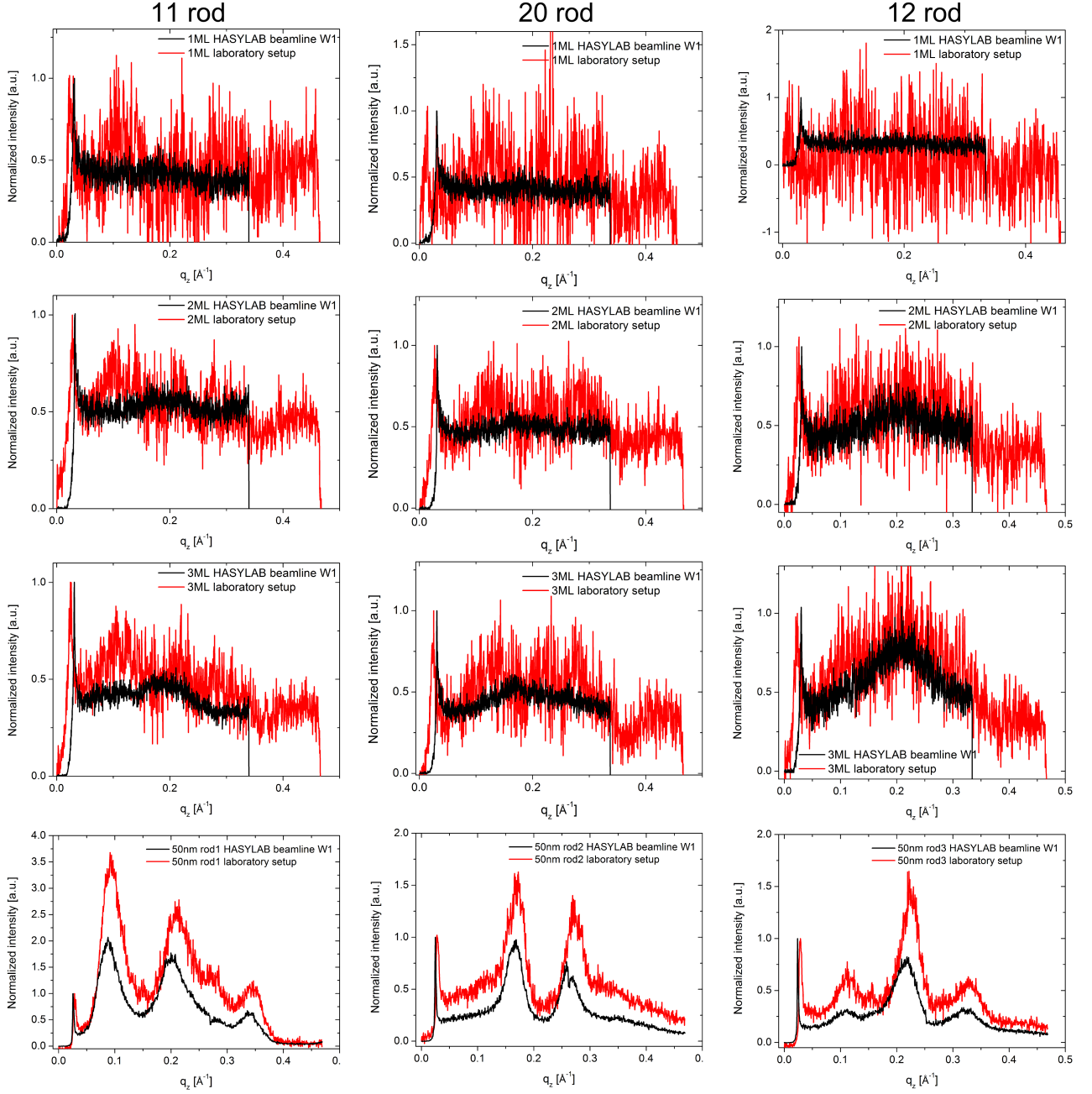


Figure 3.13.: Bragg rod profiles of the first three Bragg rods integrated along q_p (from 1.317 \AA^{-1} to 1.38 \AA^{-1} for the first, from 1.62 \AA^{-1} to 1.70 \AA^{-1} for the second, and from 1.94 \AA^{-1} to 1.99 \AA^{-1} for the third rod) for 1 monolayer (1 ML), 2 ML, 3 ML and 50 nm thin pentacene film. Lab measurements (red lines) are compared to synchrotron measurements (black lines); the intensities at the Yoneda peak are scaled to each other. The evolution of a 3 dimensional structure is clearly observed in the 2 ML and 3 ML samples by the emergence of Bragg peaks at out-of-plane q_z values corresponding to them of the thin film phase.

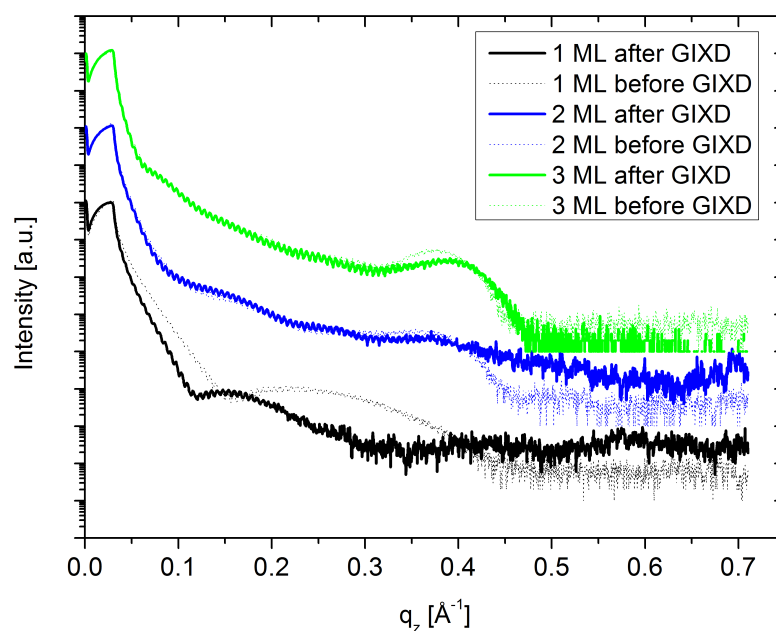


Figure 3.14.: X-ray reflectivity (XRR) of nominal 1 monolayer (1 ML), 2 ML and 3 ML pentacene on SiO_2 before (dashed lines) and after (solid lines) GIXD measurements. Degradation after X-ray irradiation is clearly visible. XRR curves are vertically shifted for the sake of clarity.

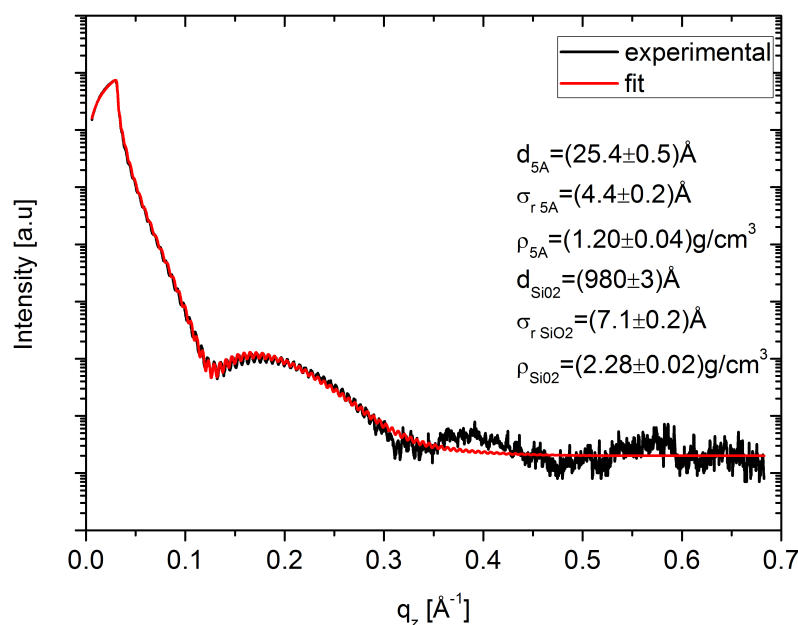


Figure 3.15.: X-ray reflectivity (XRR) of nominal 1 monolayer pentacene on SiO_2 after GIXD measurements. The solid red curve corresponds to the fit of the experimental data. The fit parameters are listed inside the graph (d = thickness; σ = root-mean-squared roughness; ρ = density).

3.2. Microstructure characterization of a quinquethiophene based self-assembled monolayer

Self-assembled monolayers (SAMs) are promising materials in the field of organic electronics, since charge transport in organic field-effect transistors is determined by the first monolayer of the organic semiconducting material and the properties at the interface (Dinelli et al., 2004; Mottaghi & Horowitz, 2006) and self assembly allows to obtain highly reproducible films. Quinquethiophene based SAMs used in organic field-effect transistors are reported to have same properties as bulk ones (Mathijssen et al., 2009) and are successfully used in integrated organic electronics (Smits et al., 2008). Furthermore, their processing is solution based which drastically reduces fabrication costs and makes this materials a promising candidate for low cost flexible devices. In the following a microstructure study on quinquethiophene based SAMs using a combination of X-ray reflectivity (XRR) measurements and grazing incidence in-plane diffraction (GIXD) fully performed with standard laboratory equipment is presented. Especially for GIXD this is a novelty, as normally GIXD experiments on organic self-assembled monolayers were carried out up to now at synchrotron radiation facilities of high brilliance. It is once more emphasized that GIXD is perfectly suited to characterize the in-plane order of crystalline monolayers because of its high surface sensitivity to lattice planes perpendicular to the sample surface. In addition to GIXD, XRR reveals the out-of-plane layer structure like layer thickness, root-mean-squared surface roughness, and layer electron density.

3.2.1. Fabrication and layer formation

The basic steps of the solution based processing of a SAM are shown in Figure 3.16 (taken from Flesch (2010)). First the molecules have to be dissolved in a solvent, then the beforehand cleaned and treated (to make it reactive) substrate is submerged into the solution. As a next step just time is needed until a fully covered layer is formed. The last step is taking out the substrate from the solution and rinsing it.

In this work molecules that comprise a semiconducting quinquethiophene backbone, that is end-capped with an ethyl group for stability, and have a monochlorosilane anchoring group attached to the backbone via an undecane alkyl spacer (dielectric) are used (see Figure 3.17). This design was chosen to combine the semiconducting and dielectric parts necessary for an organic field effect transistor in one molecule.

The chlorine of the monochlorosilane anchoring group reacts with the remaining water of the solvent (toluene) and forms an OH-group and HCl. The OH-group can bind to a hydroxylated silicon oxide substrate (Si-OH). This is schematically illustrated in Figure 3.17. It is reported that the substrate has to stay at least 24 hours in the solution to achieve the formation of a closed monolayer (Flesch, 2010).

A more detailed description of the layer formation and molecular design can be found in the supplementary informations of Smits et al. (2008) and in Flesch (2010).

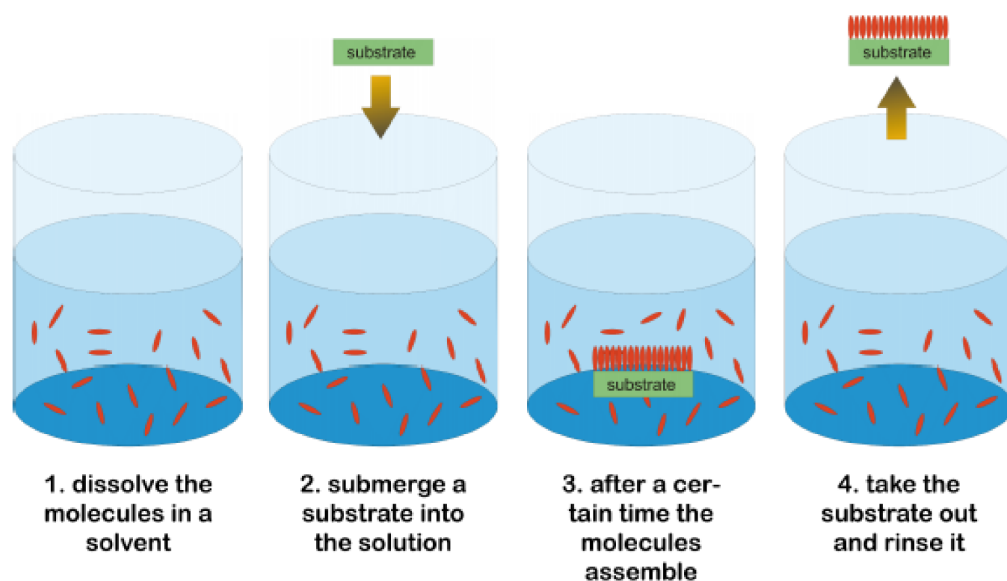


Figure 3.16.: Schematic diagram of the solution processing of a self assembled monolayer (picture take from Flesch (2010)).

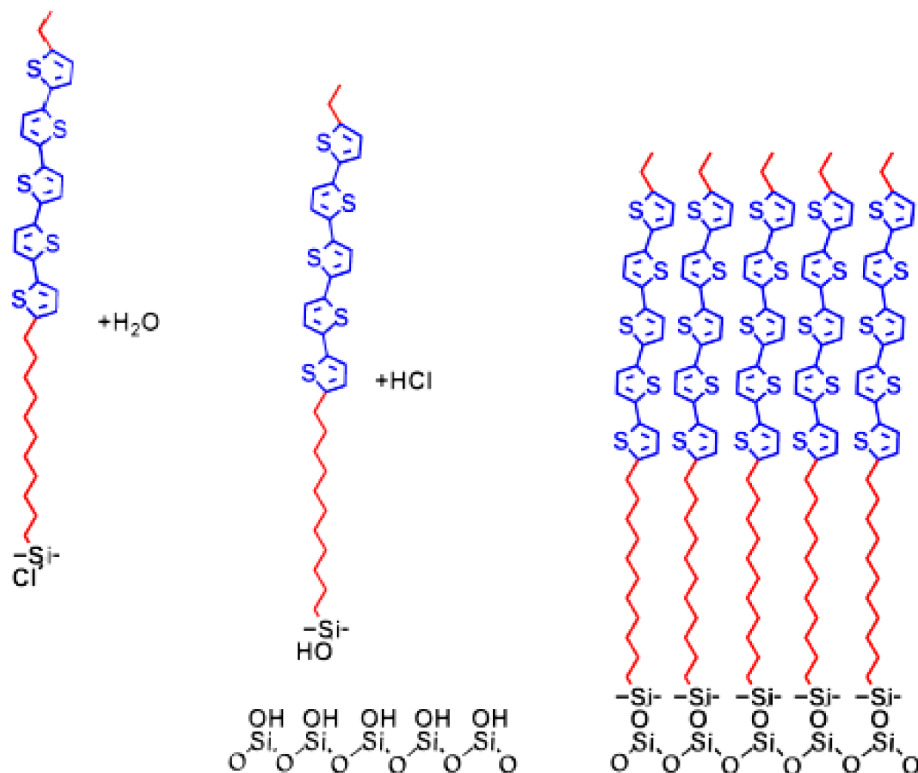


Figure 3.17.: Schematic diagram of the layer formation and the assembly of the molecules on the SiO_2 substrate (picture take from Flesch (2010)).

3.2.2. XRR investigations

Two different samples of quinquethiophene based SAMs were investigated, which are named sample NA1 and sample R95 in the following.

The layer composition of the SAMs was first probed using XRR measurements to obtain the electron density profile (or density), layer thickness, and root-mean-squared roughness. XRR measurements were carried out on a Panalytical Empyrean $\theta/2\theta$ diffractometer, using a step size of $\Delta 2\theta = 0.005^\circ$ and an integration time of 2 seconds per step. In Figure 3.18 the XRR curve of the SAM sample NA1 is depicted as reflected X-ray intensity as a function of momentum transfer q_z . There, the high frequency oscillations are due to interferences of X-rays reflected from the 200nm thick SiO_2 substrate and the one visible oscillation with lower frequency originates from interferences of X-rays reflected from the SAM. For fitting the XRR data with GenX (Björck & Andersson, 2007) a two layer model with two different densities was necessary, where one layer represents the alkyl spacer group and the other the thiophene backbone.

The fit parameters obtained for the alkyl spacer layer were a density of $\rho = 1.0 \pm 0.02 \text{ g/cm}^3$, a thickness of $d = 5.9 \pm 0.2 \text{ \AA}$, and a root-mean-squared roughness of $R_{rms} = 2.5 \pm 0.2 \text{ \AA}$. The higher density layer ($\rho = 1.58 \pm 0.04 \text{ g/cm}^3$) corresponds to the thiophene backbone layer. Its thickness and root-mean-squared roughness was found to be $d = 20.6 \pm 0.4 \text{ \AA}$ and $R_{rms} = 5.3 \pm 0.2 \text{ \AA}$, respectively. The obtained thickness of the quinquethiophene backbone compare well to the calculated value of 21 \AA (Smits et al., 2008), but for the undecane alkyl spacer a larger thickness of 15 \AA is expected. The backbone density compare well with reported densities between $1.07\text{-}1.62 \text{ g/cm}^3$ (Flesch, 2010). For the alkyl spacer layer densities between $0.49\text{-}0.82 \text{ g/cm}^3$ are reported. In this fit a higher density was found which can be explained by the also found lower thickness of the alkyl spacer layer. To summarize, XRR measurement indicates that the out-of-plane order of sample NA1 consists of the alkyl space layer, which thickness is smaller as expected, followed by fully upright standing quinquethiophene backbones.

The XRR curve of sample R95 is shown in Figure 3.19(a). There, it can clearly be seen that the curve looks different compared to sample NA1. The oscillations originating from interferences of X-rays reflected from the SAM have higher frequencies than for sample NA1. This is an indication for a larger layer thickness. 3.19(b) shows possible misalignments of the molecules during layer formations that can lead to an increased layer thickness. Also not optimized growth conditions (i.e., purity of the active molecules, concentration, growth duration) can lead to precipitations and 3D agglomerations. XRR fitting is always linked to the refinement of a proper model, however in this case of misaligned molecules it is difficult to find an appropriate one. Therefore, XRR data of sample R95 were not fitted. Nevertheless, the thickness can be estimated out of the period (Δ) of the fringes in q -space using $d = 2\pi/\Delta$ (Als-Nielsen & McMorrow, 2001). This leads to an estimated thickness of about 100 \AA .

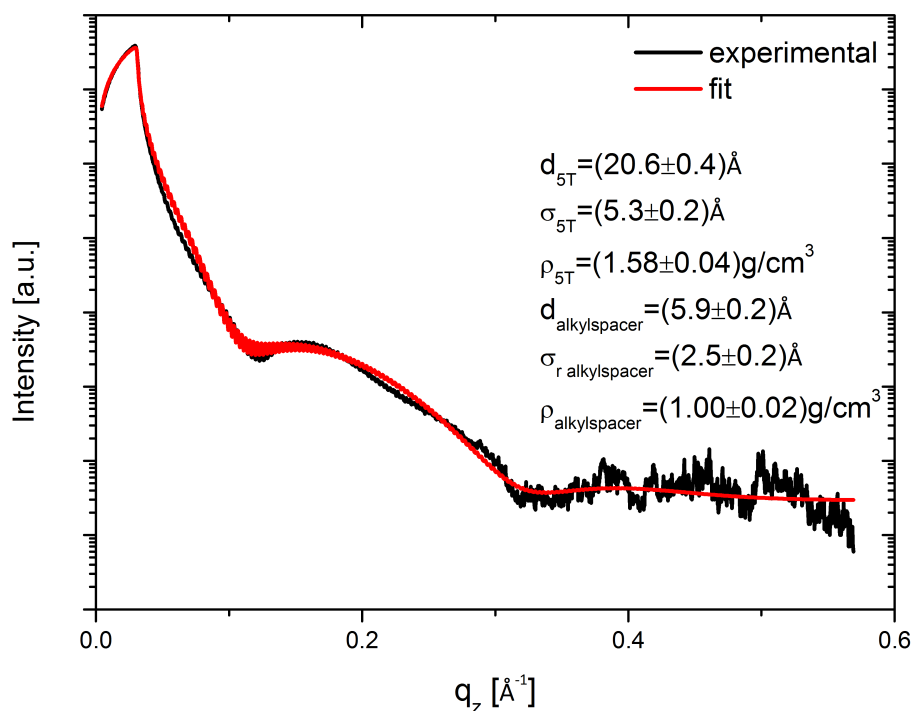


Figure 3.18.: X-ray reflectivity (XRR) of quinquethiophene (5T) based SAM on SiO₂ (sample NA1). The solid red curve corresponds to the fit of the experimental data. The fit parameters are listed inside the graph (d = thickness; σ = root-mean-squared roughness; ρ = density).

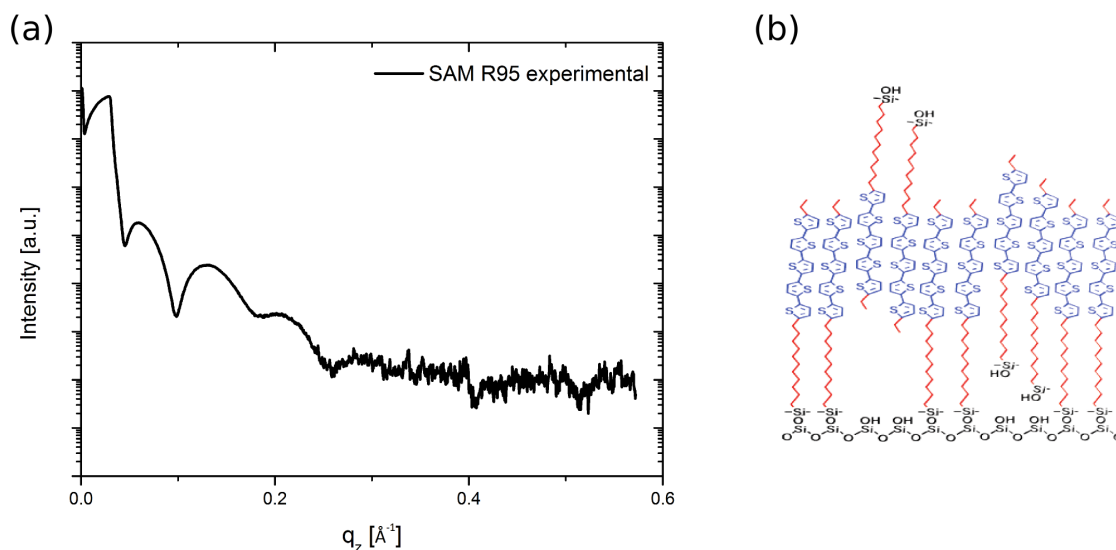


Figure 3.19.: (a) X-ray reflectivity (XRR) of quinquethiophene based SAM on SiO₂ (sample R95). (b) Possible misalignments of molecules during layer formation (picture take from Flesch (2010)).

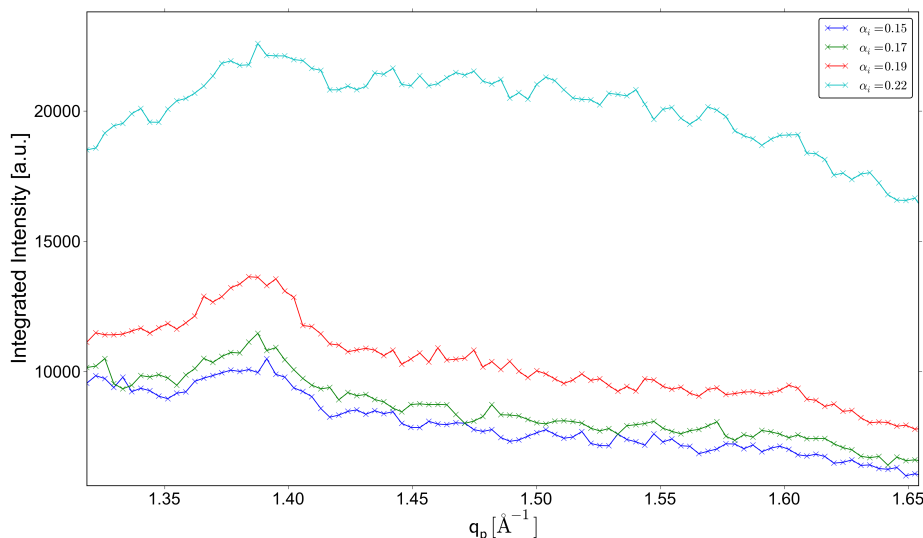


Figure 3.20.: Integrated diffraction intensities (from $q_z = 0 \text{ \AA}^{-1}$ to $q_z = 0.4 \text{ \AA}^{-1}$) of a quinquethiophene based SAM (sample R95) measured at different different incidence angles α_i .

3.2.3. GIXD investigations

The in-plane order of the SAMs was determined by GIXD measurements carried out with our laboratory setup. As measurement parameters a step size of $\Delta 2\theta_i = 0.05^\circ$ and an integration time of 360 seconds per step were chosen. An incidence angle of $\alpha_i = 0.18^\circ$ was used which corresponds to the critical angle of total external reflection of the SAM molecules for Cu- K_α radiation ($\lambda = 1.54178 \text{ \AA}$). It was calculated using Eq.(3.1) and an electron density of $\rho = 0.46 \text{ electrons/\AA}^3$ (Flesch, 2010). Furthermore, the diffracted intensity as a function of the incidence angle was investigated. This can be seen in Figure 3.20 where integrated linescans of the first two Bragg rods measured at different incidence angles are shown. At a too high incidence angle of $\alpha_i = 0.22^\circ$ the X-ray penetrates that much into the sample that the amorphous signal of the SiO_2 substrate is visible (large peak with maximum at about $q_p = 1.5 \text{ \AA}^{-1}$). Only for an incidence angle near the critical angle $\alpha_c = 0.18^\circ$ the second Bragg rod at $q_z = 1.6 \text{ \AA}^{-1}$ can be observed.

The GIXD reciprocal space maps of sample NA1 and sample R95 are depicted in Figure 3.21(a) and Figure 3.22(a), respectively. Remarkable are the rod like shapes of the diffraction features. These so called Bragg rods are characteristically for monolayers, as they originate from the absence of periodicity perpendicular to the sample surface. Moreover, the onsets of the Bragg rods are located directly at the Yoneda reflection (Yoneda, 1963) which is the horizontal line at approximately $q_z = 0.025 \text{ \AA}^{-1}$ that occurs due to diffuse scattering from the surface at the critical angle of total external reflection. Having the onset directly at the Yoneda reflection is a strong indication for fully upright standing molecules (Kjaer, 1994). This is in perfect agreement with the XRR results. A recent study shows that for the same quinquethiophene

Table 3.6.: Fit parameter of Lorentzian fits of the integrated Bragg rods for laboratory measurements (see Figure 3.21(b) and 3.22(b)).

		$q_p / \text{\AA}^{-1}$	FWHM / \AA^{-1}	height	area
laboratory setup					
sample NA1	rod 11	1.4013 ± 0.0007	0.024	970	36.7
	rod 02	1.6154 ± 0.0006	0.028	490	21.8
	rod 12	1.981 ± 0.003	0.042	242	16.2
sample R95	rod 11	1.3888 ± 0.0006	0.031	2202	110
	rod 02	1.6042 ± 0.001	0.019	773	24.1
	rod 12	1.9612 ± 0.002	0.032	501	25.6

SAM system a phase transition from upright standing to tilted molecules is observed upon annealing resulting in an increased intensity of the Bragg rod above the Yoneda horizon (Flesch et al., 2011).

In the RSM of sample NA1 also Si 111 reflections are visible due the fact that the sample was cut and small Si crystallites stucked to the surface.

From the position in q_p of the Bragg rods and by indexing the first three Bragg rods with 11, 02, and 12 the two dimensional unit cell parameters could be calculated. The Bragg rods' q_p positions were obtained by fitting the background subtracted integrated intensities (integrated along q_z from 0\AA^{-1} to 0.15\AA^{-1}) with Lorentzians as it is shown in Figure 3.21(b) and Figure 3.22(b) for sample NA1 and R95, respectively. The fit parameter are listed in Table 3.6. Out of them the unit cell parameters were calculated using Eq.(3.6)-(3.9). The resulting parameters are summarized in Table 3.7 and show perfect agreement with previous studies of quinquethiophene SAMs (Mathijssen et al., 2009; Smits et al., 2008; Flesch, 2010), all performed using synchrotron radiation facilities. The obtained unit cell parameters compare well to unit-cells of herringbone packed molecules observed in oligothiophenes (Fichou, 1999). Thus, the high crystalline in-plane order is due to a herringbone packing of the quinquethiophene backbone, whereas the undecane alkyl spacers play a minor role for crystallization and are expected to be amorphous. To obtain the herringbone angle density functional theory calculations could be employed using the calculated lattice parameters as inputs. This was done in the work of Flesch et al. (2011) reporting a herringbone angle of 63° .

3.2. MICROSTRUCTURE CHARACTERIZATION OF A QUINQUETHIOPHENE BASED SELF-ASSEMBLED MONOLAYER

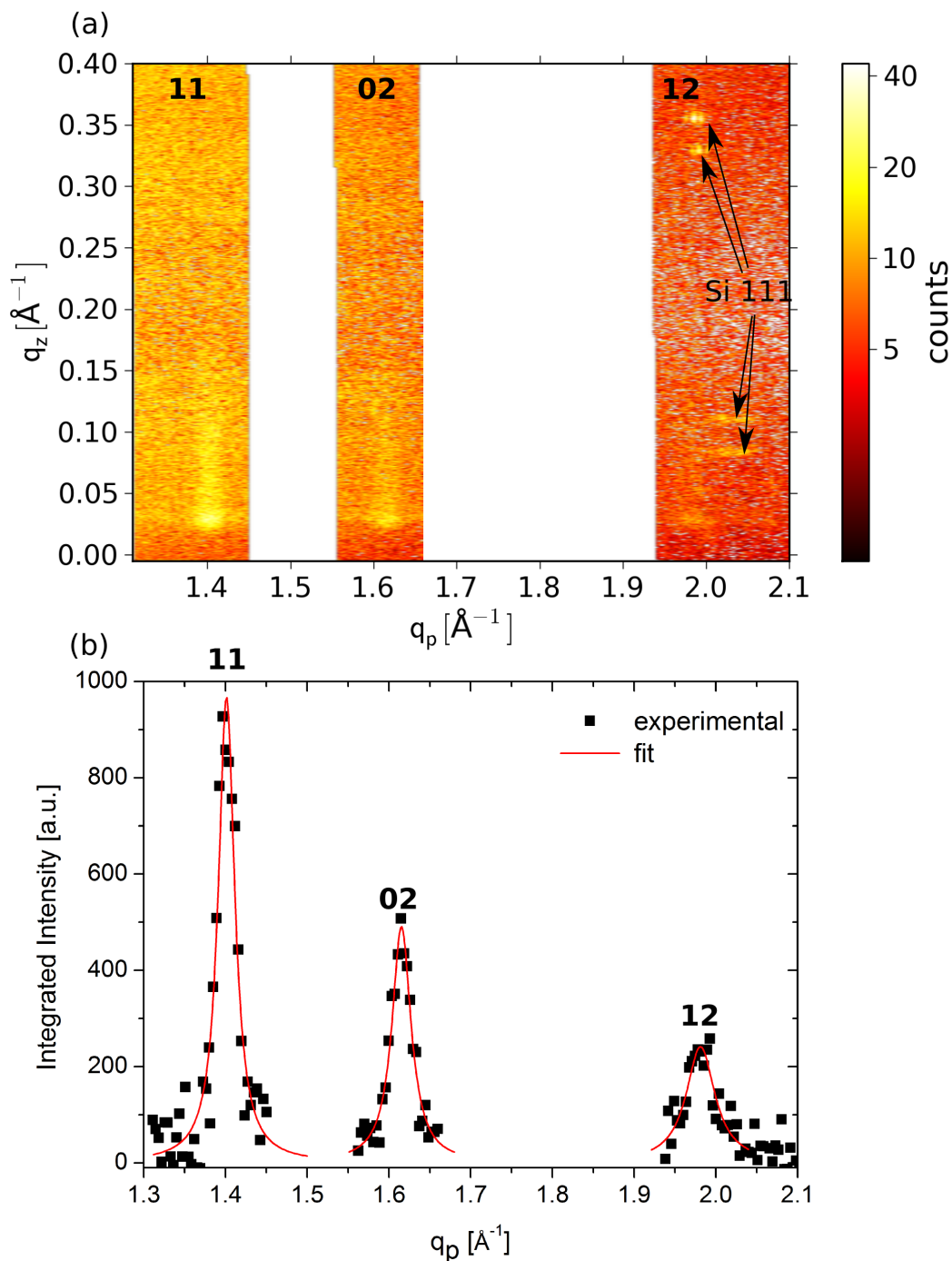


Figure 3.21.: (a) Grazing incidence reciprocal space map of a quinquethiophene based SAM on SiO_2 (sample NA1) showing the first three Bragg rods (11, 02, 12). (b) Background subtracted diffraction intensities integrated along the q_z direction (from 0 \AA^{-1} to 0.15 \AA^{-1}) and plotted as a function of the in-plane scattering vector q_p (squares). The peaks are fitted with Lorentzians (full lines).

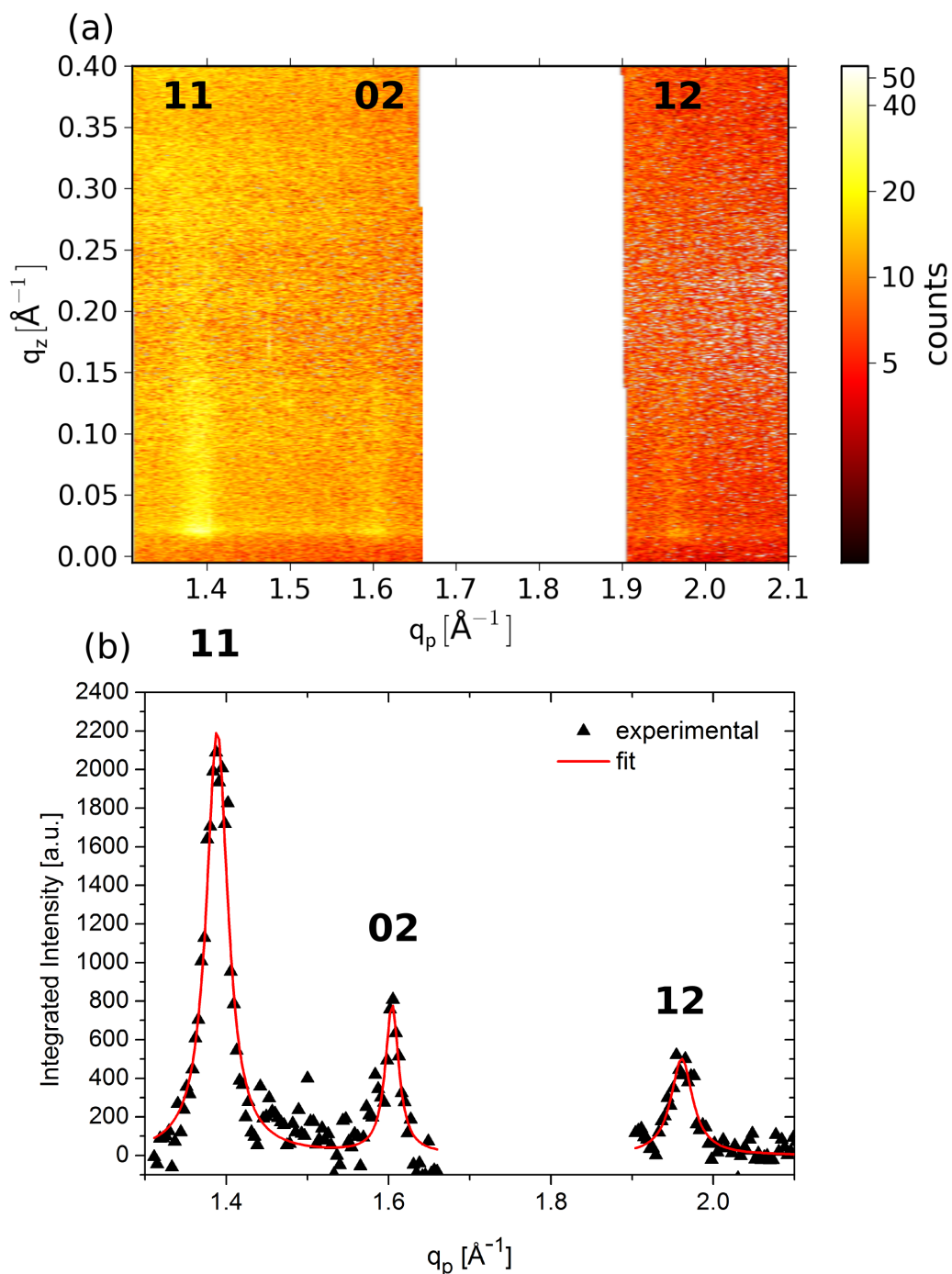


Figure 3.22.: (a) Grazing incidence reciprocal space map of a quinquethiophene based SAM on SiO_2 (sample R95) showing the first three Bragg rods (11, 02, 12). (b) Background subtracted diffraction intensities integrated along the q_z direction (from 0 \AA^{-1} to 0.15 \AA^{-1}) and plotted as a function of the in-plane scattering vector q_p (squares). The peaks are fitted with Lorentzians (full lines).

3.2. MICROSTRUCTURE CHARACTERIZATION OF A QUINQUETHIOPHENE BASED SELF-ASSEMBLED MONOLAYER

Table 3.7.: Two dimensional unit cell parameters of quinquethiophene (5T) based SAMs calculated from the fitted diffraction peak positions of Figure 3.21(b) and 3.22(b). The parameters obtained from our laboratory data are compared to parameters from previous studies all performed using synchrotron light sources (Mathijssen et al., 2009; Smits et al., 2008; Flesch, 2010).

	a / Å	b / Å	γ /°
laboratory setup			
sample NA1	5.50 ± 0.03	7.78 ± 0.02	90.1 ± 0.4
sample R95	5.51 ± 0.02	7.83 ± 0.02	89.6 ± 0.4
5T-SAM (Flesch, 2010)	5.61 ± 0.2	7.85 ± 0.2	90.0 ± 2.0
5T-SAM (Mathijssen et al., 2009)	5.49	7.83	90.0
5T-SAM (Smits et al., 2008)	5.49	7.69	90.0

3.2.4. Degradation under the X-ray beam

As already mentioned in Section 3.1.5 organic thin films are very sensitive to X-ray irradiation. To determine possible X-ray induced damages to the SAMs XRR measurements were carried out again after the GIXD experiments. The comparison between XRR before and after GIXD are shown in Figure 3.23. No changes in the XRR signal can be observed. Therefore, any X-ray beam damage can be excluded although all measurements were carried out under ambient conditions. This is in agreement with the observations in the work of Flesch (2010) concerning the same kind of SAMs at room temperature. However, there it is reported that the sample are very sensitive to annealing combined with X-ray irradiation. A steadily degradation of the SAMs in the X-ray beam was found at increased temperatures.

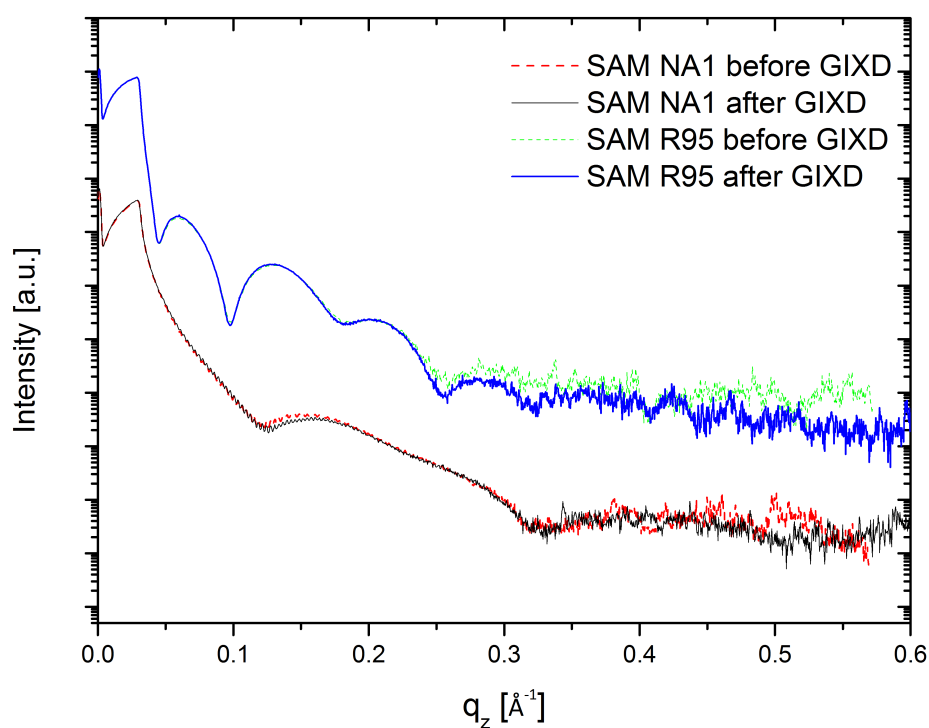


Figure 3.23.: X-ray reflectivity (XRR) of of both quinquethiophene based SAM samples before (dashed lines) and after (solid lines) GIXD measurements. No degradation after X-ray irradiation is visible. XRR curves are vertically shifted for the sake of clarity.

3.3. Qualitative phase analysis of inorganic oxide solar cell multilayer stack

In this section a qualitative phase analysis of oxide solar cell composed of electrochemical grown zinc oxide (ZnO) nanowires (approx. 1500 nm length; 50 nm diameter) on an Al-doped ZnO electrode (250 nm), covered with a sputter-deposited copper oxide absorber (200 - 1000 nm), a sputter-deposited nickel oxide (NiO; 40nm) electron blocking layer, and Gold dots (Au; 400nm) as contacts on top, is presented. Especially for the copper oxide absorber layer it was from high interest to determine which copper oxide phase of the two possible phases, cupric oxide (CuO) or cuprous oxide (Cu₂O), is present. Their growth strongly depends on the sputtering parameters (pressure, O₂ gas content) and only the cupric oxide (CuO) is favorable for an efficient device performance.

Detailed informations about the device architecture, performance, and characterization can be found in Dimopoulos et al. (2012). In the following, only the qualitative phase analysis by the means of specular X-ray diffraction (XRD) and GIXD is illustrated.

3.3.1. Specular XRD and GIXD investigations

Four different samples were analyzed named sancell06, sancell06 annealed, sancell05, and sancell41 in the following. First conventional specular XRD measurements were performed on a Siemens D501 diffractometer in Bragg-Brentano geometry. For the qualitative phase analysis diffraction pattern were compared with reference pattern from the Powder Diffraction File 2 (PDF2) database from the International Center of Diffraction Data (ICDD). Taking a closer look to the specular XRD pattern of sample sancell06 (black line in Figure 3.25) one can only determine 6 diffraction peaks. Three of them can be assigned to the ZnO nanowires, which are highly textured showing a columnar growth along the c-axis of their hexagonal closed packed lattice (McMurdie et al., 1986). This can be evidenced by the fact that in the specular scan only reflections (002, 103, 004) that have their lattice plane parallel to the sample surface considering (001)-texture, can be observed. From the other three peaks one is the 111 Au peak and two can be identified as the 002 and -222 peaks of the CuO phase.

The main question of this analysis was which kind of copper oxide phase (cupric oxide (CuO) or cuprous oxide (Cu₂O)) is dominating in the multilayer stack. Since a phase analysis out of two diffraction peaks for copper oxide is not satisfying GIXD was employed to further investigate the samples. Here the advantage of GIXD, in comparison to conventional specular XRD, is that due to the small incidence angle a larger sample volume is irradiated. In the case of polycrystalline thin films this highly increases the scattered intensity of each layer because more crystallites are irradiated and contribute to the diffraction signal. Furthermore, because of the in-plane geometry lattice plane normal to the sample surface are probed.

3. EXPERIMENTAL SETUP PERFORMANCE - RESULTS AND DETAILS

GIXD measurements were carried out over a $2\theta_i$ -range of 25° to 80° using a step size of $\Delta 2\theta_i = 0.05^\circ$ and an integration time of 60s. An incidence angle $\alpha_i = 0.4^\circ$ was chosen to ensure penetration of X-rays through the whole multilayer stack because this value is larger than the critical angles of total external reflection of all involved materials ($\alpha_c \text{ZnO} = 0.33^\circ$, $\alpha_c \text{CuO} = 0.34^\circ$, $\alpha_c \text{NiO} = 0.37^\circ$; Au was just present as small dots on the sample surface). Normally GIXD measurements are presented as RSM as a function of the in-plane component q_p and out-of-plane component q_z of the scattering vector q as it is shown in Figure 3.24(a). The diffraction features of polycrystalline materials and textured films with a certain mosaicity have an arc-shaped form. An integration over the q_z direction would not lead to a correct representation for a comparison with reference diffraction patterns for a phase analysis because the peak positions would be shifted. Therefore, the RSM were transformed into polar coordinates using

$$q = \sqrt{q_z^2 + q_p^2} \quad (3.12)$$

$$\varphi = \tan^{-1} \left(\frac{q_z}{q_p} \right) \quad (3.13)$$

as shown in Figure 3.24(b). Integration along φ leads to an in-plane diffraction pattern that can be compared to a reference database. The specular and in-plane XRD patterns of all samples are depicted in Figure 3.25-3.28 including the indexation of the diffraction peaks. Concerning the two possible copper oxide phases they can be best distinguished from each other by observing the 020-peak for cupric oxide (CuO) and the 200-peak for cuprous oxide (Cu₂O). Summarized we have

- in sample *sancell05*, *sancell06*, and *sancell06* annealed cupric oxide (CuO) is dominating with negligible traces of cuprous oxide (Cu₂O)
- in sample *sancell41* cuprous oxide (Cu₂O) is dominating

Furthermore, the broad peak form of the cuprous oxide (Cu₂O) peaks of sample *sancell41* are a strong indication for small crystallites. The in-plane patterns also confirm the (001)-texture of the ZnO nanowires because there the strongest ZnO peaks are 100, 101, 110 and 200. No NiO peaks were found neither in the specular nor in the in-plane pattern leading to the conclusion that this layer is amorphous.

3.3. QUALITATIVE PHASE ANALYSIS OF INORGANIC OXIDE SOLAR CELL MULTILAYER STACK

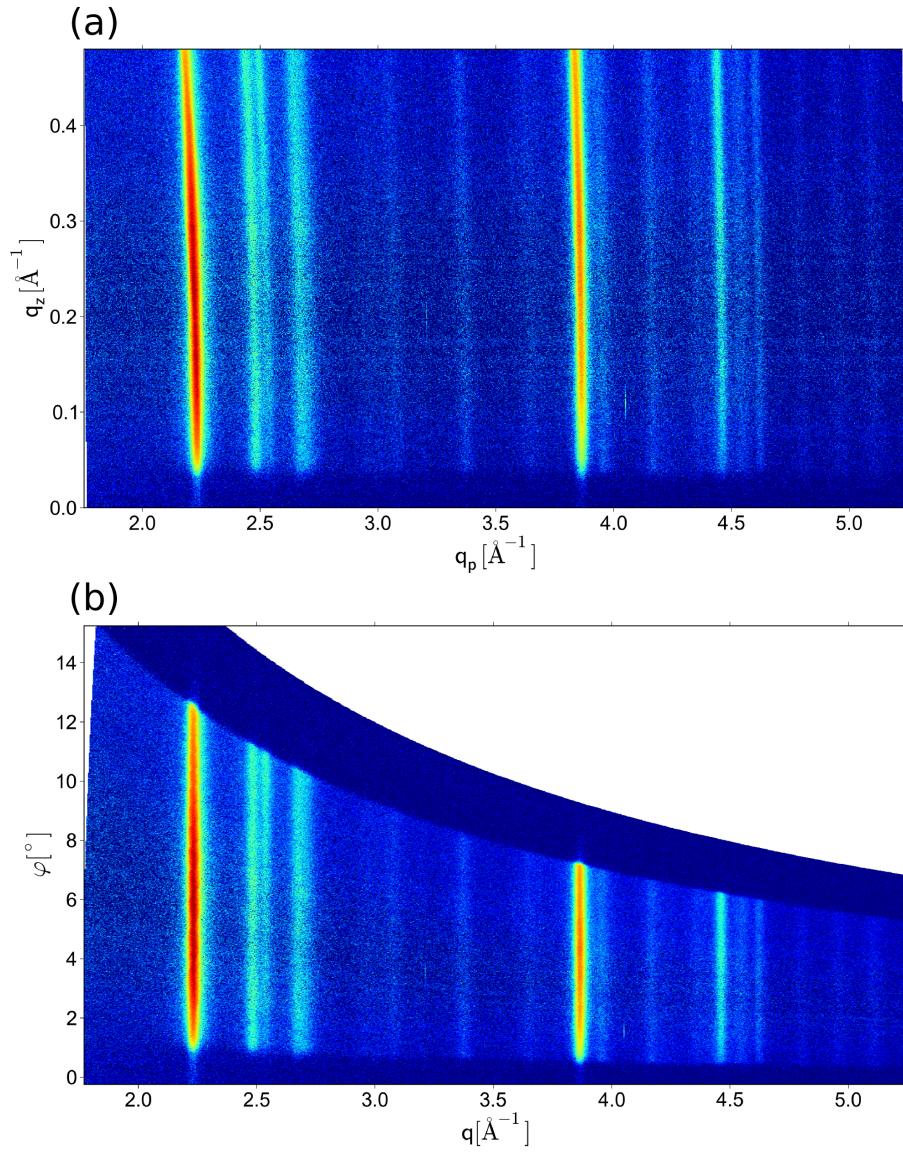


Figure 3.24.: (a) In plane reciprocal space maps (RSM) of sancell06. (b) RSM transformed in polar coordinates with $q = \sqrt{q_p^2 + q_z^2}$ and φ the polar angle.

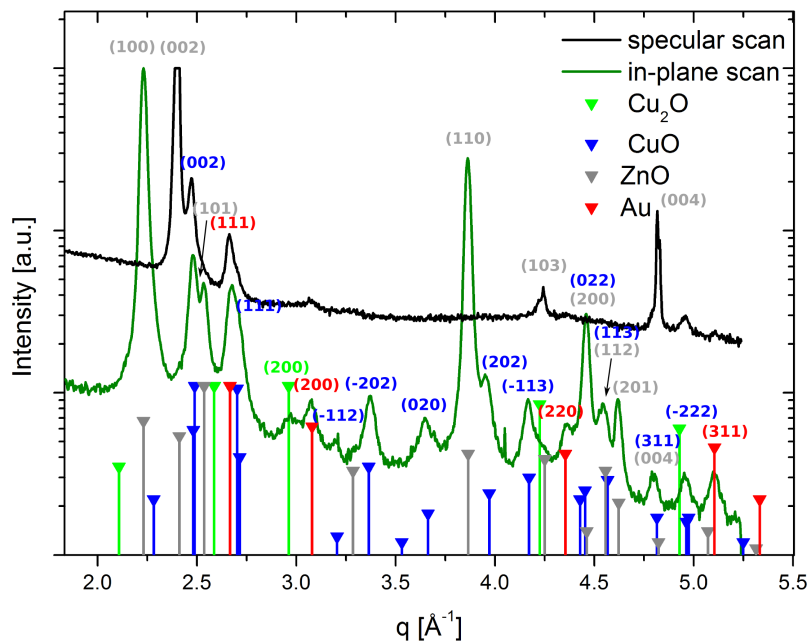


Figure 3.25.: Specular XRD and integrated in-plane scan of sample sancell06. The peaks are indexed using reference data from the database Powder Diffraction File 2 (PDF2) from the International Center of Diffraction Data (ICDD).

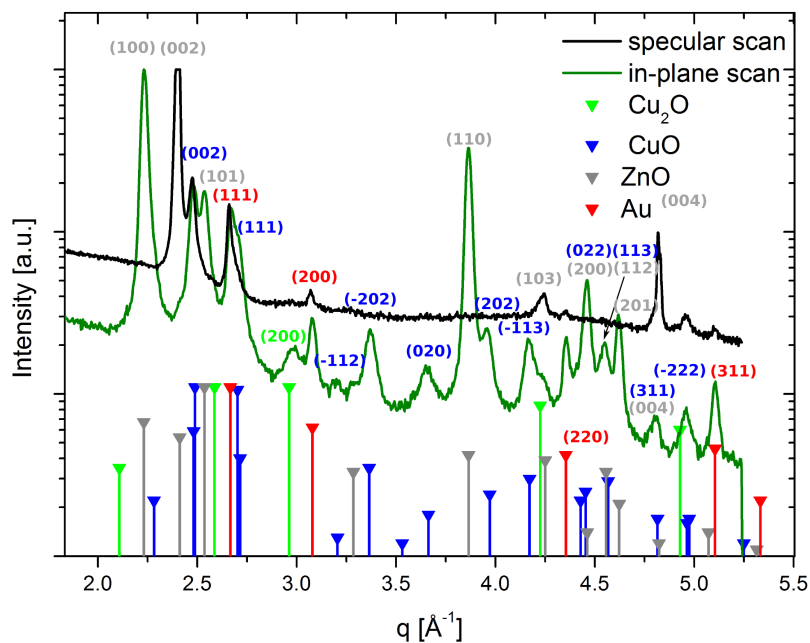


Figure 3.26.: Specular XRD and integrated in-plane scan of sample sancell06 annealed. The peaks are indexed using reference data from the database PDF2.

3.3. QUALITATIVE PHASE ANALYSIS OF INORGANIC OXIDE SOLAR CELL MULTILAYER STACK

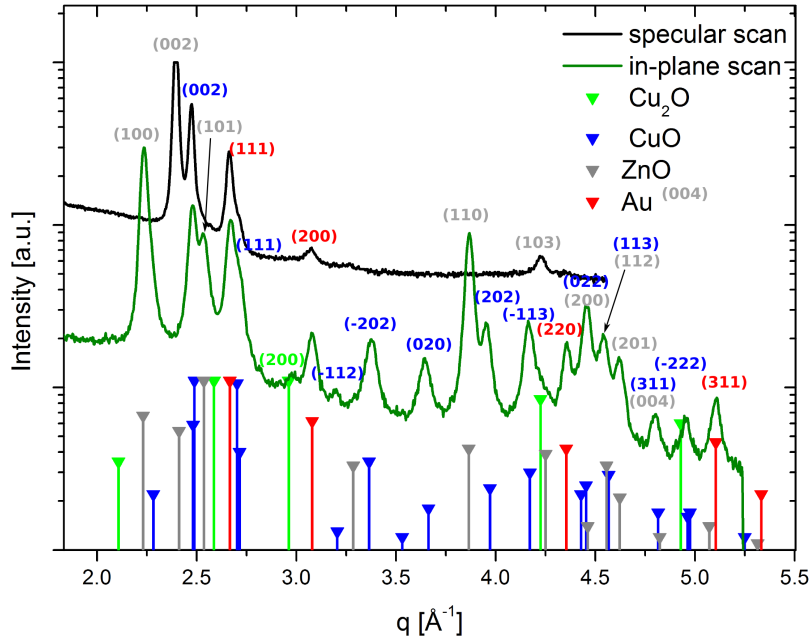


Figure 3.27.: Specular XRD and integrated in-plane scan of sample cancell05. The peaks are indexed using reference data from the database PDF2.

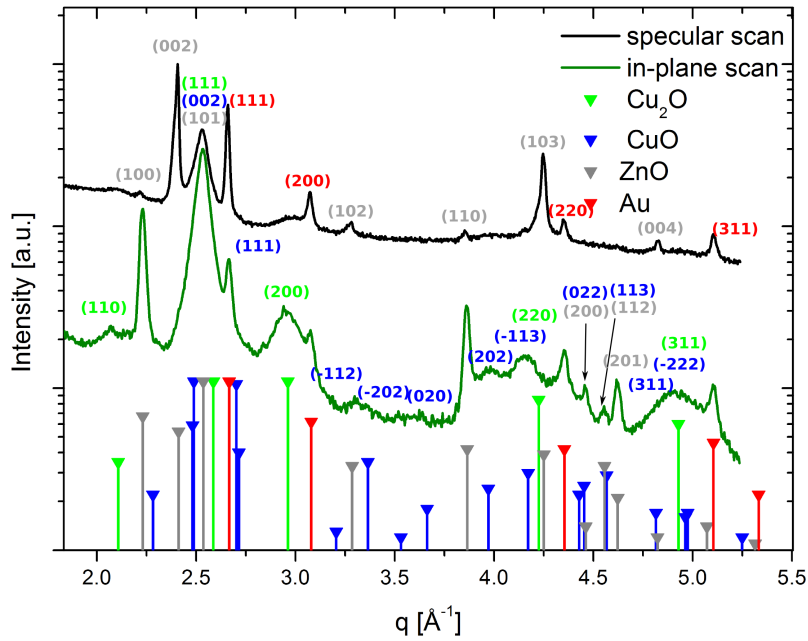


Figure 3.28.: Specular XRD and integrated in-plane scan of sample cancell41. The peaks are indexed using reference data from the database PDF2.

4. Conclusion

In this work, a novel setup for grazing-incidence X-ray diffraction (GIXD) using standard laboratory equipment is presented and its potential and experimental performance illustrated on different systems of organic and inorganic semiconductors for thin film applications.

- For the case of pentacene thin films and multi-/monolayers it could be demonstrated that this experimental approach provides an effective possibility to characterize their in-plane structure in the laboratory at a reasonable timescale. A 100 times longer integration time for 50 nm pentacene thin films leads to results of the same quality as synchrotron measurements. Further, the results clearly demonstrate that high quality GIXD studies can be performed with laboratory sources even in the monolayer range. It is shown that the quantity of matter of one pentacene monolayer ($6.52 \text{ electrons } \text{\AA}^{-2}$) is sufficient enough to perform an in-plane X-ray diffraction study which allows the clear observation of Bragg rods. In addition, X-ray reflectivity and atomic force microscopy investigations evidence a almost fully closed 1 monolayer (ML) sample and the evolution of a 3 dimensional structure in 2 and 3 ML case. The only problem is degradation of the mono- and multilayers samples after X-ray irradiation due to the formation of ozone near the sample surface. Therefore, measurements under inert atmosphere or vacuum should be considered.
- A detailed study of the crystalline structure and layer morphology of quinquethiophene SAMs based on XRR and GIXD experiments was fully performed using laboratory equipment. The XRR measurements revealed a dense packed monolayer with fully upright standing molecules that is confirmed by the occurrence of Bragg rods in GIXD measurements. Furthermore, from the clearly visible Bragg rods a long range in-plane order could be deduced leading to the conclusion that the quinquethiophene backbone of the SAM crystallizes in a 2 dimensional rectangular unit cell with 2 molecules per unit cell arranged in a herringbone packing. Remarkable is the achieved quality of the GIXD measurements that compares perfectly to studies performed using synchrotron radiation facilities.
- The presented setup is also applicable on inorganic thin films characterization. Only the combination of specular X-ray diffraction and GIXD allowed a successful phase analysis of copper oxides in an inorganic oxide solar cell.

On the whole, it could clearly be demonstrated that the presented GIXD setup provides a powerful techniques to investigate the in-plane structure of thin films in the

4. CONCLUSION

laboratory even down to the monolayer range. In combination with our existing XRR setup we have now all the tools necessary to successfully perform thin-films characterizations and are no longer limited to GIXD experiments at synchrotron radiation facilities.

Appendix

A. GIXD setup: how to align and measure

A.1. Alignment of the GIXD setup

For the alignment of the GIXD setup we have to align the X-ray beam to the center of rotation (COR) of the goniometer. For this purpose, the x-, y-, and z- coordinates of the COR have to be known. They can be determined using a centering pin and following the instructions given in the *BRUKER User's Manual of the centric Eulerian cradle*. Their coordinates of the COR were found to be $x = 0.07$ mm, $y = 1.11$ mm, $z = 0.66$ mm.

Before aligning the beam to the COR it has to be checked if the X-ray tube is perfectly vertically oriented. This can be done by using a fluorescent screen. The vertically collimated X-ray beam emitted from the multilayer mirror should appear as horizontal line. If it is not perfectly horizontal, the whole X-ray tube can be rotated by the manual tube rotation and adjustments of the corresponding set screw at the back (see Figure A.1 or for more details see *BRUKER Ultra GID User Manual*). Maybe the primary Soller slits have to be removed to increase the primary beam intensity for a better visibility of the beam at the fluorescent screen.

Now the primary beam can be aligned to the COR of the goniometer. During the whole alignment process the slit after the multilayer mirror is chosen with 0.1 mm and a point detector with 6mm slit in front is used. Inside the primary 0.1 mm slit one copper absorber has to be inserted inserted to attenuate the primary beam. This is very important not to destroy the detector. The point detector is mounted behind the Soller slits which are positioned at the 160 mm position on the track. The position of 160 mm is chosen because it is the closest possible position to the COR where no collisions with the centric Eulerian cradle are guaranteed.

A glass slit has to be mounted to the sample stage and the stage has to be moved to the x-, y-, z-positions of the COR. The glass slit ensures that only a beam parallel to the sample stage surface can pass the COR, which is important for the beam height and α_i motor alignment. First a z-scan with $\alpha_i = 0$ has to be performed from 0 mm to 1 mm with a step size of $\Delta z = 0.01$ mm. The measured peak maximum should be at $z = 0.66$ mm. If the maximum is at a different position the whole X-ray tube can be manually translated, i.e. the direct beam can be translated up and down, using the manual height adjustment screw behind the X-ray tube as indicated in Figure A.1. The height of the tube has to be adjusted so that after performing a z-scan the maximum is at $z = 0.66$ mm. After the height adjustment the α_i motor can be aligned.

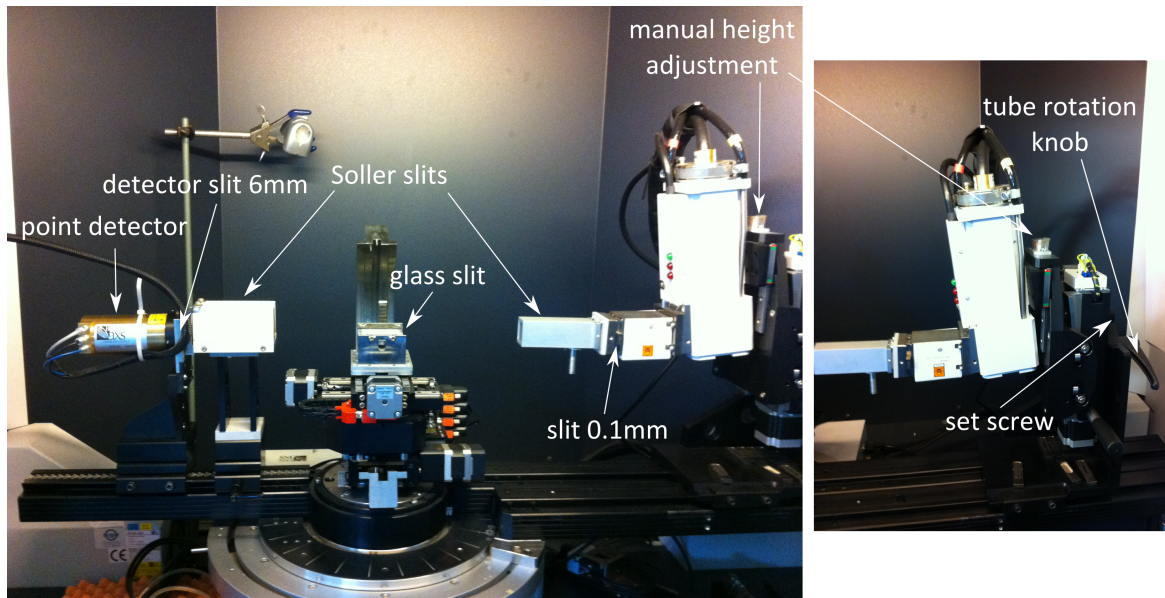


Figure A.1.: Photograph of the experimental setup with mounted glass slit and point detector.

The glass slit is moved again at the x , y , z positions of the COR and an α_i -scan from -0.2° to 0.2° with a step size of $\Delta\alpha_i = 0.01^\circ$ is performed. The resulting peak should have its maximum at $\alpha_i = 0^\circ$. If this is not the case the actual peak value should be set to zero. This can be done by pressing the set new Zi-value button in the *BRUKER XRD Commander*. After the α_i alignment again the height adjustment should be checked by a z -scan because height adjustment and α_i alignment are correlated.

Furthermore, a 2θ -scan (detector scan) should be performed to ensure that the 2θ motor and secondary Soller slits are well aligned. If there is a large deviation from the zero position in 2θ the alignment of the Soller slits should be checked. This can be done by dismounting the Soller slits and using a double slit optic to determine the 2θ zero position. Then the Soller slit can be mounted again and aligned to this position by 3 screws on the back of its housing. For very small deviations it is sufficient to set the peak value to zero by pressing the set new Zi-value button. Now the setup is fully aligned and ready for measurements. Only the point detector has to be replaced by the one dimensional Vantec detector. The settings for the Vantec detector which can be set in the *BRUKER Diffrac Plus Config* program are shown in Figure A.2.

A.2. GIXD Measurements

First, a step by step description of how to perform a measurement using the Vantec-1 detector is given. Since the Vantec-1 detector and the *BRUKER XRD Commander* control software are optimized for fast powder diffraction scans, where the detector simultaneously records X-ray diffraction patterns within a wide 2θ -range, a workaround using macros had to be used to move different motors and read out the detected one

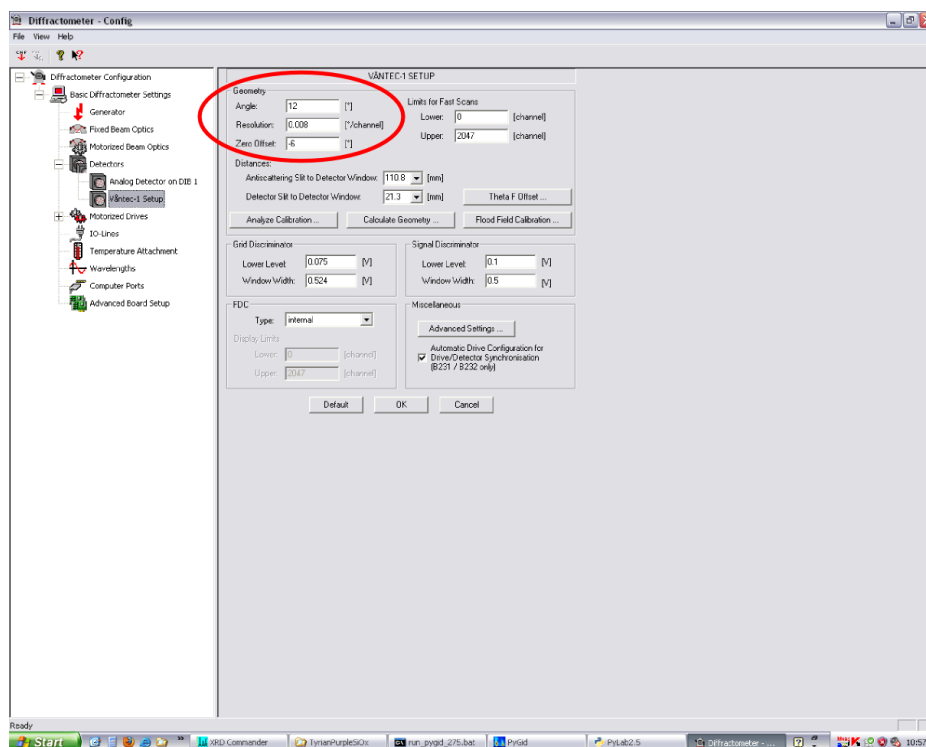


Figure A.2.: Settings of the Vantec detector in the *BRUKER Difract Plus Config* program (Angle=12; Resolution=0.008; Zero Offset=-6).

dimensional intensity distributions. Macros can be programmed using the *BRUKER XRD Wizard*. In Figure A.3 all needed steps are shown to set up a macro

1. Start a new HRXRD macro
2. Set all the drive positions. This can be done by clicking in the *BRUKER XRD commander* on the transmit drive position button and then importing the drive positions inside the wizard by the clicking get drive positions button.
3. In the tab 'detector selection' PSD: *Vantec-1* has to be selected and the PSD electronic window has to be set to 24°.
4. As scan type *Theta_f_Scan* has to be chosen.
5. In the tab 'scan parameters' the time for each measurement step can be set.
6. In the tab 'loops' the motor which should be changed during the measurement can be selected. Also the start and stop values, and the step size can be set.

The macro has to be saved and can be loaded inside the *BRUKER XRD commander* to start the measurement.

Prior to starting a GIXD measurement the sample has to be aligned. The goal of the alignment is to align the sample surface parallel to the in-plane scattering plane,

A. GIXD SETUP: HOW TO ALIGN AND MEASURE

i.e. to align the sample perfectly horizontal. This can be done following this step by step procedure

1. After mounting the sample to the sample tilt stage it has to be pre-aligned using a laser. The reflection of a laser shining on the sample has to be observed. Thereby, the sample is rotated from 0° to 90° to 180° to 270° around its vertical axis (φ) and the reflected laser position is marked for each position. The laser reflection moves around a circle and if the sample surface is perfectly perpendicular to the vertical rotation axis the reflections stays at one point while rotating the sample. Thus, the marked position of 0° and 180° , and 90° and 270° have to be connected by a straight line. Now the laser reflection has to be moved to the intersection of this two lines by moving the ξ - and ζ -motors of the sample tilt stage. The best way to control the movements of the ξ - and ζ -motors is to start the *BRUKER D8 Tools* program. There it is possible to move both motors continuously.
2. After the pre-alignment, the sample can be aligned in the X-ray beam. A primary slit of 0.1 mm (with one copper absorber) should be used to minimize the footprint of the direct beam on the sample. Now a z-scan is performed and the sample is moved to the z-position that corresponds to half of the intensity, i.e. the sample is positioned in the middle of the direct beam.
3. Now the horizontal alignment of the sample surface can be refined. Normally one would do this by scanning the ζ and ξ motors to rock the sample and maximize the intensity, however both motors have a large backlash, so the real motor position and the shown position show a too large deviation for a satisfying alignment. Therefore a different alignment approach is taken. The angle of incidence α_i is scanned from -0.2° to 0.2° and the reflected and direct beam are observed with the one dimensional detector. The direct beam is the beam that passes the sample without shining on the sample. This happens because the beam height is set with the primary slit to 0.1 mm and a very small angle of incidence is used resulting in a footprint on the sample surface that is larger than the sample size. The sample is perfectly horizontal if the direct beam and the reflected beam intersect at $\alpha_i = 0^\circ$ or in other words if one starts seeing a reflected beam exactly at $\alpha_i = 0^\circ$. The α_i -scans can be analyzed using a python script. In the Pylab2.5 shell the commands shown in Figure A.4 should be executed. First with `cd C:\diffdat1\markus_neusch\python_live` the working directory of the python shell is changed to the folder that contains the script. Then with `run alphaialignement_mod.py [relative path of the alphaifile.raw] [motor name]` the script is started and a figure opens that shows a color map of the measurement. There the direct and the reflected beam can be seen as shown in Figure A.4. Now 6 clicks have to be made to define two trapezia, one for the reflected and one for the direct beam as indicated in Figure A.4 (first click=lower left corner of first trapezium(ft); second click=lower right corner of ft; third click=upper left corner of ft; fourth click=lower left corner of

second trapezium(st); fifth click=lower right corner of st; sixth click=upper left corner of st). Wrong clicks can be erased by a right click. The python script searches now for the maxima in each of the two trapezia and fits a linear fit to them which can be seen in a new opening figure. The two linear fits are intersected and the intersection is printed in the shell. So the α_i -value at which one starts to see a reflected beam can be calculated. This value should be smaller than $|\alpha_{i-intersect}| < 0.01^\circ$. If it is larger/smaller than $|0.01|$ the motor (ξ or ζ) that tilts the sample around the axis normal to the direct beam (it depends on the φ position which motor is the right one) has to be moved and the α_i -scan repeated until $-0.1^\circ < \alpha_{i-intersect} < 0.01^\circ$. A good tactic is to add or subtract (depending on the misalignment) to the ξ or ζ motor position the $\alpha_{i-intersect}$ value. Now also z-scans have to be repeated to verify that the sample is still in the middle of the direct beam. This can be speeded up by performing just shots with the Vantec detector and looking at the primary beam intensity there.

Now the sample surface is partly horizontal aligned. There is still the alignment of the sample tilt axis that is parallel to the primary beam missing. Now either the sample can be rotated 90° around the φ -axis and again α_i -scans are performed or, which is the recommended method for all powder samples (no φ -rotation is needed for measurements), the χ -circle is used to align the sample surface horizontal around the missing axis.

4. For this alignment the angle of incidence α_i is set to 0.15° and φ is scanned from 88° to 94° . Then the reflected beam, which appears at an exit angle $\alpha_f = 0.15^\circ$ is integrated over α_f and the χ -position corresponding to the maximum is the right position for a horizontal aligned sample (see Figure A.5)
5. Now the sample is perfectly horizontal aligned and a GIXD measurement can be started.

A. GIXD SETUP: HOW TO ALIGN AND MEASURE

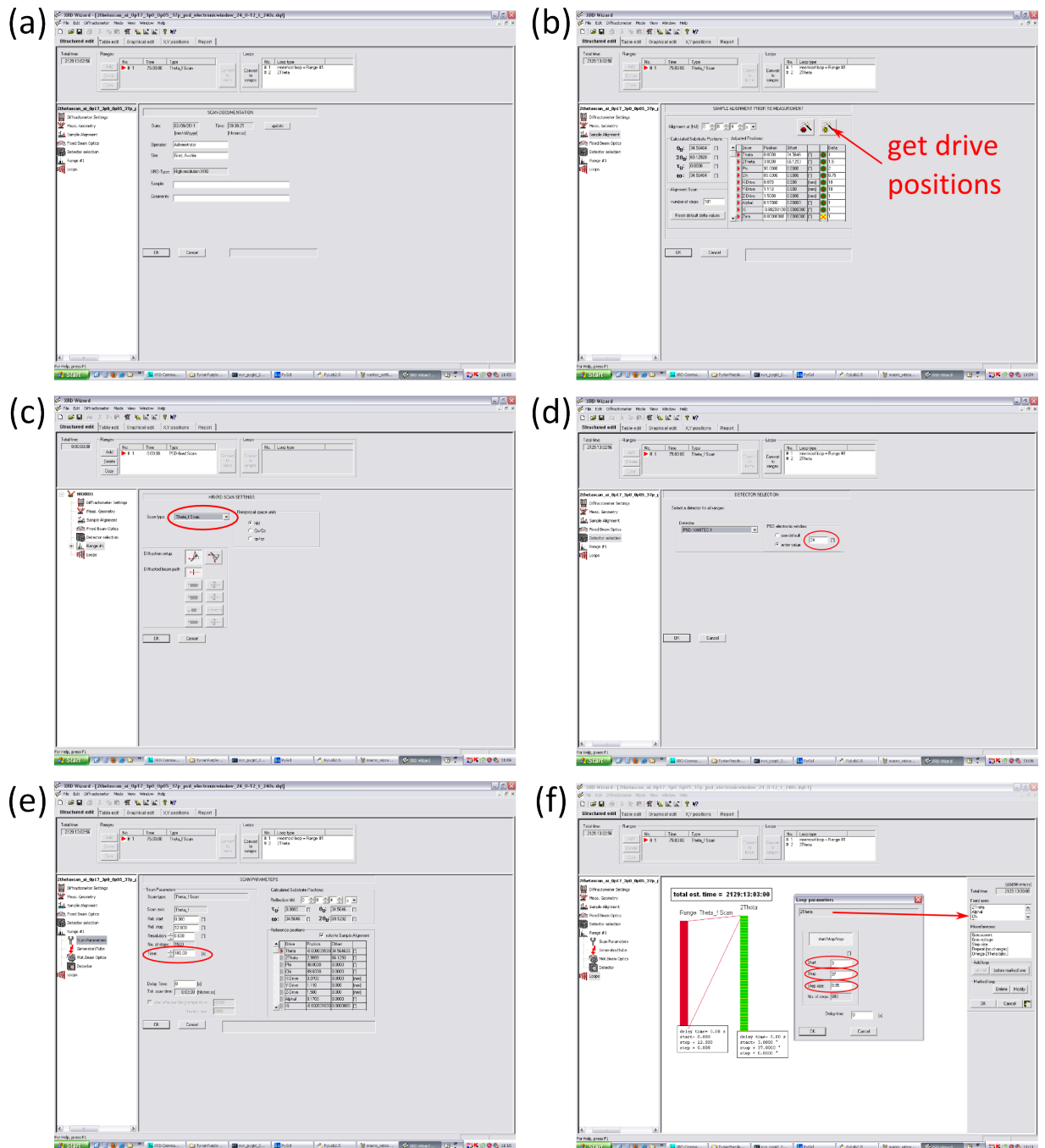


Figure A.3.: Steps to set up a macro for XRD measurements using the *BRUKER XRD Wizard*.

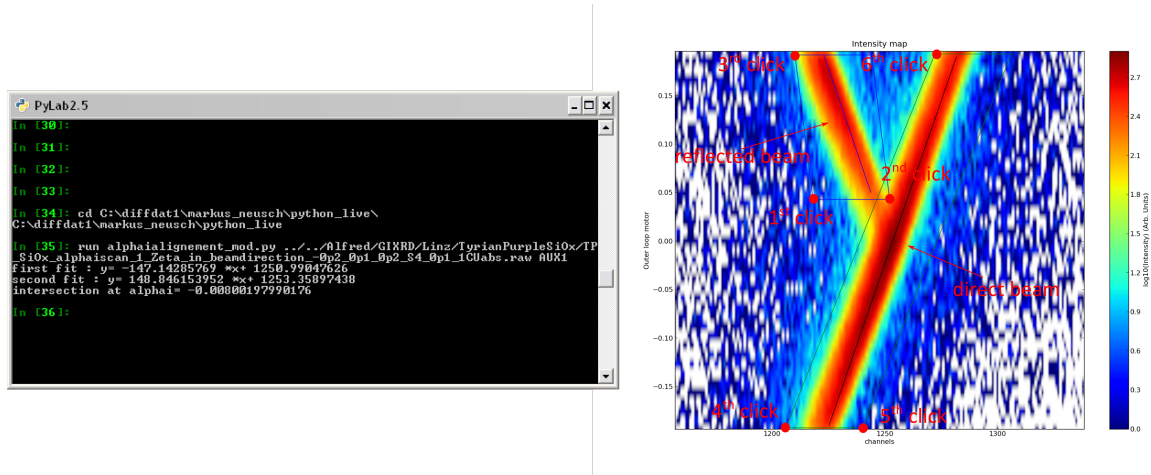


Figure A.4.: *Pypython 2.5* shell and commands to run the alignment script. The color map on the right shows the channels of the 1 dimensional PSD for the different α_i -values of the alignment scan (on the x-axis are the detector read out channels and on the y-axis are the different α_i -values). We can see that the sample is well aligned because one starts to see a reflected beam exactly at $\alpha_i = 0^\circ$. Also the clicks inside the colormap necessary to define two trapezia are indicated (see text for details).

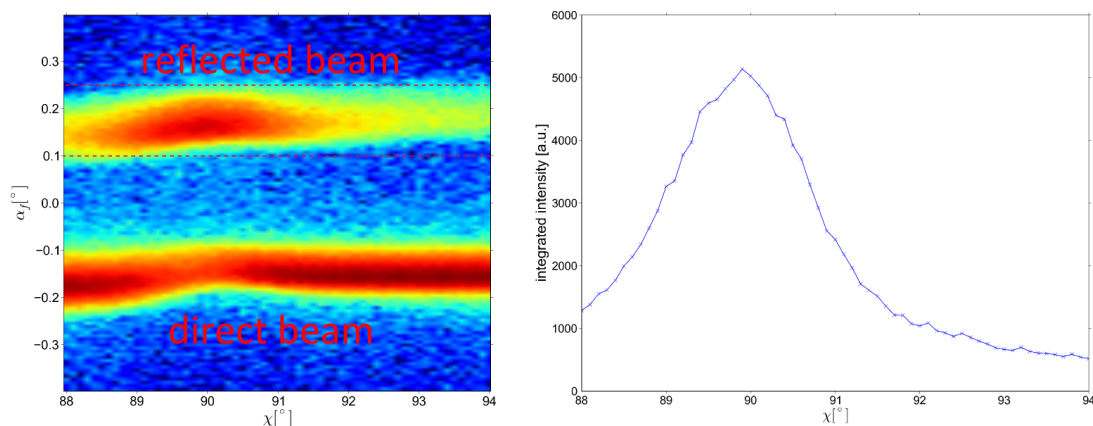


Figure A.5.: χ -scan at an angle of incidence of $\alpha_i = 0.15^\circ$ (thus the reflected beam appears at an exit angle of $\alpha_f = 0.15^\circ$). Line scan over the integrated area indicated in red in the colormap. The maximum is the χ -position where the sample surface is horizontal aligned.

B. Coplanar diffraction configuration

The experimental setup can also be used in a coplanar diffraction configuration to perform X-ray reflectivity or conventional specular X-ray diffraction experiments. In Figure B.1 schematics of the two possible setup configurations are shown. Here the coplanar diffraction setup is described shortly and a description of the alignment process is given.

In XRR or conventional specular diffraction mode the sample is adjusted by the angle χ to have its surface perpendicular to the horizontal scattering plane (Figure B.1a). The X-ray tube is in the position with the line focus also perpendicular to this plane. For detection, a NaI scintillation detector in combination with a 0.1 mm secondary and 0.1 mm receiving slit to set the angular detector acceptance and an automatic rotary absorber (not drawn in the schematics) are used. The angle of incidence of the X-rays is set by the θ -circle and the scattering angle (2θ) by the detector circle. Thus, in this scattering mode conventional $\theta/2\theta$ scattering experiments are performed probing the out-of-plane order, i.e. planes that are parallel to the substrate surface. In this configuration the Vantec-1 detector can be used in a horizontal configuration to perform fast powder diffraction experiments. Details for the detector alignment of this configuration can be found in *BRUKER VANTEC-1 Detector User Manual*. Due to the good out-of-plane collimation of the primary X-ray beam by the multilayer mirror, this setup is also perfectly suited to perform XRR measurements on thin films.

B.1. Alignment of coplanar configuration

The X-ray tube is translated to the position with the line focus perpendicular to the scattering plane (horizontal plane) (see Figure B.1a). A fluorescent screen is used to check if the line focus is perfectly vertical. If it is tilted it can be aligned by the set screw at the back of the X-ray tube (similar as shown in Figure A.1).

The alignment of the coplanar configurations works in two main steps. Because the X-ray tube is now with its line focus perpendicular to the scattering plane the α_i -motor moves the whole tube on a circle inside the horizontal plane and is not longer setting an angle of incidence. Therefore, first the right α_i angle has to be found to align the primary beam parallel to the optical axis. Then the whole X-ray tube is translated manually using the manual height adjustment screw to get the beam into the COR.

To align the beam parallel to the optical path a pinhole is mounted to the sample stage and moved to the x-, y-, and z-positions of the COR. The point detector is used

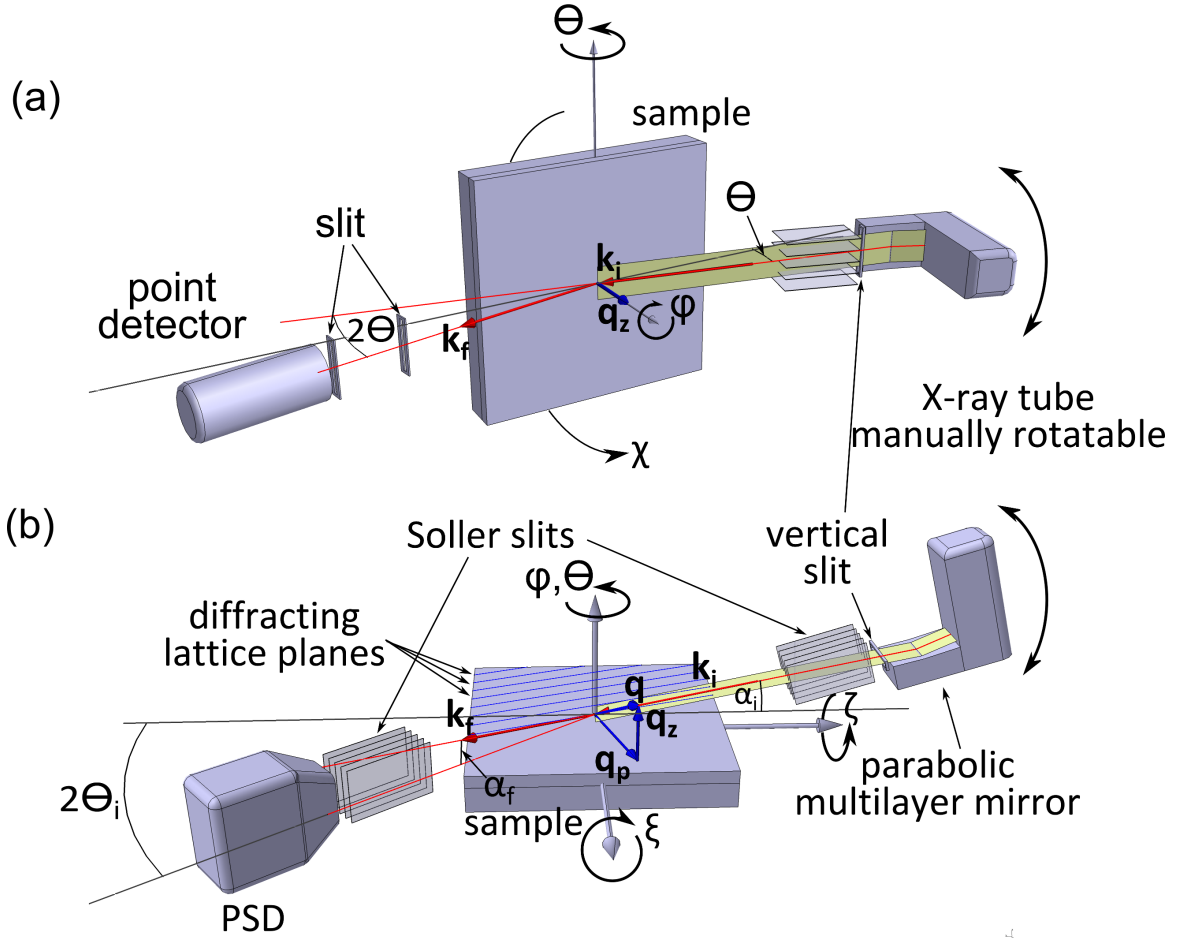


Figure B.1.: Schematic of the experimental setup; the two possible configurations are shown. (a) Corresponds to the X-ray reflectivity configuration and (b) to grazing incidence in-plane X-ray diffraction. The wave vectors of the incident wave and a scattered wave (\mathbf{k}_i and \mathbf{k}_f , respectively), the corresponding momentum transfer \mathbf{q} , and its in-plane and out-of-plane components (q_p and q_z , respectively) are indicated. A detailed description is given in the text.

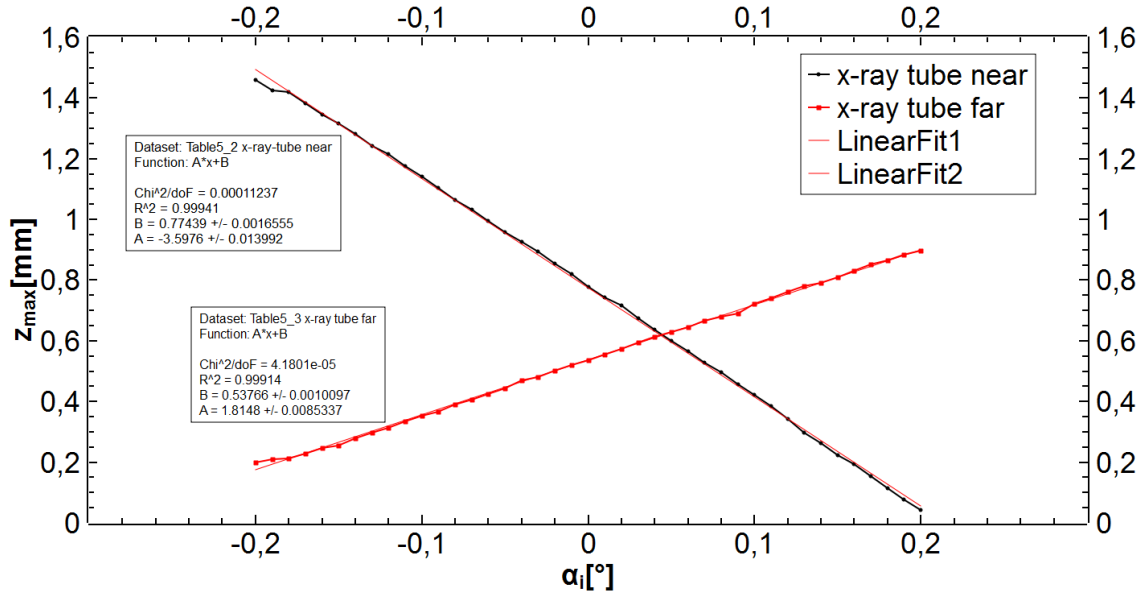


Figure B.2.: Maxima of the z-scans in dependency of the angle of incidence α_i for a X-ray tube position near and far from the COR. The lines are linearly fitted to obtain the intersection.

without Soller slits but with a 6 mm receiving slit in front. There is also no primary Soller slits used only a primary slit with 0.1 mm and 1 copper absorber. The whole X-ray tube is now translated on its track to a very close position to the COR. Then z-scans are performed at different α_i -positions. Z is scanned from -0.5 mm to 2 mm with a step size of 0.2 mm and α_i is looped from -0.2° to 0.2° with a step size of 0.01° . Now the X-ray tube is moved to a position far away to the COR (the farthest position possible) and the same scans are repeated. From each of this z-scans the maximum is determined and plotted in dependency of α_i . So one gets two straight lines and the α_i -value at the intersection is the right α_i -value for a primary beam parallel to the optical axis (see Figure B.2).

As final step the X-ray tube is translated to the designated position on its track and a glass slit is mounted. Z-scans are performed and the X-ray tube is manually translated by the manual height adjustment screw until the maximum of the z-scan is at the corresponding z-value of the COR ($z=0.66\text{mm}$). Now the coplanar setup is aligned and ready for measurements.

C. Paper published at the Journal of Applied Crystallography, Volume 45, Part 2, pages 367-370

The experimental setup established during this work to perform grazing incident in-plane X-ray diffraction experiments in the laboratory was published in the Journal of Applied Crystallography, Volume 45, Part 2, pages 367-370. The results obtained for pentacene thin films and multi- and monolayers in comparison to the synchrotron data are presented. In the following pages the electronic reprint is shown. Reproduced with permission of the International Union of Crystallography. The original paper can be found at <http://dx.doi.org/10.1107/S0021889812000908>.

Grazing-incidence in-plane X-ray diffraction on ultra-thin organic films using standard laboratory equipment

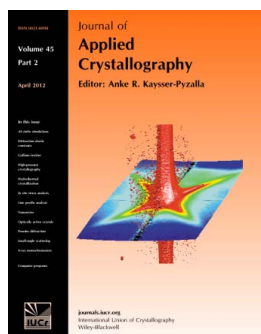
Markus Neuschitzer, Armin Moser, Alfred Neuhold, Johanna Kraxner, Barbara Stadlober, Martin Oehzelt, Ingo Salzmann, Roland Resel and Jiří Novák

J. Appl. Cryst. (2012). **45**, 367–370

Copyright © International Union of Crystallography

Author(s) of this paper may load this reprint on their own web site or institutional repository provided that this cover page is retained. Republication of this article or its storage in electronic databases other than as specified above is not permitted without prior permission in writing from the IUCr.

For further information see <http://journals.iucr.org/services/authorrights.html>



Journal of Applied Crystallography covers a wide range of crystallographic topics from the viewpoints of both techniques and theory. The journal presents papers on the application of crystallographic techniques and on the related apparatus and computer software. For many years, the *Journal of Applied Crystallography* has been the main vehicle for the publication of small-angle scattering papers and powder diffraction techniques. The journal is the primary place where crystallographic computer program information is published.

Crystallography Journals **Online** is available from journals.iucr.org

Grazing-incidence in-plane X-ray diffraction on ultra-thin organic films using standard laboratory equipment

Received 3 October 2011
Accepted 9 January 2012Markus Neuschitzer,^{a*} Armin Moser,^a Alfred Neuhold,^a Johanna Kraxner,^b Barbara Stadlober,^b Martin Oehzelt,^c Ingo Salzmann,^d Roland Resel^a and Jiří Novák^a^aInstitute of Solid State Physics, Graz University of Technology, Austria, ^bJoanneum Research Forschungsgesellschaft mbH, Institute of Surface Technologies and Photonics, Weiz, Austria, ^cHelmholtz Zentrum Berlin für Materialien und Energie – BESSY II, Germany, and ^dInstitut für Physik, Humboldt Universität zu Berlin, Germany. Correspondence e-mail: n_markus@sbox.tugraz.at

A novel grazing-incidence in-plane X-ray diffraction setup based on a commercial four-circle diffractometer with a sealed-ceramic copper X-ray tube, upgraded with parabolic graded multilayer X-ray optics and a one-dimensional position-sensitive detector, is presented. The high potential of this setup is demonstrated by a phase analysis study of pentacene thin films and the determination of in-plane lattice constants of pentacene mono- and multilayers. The quality of the results compare well to studies performed at synchrotron radiation facilities.

© 2012 International Union of Crystallography
Printed in Singapore – all rights reserved

1. Introduction

Grazing incidence in-plane X-ray diffraction (GIXD) is a powerful technique to solve problems in materials science. First established by Marra *et al.* (1979) to study crystal surfaces and interfaces, it is now widely used to determine in-plane order and crystalline properties of thin films. In GIXD, X-rays impinge on the sample surface at a grazing angle below the angle of total external reflection, resulting in an evanescent wave propagating parallel to the surface. Perpendicular to the surface, its amplitude is exponentially damped, *i.e.* its penetration depth is limited to several nanometres depending on the incidence angle, the wavelength of the radiation and the electron density of the material (Vineyard, 1982). Therefore, in a GIXD experiment the evanescent wave is scattered only by the first few surface layers, resulting in an exceedingly increased surface sensitivity. Moreover, the wavefield amplitude of the evanescent wave is enhanced up to a factor of two because incident, reflected and transmitted wavefields couple coherently at the surface (Dosch, 1992). As a result, GIXD allows scattering experiments to be performed on thin films of very low scattering volume (Resel *et al.*, 2006; Novák *et al.*, 2011). Because of its scattering geometry (see Fig. 1), GIXD probes lattice planes that are almost perpendicular to

the surface, and thus the in-plane structure of the sample can be determined. GIXD even allowed, for the first time, the characterization of the structure of ordered organic monolayers (Als-Nielsen *et al.*, 1994; Kaganer *et al.*, 1999).

Nowadays, GIXD measurements are mostly performed using synchrotron radiation sources of high brilliance. However, an increasing interest in GIXD setups in laboratories arose with the emergence of more sophisticated X-ray optics (Tanner *et al.*, 2004). This work shows in detail the realization of a novel GIXD setup in the laboratory and its successful application on pentacene thin films and monolayers. Even for monolayer films, we demonstrate that our setup allows us to achieve results comparable to those obtained by a synchrotron radiation facility.

2. Experimental setup

The GIXD setup is based on a commercial four-circle Bruker D8 Discover diffractometer upgraded with the Bruker Ultra GID add-on, which allows rotation of the X-ray tube to set the angle of incidence (α_i) of the X-ray beam towards the substrate surface. It is possible to tune the angle of incidence between -3.5 and 6.5° with a resolution better than 0.01° while keeping the sample horizontal; the experimental setup is illustrated in Fig. 1.

A conventional 2.2 kW water-cooled X-ray tube with a copper anode in line-focus mode is used as X-ray source. The divergent X-ray beam emitted from the line-shaped source is collimated by a 60 mm-long parabolic graded multilayer mirror (Schuster & Gobel, 1995), leading to an out-of-plane divergence better than 0.025° . In addition, the multilayer mirror acts as monochromator, which suppresses the intensity of Cu $K\beta$ radiation to less than 1% of the Cu $K\alpha$ radiation. The in-plane incoming beam divergence is adjusted by Soller slits to 0.35° . The resulting beam has dimensions of 1.1 mm in height and 12 mm in width and can be limited in height by a vertical slit after the multilayer mirror. The reached flux density of the X-ray beam is 8.6×10^6 photons $(\text{s mm}^2)^{-1}$.

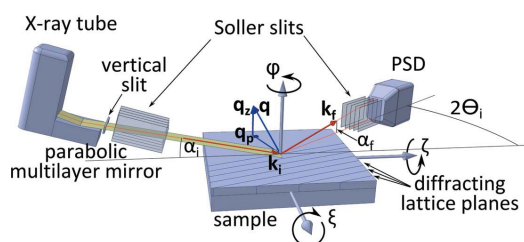


Figure 1
Schematic of the experimental setup. The wavevectors of the incident wave and a scattered wave (\mathbf{k}_i and \mathbf{k}_f , respectively), the corresponding scattering vector \mathbf{q} , and its in-plane and out-of-plane components (q_p and q_z , respectively) as well as the probed lattice planes are indicated. A detailed description is given in the text.

The sample is attached to an Eulerian cradle with a sample stage that allows translations in all three directions (x , y , z) and rotations around the vertical axis (φ). In addition, the sample holder can be tilted in two perpendicular directions (ξ , ζ) to align the sample surface normal to the rotation axis (φ).

To reduce measurement time, a one-dimensional position-sensitive detector (PSD; Vantec-1; Khazins *et al.*, 2004) is used to collect scattering intensity profiles along the out-of-plane direction with a resolution of $\Delta\alpha_f = 0.007^\circ$. The angular resolution of the PSD is calibrated by scanning the X-ray angle of incidence (α_i) from the lowest to the highest possible value, *i.e.* by scanning the (attenuated) primary X-ray beam over the whole detector range. Thus a linear dependency between the detector read-out channels and the exit angle (α_f) can be calculated. In our present setup, the PSD covers an out-of-plane range (α_f) of 7.3° in one single shot. A set of Soller slits in front of the PSD defines the angular in-plane detector acceptance as 0.35° .

The presented scattering geometry probes lattice planes that are nearly perpendicular to the sample surface, as indicated in Fig. 1. Thus, this setup is perfectly suited to characterize the in-plane order of epitaxially grown films as well as two-dimensional powders (*i.e.* fiber-textured films). In such samples, all crystallites are oriented with the identical lattice plane parallel to the substrate surface while their azimuthal orientations (*i.e.* with respect to the sample surface) are statistically distributed. This specific growth mode is typically found for ordered organic monolayers or organic thin films grown on isotropic surfaces. In this case, complete crystallographic information can be revealed by in-plane diffraction at one specific azimuthal angle φ (Mannsfield *et al.*, 2011; Salzmann *et al.*, 2011; Moser *et al.*, 2009).

3. Experimental details and data processing

The experimental results of the GIXD measurements are visualized and analyzed using the custom-made software *PyGid* (Moser, 2011), which allows transformation to q space, indexing of Bragg peaks, and intensity extraction into horizontal and vertical directions. In the following, GIXD data are shown as reciprocal-space maps (RSMs) as a function of the in-plane component q_p and out-of-plane component q_z of the scattering vector \mathbf{q} [$q = (4\pi/\lambda)\sin\theta$] (Fig. 1). The intensities recorded with the one-dimensional PSD were corrected using a flat-field correction to guarantee equal sensitivity over the whole detector range. RSMs of all presented samples were measured under ambient conditions with an incidence angle equal to the critical angle of total external reflection of pentacene, which corresponds to 0.17° for Cu $K\alpha$ radiation ($\lambda_{\text{Cu}K\alpha} = 1.542 \text{ \AA}$). For the used vertical slit size of 0.6 mm, this incidence angle leads to a 202 mm footprint of the direct beam on the sample surface plane. The sample size of all investigated samples was $20 \times 20 \text{ mm}$.

4. Experimental setup performance

4.1. Pentacene 50 nm thin films

Pentacene, one of the most thoroughly studied materials in the field of organic electronics, exhibits several polymorphs slightly different from its bulk crystal structure (Mattheus *et al.*, 2001). Pentacene deposited as a thin film on SiO_2 grows as a two-dimensional powder, making in-plane diffraction necessary to solve its crystal structure, as was shown independently by Yoshida *et al.* (2007), Nabok *et al.* (2007) and Schiefer *et al.* (2007). An RSM of a nominally 50 nm thin pentacene film prepared on a thermally oxidized silicon wafer (SiO_2) is depicted in Fig. 2(a). This RSM was

recorded with a step size of $\Delta 2\theta_i = 0.05^\circ$ using the described setup (integration time of 180 s per step). The presence of a dominating thin-film-phase portion (black dots) and an additional less pronounced contribution of the bulk phase (white dots) (Campbell *et al.*, 1962) can clearly be seen.

A comparison between synchrotron and laboratory data is presented in Fig. 2(b). Synchrotron measurements were carried out at the HASYLAB (DESY, Hamburg, Germany) Doris W1 beamline using a wavelength $\lambda = 1.180 \text{ \AA}$, an incidence angle of $\alpha_i = 0.15^\circ$, a step size of $\Delta 2\theta_i = 0.05^\circ$ and an integration time of 2 s per step. For detection, a one-dimensional Mythen detector was employed, which covers an out-of-plane range (α_f) of 4° in one shot. In the used configuration the primary beam reaches a flux density of $3.1 \times 10^{10} \text{ photons (s mm}^2\text{)}^{-1}$. The beamline provides a good trade-off between intensity and beam damage since beam damage plays a nonnegligible role in the characterization of organic materials using synchrotron radiation (Neuhold *et al.*, 2012). In Fig. 2(b) the diffraction intensities integrated over a q_z range from 0 to 0.46 \AA^{-1} followed by background subtraction are shown for the same pentacene thin-film sample. Each peak was fitted with a Lorentzian to compare the peak areas and full widths at half-maximum (FWHMs).

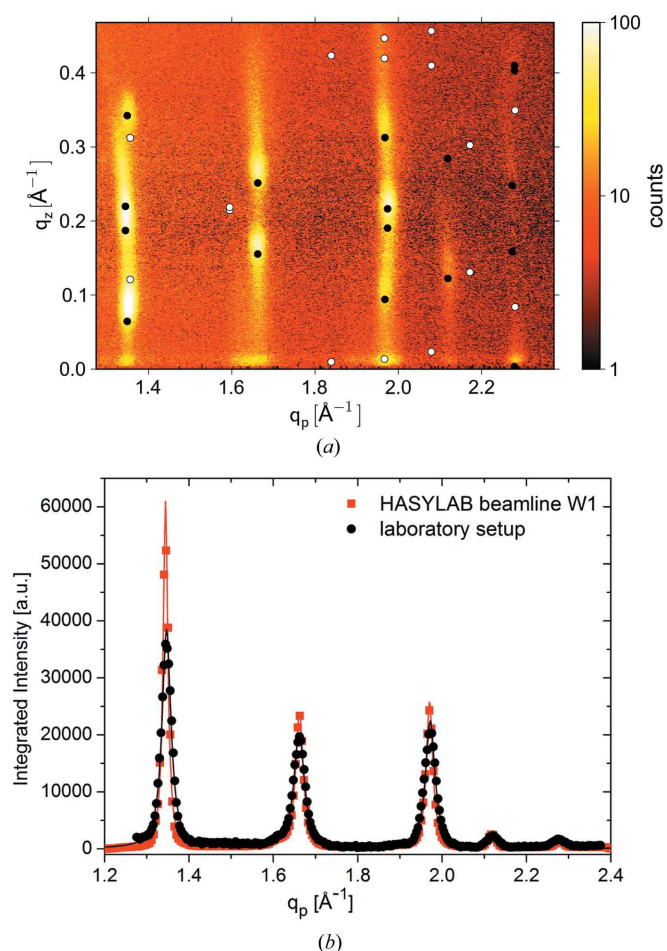


Figure 2
(a) Grazing-incidence reciprocal-space map of a 50 nm pentacene film grown on SiO_2 measured with the laboratory setup. Reflections corresponding to the pentacene thin-film phase are indicated with black dots, bulk-phase contributions with white dots. (b) Comparison between beamline W1 (HASYLAB) and the laboratory measurements (red squares and black dots, respectively). Intensities are integrated over a q_z range from 0 to 0.46 \AA^{-1} and afterwards corrected for background. The peaks are fitted with Lorentzians (full lines).

The ratio found between the peak area measured in the laboratory and that measured at the synchrotron was 1.2. Hence, a 50 times longer total measurement time in the laboratory (16.5 h) than at the synchrotron (20 min) results in comparable quality. This is still a reasonable measurement time for normal laboratories. Comparing integrated count rates of the peaks reveals that a 100 times longer integration time is needed in the laboratory for statistics equivalent to the synchrotron measurement.

The peak widths (FWHM) of the synchrotron data are smaller than the peaks of the laboratory measurement, *e.g.* 0.014 \AA^{-1} (HASYLAB) versus 0.024 \AA^{-1} (laboratory) for the first, 0.021 versus 0.03 \AA^{-1} for the second, and 0.018 versus 0.029 \AA^{-1} for the third peak. This is due to a worse in-plane resolution in the laboratory. The in-plane resolution of the laboratory equipment is determined by the Soller slits. Their angular acceptance has to be chosen as a trade-off between intensity (*i.e.* measurement time necessary to obtain the requested measurement statistics) and resolution. The FWHM in reciprocal space of the first peak (0.024 \AA^{-1}) corresponds to 0.34° in angular space, *i.e.* exactly the angular acceptance of the Soller slits (0.35°). The FWHMs of the second and third peaks are slightly larger

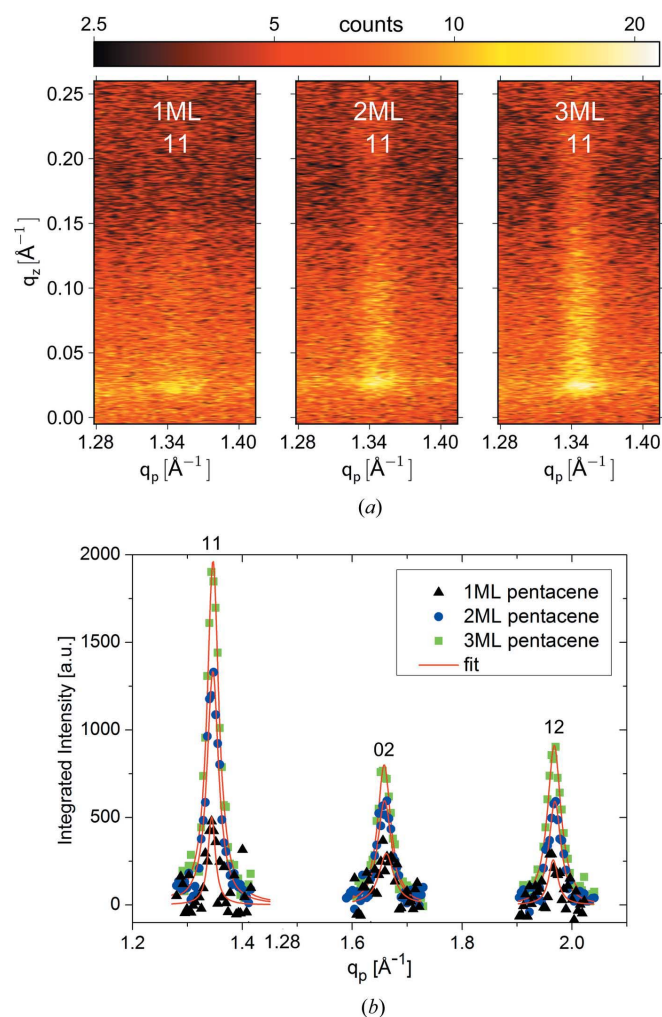


Figure 3 (a) Grazing-incidence reciprocal-space map of the 11 Bragg rod of nominally 1 ML, 2 ML and 3 ML pentacene on SiO_2 . (b) Background-subtracted diffraction intensities of 1 ML, 2 ML and 3 ML pentacene integrated along the q_z direction (from 0 to 0.25 \AA^{-1}) and plotted as a function of the in-plane scattering vector q_p (triangles, circles and squares). The first three Bragg rods are shown and fitted with Lorentzians (full lines).

Table 1

Two dimensional unit-cell parameters of 1 ML, 2 ML and 3 ML pentacene calculated from the fitted diffraction peak positions of Fig. 3(b).

The parameters obtained from our laboratory data are compared with parameters from previous studies of pentacene monolayer (Fritz *et al.*, 2004), sub-monolayer (SML) and multilayer (MML) (Ruiz *et al.*, 2004) samples (all from synchrotron measurements).

	a (Å)	b (Å)	γ (°)
1 ML (this work)	5.91 (6)	7.56 (3)	89.6 (5)
2 ML (this work)	5.92 (2)	7.58 (1)	90.0 (2)
3 ML (this work)	5.91 (1)	7.58 (1)	89.9 (2)
1 ML (Fritz <i>et al.</i> , 2004)	5.916	7.588	89.95
SML (Ruiz <i>et al.</i> , 2004)	5.90	7.62	90.0 (2)
MML (Ruiz <i>et al.</i> , 2004)	5.91	7.58	90.0 (2)

because of the presence of two polymorph structures of pentacene appearing at similar q_p positions (compare Fig. 2a). Nevertheless, the in-plane resolution is quite sufficient to characterize organic thin films, although caution is advised when performing crystal size determinations by peak breadth analysis. The resolution limit for grain size analysis is reached if the peak broadening due to the crystal grain size does not exceed the broadening due to the apparatus resolution by at least 50% (Smilgies, 2009). For the presented setup this leads to a maximum in-plane crystal size of 25 nm accessible to grain size determinations. Transverse shear force microscopy studies on pentacene monolayers vacuum deposited on SiO_2 report lateral crystalline domain sizes of 1–2 μm (Zhang *et al.*, 2008; Wu *et al.*, 2009); thus the observed peak broadening is purely caused by the in-plane resolution of the setup.

4.2. Pentacene mono- and multilayers

Pentacene films of nominally one-monolayer (1 ML; 1.3 nm), 2 ML (2.6 nm) and 3 ML (3.9 nm) thickness were prepared by vacuum deposition on thermally oxidized silicon wafers. The RSMs of the first Bragg rod of the 1 ML, 2 ML and 3 ML samples are shown in Fig. 3(a). A step size of $\Delta 2\theta_i = 0.05^\circ$ was chosen using an integration time of 360 s per step. The rod-like shape of the diffraction features originates from the absence of a periodicity perpendicular to the substrate surface that is characteristic for monolayer films. As expected, for the 2 and 3 ML samples, the evolution of a three-dimensional structure is observed by the emergence of Bragg peaks at out-of-plane q_z values for the 02 and 12 Bragg rods (see supplementary figure¹). However, the quality of these Bragg rod profiles, especially for 1 ML, is not sufficient to perform quantitative analyses of the profiles. Background-subtracted integral intensity diffraction profiles (integrated over a q_z range from 0 to 0.25 \AA^{-1}) for the 1 ML, 2 ML and 3 ML samples are shown in Fig. 3(b) for the first three Bragg rods. Because the indexing of the first three rods (11, 02 and 12) is known from previous work (Fritz *et al.*, 2004), the two-dimensional unit-cell parameters can be calculated from the q_p positions of the rods (obtained by fitting the integrated diffraction profiles with Lorentzians). The resulting parameters are summarized in Table 1 and show perfect agreement with previous studies of pentacene mono- and multilayers carried out by Fritz *et al.* (2004) and Ruiz *et al.* (2004), both using synchrotron radiation.

5. Conclusion

In this work, we presented a novel laboratory setup for grazing-incidence X-ray diffraction and demonstrated that our experimental

¹ The supplementary material discussed in this paper is available from the IUCr electronic archives (Reference: RG5007). Services for accessing these data are described at the back of the journal.

approach provides an effective possibility to characterize organic thin films and monolayers in the laboratory on a reasonable timescale. Our results clearly demonstrate that high-quality GIXD studies can be performed with laboratory sources even in the monolayer range. We showed that the quantity of matter of one monolayer ($6.52 \text{ electrons } \text{Å}^{-2}$) is sufficient to perform an in-plane X-ray diffraction study that allows the clear observation of Bragg rods.

This work was supported by the Austrian Science Fund (FWF):[S9708]. The authors thank W. Caliebe (DESY-HASYLAB, Hamburg, Germany) for experimental support.

References

- Als-Nielsen, J., Jacquemain, D., Kjaer, K., Leveiller, F., Lahav, M. & Leiserowitz, L. (1994). *Phys. Rep.* **246**, 251–313.
- Campbell, R. B., Robertson, J. M. & Trotter, J. (1962). *Acta Cryst.* **15**, 289–290.
- Dosch, H. (1992). *Critical Phenomena at Surfaces and Interfaces: Evanescent X-ray and Neutron Scattering*, Springer Tracts in Modern Physics, Vol. 126. Berlin, Heidelberg: Springer.
- Fritz, S. E., Martin, S. M., Frisbie, C. D., Ward, M. D. & Toney, M. F. (2004). *J. Am. Chem. Soc.* **126**, 4084–4085.
- Kaganer, V. M., Möhwald, H. & Dutta, P. (1999). *Rev. Mod. Phys.* **71**, 779–819.
- Khazins, D., Becker, B., Diawara, Y., Durst, R., He, B., Medved, S., Sedov, V. & Thorson, T. (2004). *IEEE Trans. Nucl. Sci.* **51**, 943–947.
- Mannsfeld, S. C., Tang, M. L. & Bao, Z. (2011). *Adv. Mater.* **23**, 127–131.
- Marra, W. C., Eisenberger, P. & Cho, A. Y. (1979). *J. Appl. Phys.* **50**, 6927–6933.
- Mattheus, C. C., Dros, A. B., Baas, J., Meetsma, A., Boer, J. L. de & Palstra, T. T. M. (2001). *Acta Cryst.* **C57**, 939–941.
- Moser, A. (2011). *PyGid: Software for the Analysis of Grazing-Incidence X-ray Diffraction Data*. Personal communication.
- Moser, A., Werzer, O., Flesch, H., Koini, M., Smilgies, D., Nabok, D., Puschnig, P., Ambrosch-Draxl, C., Schiek, M., Rubahn, H. & Resel, R. (2009). *Eur. Phys. J. Spec. Top.* **167**, 59–65.
- Nabok, D., Puschnig, P., Ambrosch-Draxl, C., Werzer, O., Resel, R. & Smilgies, D.-M. (2007). *Phys. Rev. B*, **76**, 235322.
- Neuhold, A., Novák, J., Flesch, H.-G., Moser, A., Djuric, T., Grodd, L., Grigorian, S., Pietsch, U. & Resel, R. (2012). *Nucl. Instrum. Methods Phys. Res. Sect. B*, doi:10.1016/j.nimb.2011.07.105.
- Novák, J., Oehzelt, M., Berkebile, S., Koini, M., Ules, T., Koller, G., Haber, T., Resel, R. & Ramsey, M. G. (2011). *Phys. Chem. Chem. Phys.* **13**, 14675–14684.
- Resel, R., Oehzelt, M., Lengyel, O., Haber, T., Schulli, T., Thierry, A., Hlawacek, G., Teichert, C., Berkebile, S. & Koller, G. (2006). *Surf. Sci.* **600**, 4645–4649.
- Ruiz, R., Mayer, A. C., Malliaras, G. G., Nickel, B., Scoles, G., Kazimirov, A., Kim, H., Headrick, R. L. & Islam, Z. (2004). *Appl. Phys. Lett.* **85**, 4926–4928.
- Salzmann, I., Nabok, D., Oehzelt, M., Duhm, S., Moser, A., Heimel, G., Puschnig, P., Ambrosch-Draxl, C., Rabe, J. P. & Koch, N. (2011). *Cryst. Growth Des.* **11**, 600–606.
- Schiefer, S., Huth, M., Dobrinevski, A. & Nickel, B. (2007). *J. Am. Chem. Soc.* **129**, 10316–10317.
- Schuster, M. & Gobel, H. (1995). *J. Phys. D Appl. Phys.* **28**, A270–A275.
- Smilgies, D.-M. (2009). *J. Appl. Cryst.* **42**, 1030–1034.
- Tanner, B. K., Hase, T. P. A., Lafford, T. A. & Goorsky, M. S. (2004). *Powder Diffr.* **19**, 45–48.
- Vineyard, G. H. (1982). *Phys. Rev. B*, **26**, 4146–4159.
- Wu, Y., Toccoli, T., Zhang, J., Koch, N., Iacob, E., Pallaoro, A., Iannotta, S. & Rudolf, P. (2009). *Appl. Phys. A*, **95**, 21–27.
- Yoshida, H., Inaba, K. & Sato, N. (2007). *Appl. Phys. Lett.* **90**, 181930.
- Zhang, J., Rabe, J. P. & Koch, N. (2008). *Adv. Mater.* **20**, 3254–3257.

Bibliography

- Als-Nielsen, J., Jacquemain, D., Kjaer, K., Leveiller, F., Lahav, M. & Leiserowitz, L. (1994). Principles and applications of grazing incidence X-ray and neutron scattering from ordered molecular monolayers at the air-water interface, *Phys. Rept.* **246**(5): 251–313.
- Als-Nielsen, J. & McMorrow, D. (2001). *Elements of modern X-ray physics*, Wiley, New York.
- Bartsch, H. (2004). *Taschenbuch mathematischer Formeln*, Fachbuchverl. Leipzig im Carl-Hanser-Verl., München; Wien.
- Bhatta, U. M., Ghatak, J., Mukhopadhyay, M., Wang, J., Narayanan, S. & Satyam, P. (2009). Synchrotron x-ray induced damage in polymer (PS) thin films, *Nuclear Instruments and Methods in Physics Research Section B: Beam Interactions with Materials and Atoms* **267**(10): 1807 – 1810.
- Björck, M. & Andersson, G. (2007). GenX : an extensible x-ray reflectivity refinement program utilizing differential evolution, *Journal of Applied Crystallography* **40**(6): 1174–1178.
- Born, M. & Wolf, E. (1998). *Principles of optics - electromagnetic theory of propagation, interference and diffraction of light*, Cambridge Univ. Press.
- Braga, D. & Horowitz, G. (2009). High-performance organic field-effect transistors, *Advanced Materials* **21**: 1473–1486.
- Campbell, R. B., Robertson, J. M. & Trotter, J. (1962). The crystal structure of hexacene, and a revision of the crystallographic data for tetracene, *Acta Crystallographica* **15**(3): 289–290.
- Dietrich, S. & Wagner, H. (1984). Critical surface scattering of x-rays at grazing angles, *Zeitschrift für Physik B Condensed Matter* **56**(3): 207–215.
- Dimitrakopoulos, C. D., Brown, A. R. & Pomp, A. (1996). Molecular beam deposited thin films of pentacene for organic field effect transistor applications, *Journal of Applied Physics* **80**(4): 2501.
- Dimopoulos, T., Peić, A., Neuschitzer, M., Resel, R., Abermann, S., Postl, M., List, E. & Brückl, H. (2012). Photovoltaic properties of solar cells employing cupric oxide thin film absorber and zinc oxide nanowires, *submitted* .

- Dinelli, F., Murgia, M., Levy, P., Cavallini, M., Biscarini, F. & de Leeuw, D. M. (2004). Spatially correlated charge transport in organic thin film transistors, *Phys. Rev. Lett.* **92**: 116802.
- Dosch, H. (1987). Evanescent absorption in kinematic surface bragg diffraction, *Phys. Rev. B* **35**: 2137–2143.
- Dosch, H. (1992). *Critical Phenomena at Surfaces and Interfaces: Evanescent x-ray and neutron scattering*, Vol. 126, Springer Tracts in Modern Physics.
- Fichou, D. (ed.) (1999). *Handbook of oligo- and polythiophenes*, Wiley-VCH.
- Flesch, H.-G. (2010). *Interface Controlled Microstructure and Morphology of Thin Layers for Organic Electronics*, PhD thesis, Graz University of Technology.
- Flesch, H., Mathijssen, S. G. J., Gholamrezaie, F., Moser, A., Neuhold, A., Novák, J., Ponomarenko, S. A., Shen, Q., Teichert, C., Hlawacek, G., Puschnig, P., Ambrosch-Draxl, C., Resel, R. & de Leeuw, D. M. (2011). Microstructure and phase behavior of a Quinquethiophene-Based Self-Assembled monolayer as a function of temperature, *The Journal of Physical Chemistry C* **22925-22930115**: 22925–22930.
- Fritz, S. E., Martin, S. M., Frisbie, C. D., Ward, M. D. & Toney, M. F. (2004). Structural characterization of a pentacene monolayer on an amorphous sio₂ substrate with grazing incidence x-ray diffraction, *J. Am. Chem. Soc.* **126**(13): 4084–4085.
- Gundlach, D., Lin, Y., Jackson, T., Nelson, S. & Schlom, D. (1997). Pentacene organic thin-film transistors-molecular ordering and mobility, *IEEE Electron Device Letters* **18**(3): 87–89.
- Haber, T. & Resel, R. (2008). Crystallography of ultrathin organic films and nanoaggregates, in K. Al-Shamery, H.-G. Rubahn & H. Sitter (eds), *Organic nanostructures for next generation devices*, Springer, chapter 6, pp. 119–164.
- Hall, S. & McMahon, B. (eds) (2005). *International Tables for Crystallography Volume G: Definition and exchange of crystallographic data*, Springer.
- HASYLAB-DORIS-website (2012). http://hasylab.desy.de/facilities/doris_iii/facility_information/index_eng.html.
- HASYLAB-website (2012). http://hasylab.desy.de/facilities/doris_iii/beamlines/w1_roewi/beamline/beamline_layout/index_eng.html.
- Hecht, E. (2002). *Optics*, Addison-Wesley.
- Horcas, I., Fernaández, R., Gómez-Rodríguez, J. M., Colchero, J., Goómez-Herrero, J. & Baro, A. M. (2007). WSXM: a software for scanning probe microscopy and a tool for nanotechnology, *Review of Scientific Instruments* **78**(1): 013705.

- Kaganer, V. M., Möhwald, H. & Dutta, P. (1999). Structure and phase transitions in langmuir monolayers, *Rev. Mod. Phys.* **71**(3): 779–819.
- Khazins, D., Becker, B., Diawara, Y., Durst, R., He, B., Medved, S., Sedov, V. & Thorson, T. (2004). A parallel-plate resistive-anode gaseous detector for X-ray imaging, *IEEE Transactions on Nuclear Science* **51**(3): 943 – 947.
- Kiessig, H. (1931). Interferenz von Röntgenstrahlen an dünnen Schichten, *Annalen der Physik* **402**(7): 769–788.
- Kjaer, K. (1994). Some simple ideas on X-ray reflection and grazing-incidence diffraction from thin surfactant films, *Physica B: Condensed Matter* **198**(1-3): 100 – 109.
- Langford, J. I. & Wilson, A. J. C. (1978). Scherrer after sixty years: A survey and some new results in the determination of crystallite size, *Journal of Applied Crystallography* **11**(2): 102–113.
- Mannsfeld, S. C. B., Tang, M. L. & Bao, Z. (2011). Thin film structure of triisopropylsilylethynyl-functionalized pentacene and tetraceno[2,3-b]thiophene from grazing incidence x-ray diffraction, *Advanced Materials* **23**: 127–131.
- Mannsfeld, S. C. B., Virkar, A., Reese, C., Toney, M. F. & Bao, Z. (2009). Precise structure of pentacene monolayers on amorphous silicon oxide and relation to charge transport, *Advanced Materials* **21**: 2294–2298.
- Marra, W. C., Eisenberger, P. & Cho, A. Y. (1979). X-ray total external reflection bragg diffraction a structural study of the gaasal interface, *J. Appl. Phys.* **50**(11): 6927–6933.
- Mathijssen, S. G. J., Smits, E. C. P., van Hal, P. A., Wondergem, H. J., Ponomarenko, S. A., Moser, A., Resel, R., Bobbert, P. A., Kemerink, M., Janssen, R. A. J. & de Leeuw, D. M. (2009). Monolayer coverage and channel length set the mobility in self-assembled monolayer field-effect transistors, *Nature Nano* **4**(10): 674–680.
- Mattheus, C. C., Dros, A. B., Baas, J., Meetsma, A., Boer, J. L. d. & Palstra, T. T. M. (2001). Polymorphism in pentacene, *Acta Crystallographica Section C Crystal Structure Communications* **57**(8): 939–941.
- Mattheus, C. C., Dros, A. B., Baas, J., Oostergetel, G. T., Meetsma, A., de Boer, J. L. & Palstra, T. T. (2003). Identification of polymorphs of pentacene, *Synthetic Metals* **138**(3): 475 – 481.
- McMurdie, H., Morris, M., Evans, E., Paretzkin, B., Wong-Ng, W., Ettlinger, L. & Hubbard, C. (1986). *Powder Diffr.* **1**: 76.

- Meyer zu Heringdorf, F. (2008). The application of low energy electron microscopy and photoemission electron microscopy to organic thin films, *Journal of Physics: Condensed Matter* **20**(18): 184007.
- Moser, A. (2008). *Crystal structure determination from two-dimensional powders*, Master's thesis, Technische Universität Graz.
- Moser, A. (2011). PyGid: A software for the analysis of grazing incidence x-ray diffraction data. Private Communication.
- Moser, A., Werzer, O., Flesch, H., Koini, M., Smilgies, D., Nabok, D., Puschnig, P., Ambrosch-Draxl, C., Schiek, M., Rubahn, H. & Resel, R. (2009). Crystal structure determination from two-dimensional powders: A combined experimental and theoretical approach, *The European Physical Journal Special Topics* **167**: 59–65.
- Mottaghi, M. & Horowitz, G. (2006). Field-induced mobility degradation in pentacene thin-film transistors, *Organic Electronics* **7**: 528–536.
- Nabok, D., Puschnig, P., Ambrosch-Draxl, C., Werzer, O., Resel, R. & Smilgies, D.-M. (2007). Crystal and electronic structures of pentacene thin films from grazing-incidence x-ray diffraction and first-principles calculations, *Phys. Rev. B* **76**(23): 235322.
- Neuhold, A., Novák, J., Flesch, H.-G., Moser, A., Djuric, T., Grodd, L., Grigorian, S., Pietsch, U. & Resel, R. (2011). X-ray radiation damage of organic semiconductor thin films during grazing incidence diffraction experiments, *Nuclear Instruments and Methods in Physics Research Section B: Beam Interactions with Materials and Atoms* p. in press.
- Nénot, L. & Croce, P. (1980). Caractérisation des surfaces par réflexion rasante de rayons X. Application à l'étude du polissage de quelques verres silicates, *Revue de Physique Appliquée* **15**: 761–779.
- Parratt, L. G. (1954). Surface studies of solids by total reflection of x-rays, *Phys. Rev.* **95**: 359–369.
- Peatross, J. & Ware, M. (2011). *Physics of Light and Optics*, available at optics.byu.edu.
- Prince, E. & of Crystallography., I. U. (2004). *International tables for crystallography*, Vol. C, International Union of Crystallography by Kluwer Academic, Dordrecht; Boston.
- Richter, A. G., Guico, R., Shull, K. & Wang, J. (2006). Thickness and interfacial roughness changes in polymer thin films during X-irradiation, *Macromolecules* **39**(4): 1545–1553.

- Robinson, I. K. & Tweet, D. J. (1992). Surface X-ray diffraction, *Reports on Progress in Physics* **55**(5): 599–651.
- Ruiz, R., Choudhary, D., Nickel, B., Toccoli, T., Chang, K., Mayer, A. C., Clancy, P., Blakely, J. M., Headrick, R. L., Iannotta, S. & Malliaras, G. G. (2004b). Pentacene thin film growth, *Chemistry of Materials* **16**(23): 4497–4508.
- Ruiz, R., Mayer, A. C., Malliaras, G. G., Nickel, B., Scoles, G., Kazimirov, A., Kim, H., Headrick, R. L. & Islam, Z. (2004a). Structure of pentacene thin films, *Appl. Phys. Lett* **85**(21): 4926–4928.
- Salzmann, I., Nabok, D., Oehzelt, M., Duhm, S., Moser, A., Heimel, G., Puschnig, P., Ambrosch-Draxl, C., Rabe, J. P. & Koch, N. (2011). Structure solution of the 6,13-Pentacenequinone Surface-Induced polymorph by combining x-ray diffraction Reciprocal-Space mapping and theoretical structure modeling, *Crystal Growth & Design* **11**: 600–606.
- Scherrer, P. (1918). Bestimmung der Grösse und der inneren Struktur von Kolloidteilchen mittels Röntgenstrahlung, *Nachr. Ges. Wiss. Göttingen* **26**: 98–100.
- Schiefer, S., Huth, M., Dobrinevski, A. & Nickel, B. (2007). Determination of the crystal structure of substrate-induced pentacene polymorphs in fiber structured thin films, *J. Am. Chem. Soc.* **129**(34): 10316–10317.
- Schuster, M. & Gobel, H. (1995). Parallel-beam coupling into channel-cut monochromators using curved graded multilayers, *Journal of Physics D: Applied Physics* **28**: A270–A275.
- Sinha, S. K., Sirota, E. B., Garoff, S. & Stanley, H. B. (1988). X-ray and neutron scattering from rough surfaces, *Phys. Rev. B* **38**: 2297–2311.
- Smilgies, D.-M. (2009). Scherrer grain-size analysis adapted to grazing-incidence scattering with area detectors, *Journal of Applied Crystallography* **42**: 1030–1034.
- Smits, E. C. P., Mathijssen, S. G. J., van Hal, P. A., Setayesh, S., Geuns, T. C. T., Mutsaers, K. A. H. A., Cantatore, E., Wondergem, H. J., Werzer, O., Resel, R., Kemerink, M., Kirchmeyer, S., Muzafarov, A. M., Ponomarenko, S. A., de Boer, B., Blom, P. W. M. & de Leeuw, D. M. (2008). Bottom-up organic integrated circuits, *Nature* **455**(7215): 956–959.
- Tolan, M. (1999). *X-ray scattering from soft matter thin films : materials science and basic research*, Springer, Berlin.
- Vineyard, G. H. (1982). Grazing-incidence diffraction and the distorted-wave approximation for the study of surfaces, *Phys. Rev. B* **26**(8): 4146–4159.

- Werzer, O., Stadlober, B., Haase, A., Flesch, H. & Resel, R. (2009). Evaluation of organic sub-monolayers by x-ray based measurements under grazing incident conditions, *The European Physical Journal Applied Physics* **46**(2): 20403.
- Werzer, O., Stadlober, B., Haase, A., Oehzelt, M. & Resel, R. (2008). Full x-ray pattern analysis of vacuum deposited pentacene thin films, *The European Physical Journal B* **66**(4): 455–459.
- Wojdyr, M. (2010). Fityk : a general-purpose peak fitting program, *Journal of Applied Crystallography* **43**(5): 1126–1128.
- Wu, Y., Toccoli, T., Zhang, J., Koch, N., Iacob, E., Pallaoro, A., Iannotta, S. & Rudolf, P. (2009). Key role of molecular kinetic energy in $\hat{\text{A}}$ early stages of pentacene island growth, *Applied Physics A* **95**: 21–27.
- Yoneda, Y. (1963). Anomalous surface reflection of x rays, *Phys. Rev.* **131**(5): 2010–2013.
- Yoshida, H., Inaba, K. & Sato, N. (2007). X-ray diffraction reciprocal space mapping study of the thin film phase of pentacene, *Appl. Phys. Lett* **90**(18): 181930.
- Zhang, J., Rabe, J. P. & Koch, N. (2008). Grain-boundary evolution in a pentacene monolayer, *Advanced Materials* **20**: 3254–3257.
- Zhang, P. & Wojdyr, M. (2008). xylib, <http://xylib.sourceforge.net/>.